

Ground-state properties of one-dimensional matter and
The Zel'dovich effect in Rydberg atoms

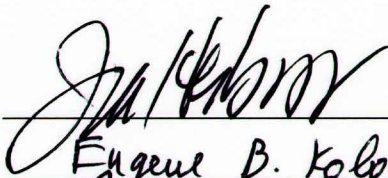
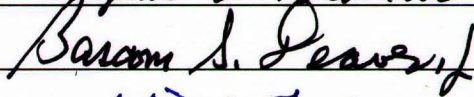
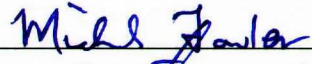
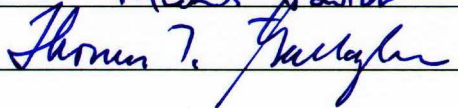
Michael Anthony Timmins
Charlottesville, Virginia

B.A. University of New Hampshire, 1988

A Dissertation presented to the Graduate Faculty of the
University of Virginia in Candidacy for the Degree of Doctor of
Philosophy

Department of Physics

University of Virginia
August, 2005


Eugene B. Kolomeisky

Bartram S. Deaver, Jr.

Michel J. Taylor

Thomas T. Gallagher

© Copyright by
Michael Anthony Timmins
All Rights Reserved
August, 2005

Abstract

The following dissertation consists of three parts. The first two concern ground-state properties of one-dimensional matter, while the third describes an experimental realization of the Zel'dovich effect in Rydberg atoms.

Motivated by emerging experimental possibilities to confine atoms and molecules in quasi-one-dimensional geometries, in Chapters 1 and 2 we analyze ground-state properties of strictly one-dimensional *molecular* matter comprised of identical particles of mass m interacting by a Morse potential between nearest neighbors. We find that due to zero-point motion, the system first undergoes a discontinuous evaporation transition into a *diatomic* gas followed by a continuous dissociation transition into a monoatomic gas. In particular we find that spin-polarized isotopes of hydrogen and ^3He are monoatomic gases, ^4He is a diatomic gas, while molecular hydrogen and heavier substances are Luttinger liquids. We also investigate the effect of finite pressure on the properties of the liquid and monoatomic gas phases. In particular we estimate a pressure at which molecular hydrogen undergoes an inverse Peierls transition into a metallic state which is a one-dimensional analog of the transition predicted by Wigner and Huntington in 1935. In Chapter 2, we show that dissociation of the Luttinger liquid is a process initiated at the system edge. The latter becomes unstable against quantum fluctuations at a value of De Boer's number which is smaller than that of the bulk instability which parallels the classical phenomenon of surface melting.

In 1959 Ya. B. Zel'dovich predicted that the bound-state spectrum of the non-relativistic Coulomb problem distorted at small distances by a short-range potential undergoes a peculiar reconstruction whenever this potential alone supports a low-energy scattering resonance. However documented experimental evidence of this effect has been lacking. In Chapter 3 we demonstrate that along the Periodic Table of elements the Zel'dovich effect manifests itself as a systematic periodic variation of the Rydberg spectra with a period proportional to the cubic root of the atomic number. This dependence, which is supported by analysis of experimental and numerical data, has its origin in the binding properties of the ionic core of the atom.

Acknowledgements

Well, it seems that the hot spell has finally come to an end in the nether regions. I'd like to dedicate this dissertation to my wife Sabra and my parents Michael and Kathy Timmins. I'd like to thank my wife Sabra for her unending support over the past decade (yes, decade). I'd also like to thank my sons Connory and Jack for keeping the swordplay to a minimum when "dad is studying". Without them, the rest is meaningless.

This wouldn't have been possible without the support of the Department of Physics, the chairman T. F. Gallagher, Peter Arnold and my boss Richard M. Marshall IV who have enabled me to maintain a hybrid student/employee existence for the past four years. Pam Joseph, Suzie Garrett and Tammie Shifflett have done an incredible job of maneuvering my administrative persona through the maze of paperwork required to get this far.

I can't say enough about Eugene Kolomeisky who is the inspiration behind it all. I consider him as much a friend as a mentor.

We thank M. Fowler, I. Harrison R. Kalas and T. J. Newman for valuable discussions. We are grateful to T. F. Gallagher and R. R. Jones for sharing with us their expertise. We also acknowledge R. M. Kalas and X. Yang who participated in the initial stages of the Zel'dovich effect project. This work was supported by the Thomas F. Jeffress and Kate Miller Jeffress Memorial Trust, the Chemical Sciences, Geosciences and Biosciences Division, Office of Basic Energy Sciences, Office of Science, U. S. Department of Energy.

Contents

| | | |
|----------|---|-----------|
| 1 | Ground-state properties of one-dimensional matter and quantum dissociation of a Luttinger liquid | 14 |
| 1.1 | Organization | 14 |
| 1.2 | Formulation of the problem | 16 |
| 1.3 | Luttinger liquid phase and its properties | 18 |
| 1.4 | Zero-pressure analysis | 21 |
| 1.4.1 | Approximate solution: $\lambda = \lambda_0$ | 23 |
| 1.4.2 | Perturbative renormalization-group treatment: $\lambda = \lambda_0$ | 25 |
| 1.4.3 | Accurate solution | 28 |
| 1.4.4 | Zero-pressure phase diagram | 34 |
| 1.5 | Finite pressure | 36 |
| 1.5.1 | Classical limit | 38 |
| 1.5.2 | Quantum case | 38 |
| 1.6 | Applications and Discussion | 45 |
| 1.6.1 | Spin-polarized hydrogen and its isotopes | 47 |
| 1.6.2 | Helium | 48 |
| 1.6.3 | Molecular hydrogen | 49 |
| 1.6.4 | Heavier substances | 52 |
| 2 | Quantum dissociation of an edge of a Luttinger liquid | 53 |
| 3 | The Zel'dovich effect and evolution of atomic Rydberg spectra along the Periodic Table | 61 |

| | | |
|-------|---|----|
| 3.1 | Organization | 61 |
| 3.2 | Distorted Coulomb problem and quantum defect | 62 |
| 3.2.1 | Zel'dovich effect in the $r_0 \ll a_B$ limit | 65 |
| 3.2.2 | Connection to Levinson's theorem | 71 |
| 3.2.3 | Zel'dovich effect in the $r_0 \gg a_B$ limit | 73 |
| 3.2.4 | Rectangular well example | 74 |
| 3.2.5 | Semiclassical treatment | 76 |
| 3.3 | Quantum defect of Rydberg electron | 78 |
| 3.3.1 | Method of comparison equations | 78 |
| 3.3.2 | Thomas-Fermi model of atomic ion: semiclassical solution | 80 |
| 3.3.3 | Beyond semiclassical approximation: connection to binding properties of ionic core | 83 |
| 3.4 | Comparison with experimental and numerical data | 86 |
| 3.4.1 | Effects of shell structure | 86 |
| 3.4.2 | Zel'dovich modulation | 96 |
| 3.5 | Conclusions and future directions | 98 |

List of Figures

| | | |
|-----|--|----|
| 1.1 | The Silvera-Goldman interaction potential between two hydrogen molecules (crosses) and its approximation by the Morse potential (solid curve). To demonstrate the strength of the overlap repulsion, a logarithmic scale is used on the positive energy axis. The energy is given in Kelvin; other details of the fit are explained in the text. | 15 |
| 1.2 | The flow diagram of the model (1.25). The arrows indicate the direction of the flow and the dashed line $v_0 = 1/\pi\lambda_0$ is the locus of initial conditions. The stable part of the $v = 0$, $\lambda_0 > 1/2$ fixed line corresponds to two segments of the chain infinitely far away from each other. For $\lambda_0 < 1/2$ the parameter v is relevant and the Morse bond joins the segments together. | 26 |
| 1.3 | The dependence of the Luttinger liquid quantum parameter λ , Eq.(1.17) on De Boer's number λ_0 , Eq.(1.17). The dashed line is $\lambda = \lambda_0$ | 30 |
| 1.4 | The reduced energy per particle of the Luttinger liquid phase as a function of De Boer's number λ_0 (1.17). The lower grey scale curve corresponds to approximate solution described by Eqs.(1.26) and (1.27) while the upper curve is an accurate solution given by Eqs.(1.37) and (1.38). The arrow shows the location of the dimer dissociation threshold $\lambda_{02} = \sqrt{2}/\pi$ | 31 |
| 1.5 | The reduced quantum expansion $Q - Q_0$ (a), and the Debye temperature θ^* (b) of the Luttinger liquid as functions of De Boer's number λ_0 (1.17). Various molecular substances are shown as solid dots on the curves. The numbers in the brackets on the quantum expansion graph are classical reduced bond lengths Q_0 while the size of vertical bars equals the relative bond fluctuation. The numbers in the brackets on the Debye temperature graph are Luttinger liquid exponents g (1.11). | 33 |

| | | |
|-----|---|----|
| 1.6 | The dependencies of the reduced energy per particle on De Boer's number λ_0 (1.4) for various phases. The bold parts of the curves correspond to ground states of the system while the grey scale segments indicate metastable states. The loci of a series of substances are shown by solid dots, and the arrow pointing down is the dimer dissociation threshold. | 35 |
| 1.7 | The $\lambda_0(\lambda)$ dependence, Eq.(1.45), for sufficiently small positive pressure ($p^* = 0.002$ is shown). The lines of fixed $\lambda_0 = \lambda_{0a,b}$ are the limits of stability of gas and liquid, respectively. | 39 |
| 1.8 | The $p^*(\lambda_0)$ diagram showing ranges of existence of liquid and monoatomic gas phases. Different scales are selected on the positive and negative parts of the pressure axis. The liquid and gas can be in equilibrium along the dotted line. | 42 |
| 1.9 | The dependence of the reduced quantum expansion $Q - Q_0$ on De Boer's parameter λ_0 at a negative pressure of large magnitude (a), within the liquid-gas coexistence region (b), and past the point C of Fig. 1.8 (c). | 43 |
| 2.1 | Dimensionless stiffness of the edge bond γ and corresponding binding energy of the edge particle E_{edge} of a half-infinite Luttinger liquid as functions of the quantum parameter λ (2.6). The region of metastability is confined to the $1/4 \leq \lambda \leq 0.3730$ range. | 57 |
| 2.2 | (Color online) Quantum expansion $Q-Q_0$ and rms fluctuation of the bulk and edge bonds as functions of the quantum parameter λ (2.6). The rms fluctuation is shown both as the vertical extent of shaded regions centered around the quantum expansion curves, and explicitly in the inset. | 58 |
| 2.3 | The dependences of the energy per particle for various bulk phases of the system on De Boer's number λ_0 (2.1) together with edge binding energy. The arrow pointing down is the dimer dissociation threshold. | 60 |
| 3.1 | Quantum defect for $U_s(r) = 0$ as a function of the range parameter x_0 , Eq.(3.5), and its $x_0 \gg 1$ limit, $\mu(0, x_0) = 3/4 - x_0/\pi$ (shown in gray scale). | 66 |
| 3.2 | Graphical solution of Eq.(3.10); $x_0 = 1/30$ has been used to construct the graph. The quantum defect μ is given by the intersections of the right-hand side of (3.10) with the line of constant $a_B/2\pi a_s$ | 67 |

| | | |
|------|--|----|
| 3.3 | Evolution of the Zel'dovich effect for the rectangular well of radius r_0 and depth U_0 for a series of range parameters x_0 , Eq.(3.5), manifested in the dependences of the quantum defect μ on $\zeta = (8mU_0r_0^2/\pi^2\hbar^2)^{1/2} \simeq w^{1/2}$ | 70 |
| 3.4 | Graphical solution of Eq.(3.12); $x_0 = 4$ has been used to construct the graph. The reduced quantum defect $M = \mu + x_0/\pi - 3/4$ is given by the intersections of the right-hand side of (3.12) with the line of constant a_s/r_0 | 73 |
| 3.5 | Plot of the surface of the relative quantum defect $\Delta\mu(\zeta, x_0) = \mu(\zeta, x_0) - \mu(0, x_0)$ for a rectangular potential well with dimensionless range and depth parameters x_0 and ζ , respectively, according to Eq.(3.9). | 75 |
| 3.6 | Plots of the number of de Broglie's half-waves $S_0/\pi\hbar$, (3.26), the range parameter x_0/π , (3.25), and semiclassical quantum defect μ_{sc} , (3.20) as functions of $Z^{1/3}$ for the Thomas-Fermi model of the residual atomic ion. | 82 |
| 3.7 | Dependence of the quantum defect μ on $Z^{1/3}$ along with its semiclassical approximant μ_{sc} , Eq.(3.20) (gray scale). The inset shows the Zel'dovich modulation $\delta\mu(Z^{1/3}) = \mu - \mu_{sc}$ together with the limiting expression, Eq.(3.22) (gray scale). | 84 |
| 3.8 | Dependences of the Zel'dovich modulation $\delta\mu = \mu - \mu_{sc}$ and the reduced scattering length of the ionic core a_s/r_0 (gray scale) on $Z^{1/3}$. The lines $a_s/r_0 = 0$ and $a_s/r_0 = 1$ are also shown to help the eye. | 85 |
| 3.9 | Systematic, experimental, and numerical dependences of the quantum defect μ on $Z^{1/3}$. To help orientation within the Periodic Table experimental alkali data are circled. | 88 |
| 3.10 | Modulation of systematic, experimental and numerical quantum defect $\delta\mu = \mu - \mu_{sc}$ relative to the semiclassical background, Eq.(3.20) as a function of $Z^{1/3}$ | 89 |
| 3.11 | Slater's ionic radii for singly-charged positive ions together with a series of corresponding ionic radii in crystals and systematic sizes of ionic core of the Rydberg atom, all in atomic units, as functions of $Z^{1/3}$. Numerical variation of the quantum defect $\delta\mu = \mu - \mu_{sc}$ is also displayed to show the correlation with Slater's radii. | 91 |
| 3.12 | Systematic, experimental and numerical amplitudes of the Fourier coefficients of the quantum defect variation (arbitrary units, same normalization) $ \mu_k $ as functions of k for $k \geq 0$. The peaks at $k \simeq 11$ correspond to the Zel'dovich effect. | 97 |

List of Tables

| | | |
|-----|---|----|
| 1.1 | Morse parameters for a series of molecular substances and some of their computed properties at zero pressure. Substances are arranged in the order of decrease of their De Boer's number λ_0 . Blank entries correspond to gas ground states when interparticle separation is infinite. | 44 |
| 3.1 | Experimentally measured quantum defects for series of elements with their atomic numbers Z and corresponding references. Systematic quantum defects of this work are also displayed for comparison. | 87 |

Introduction

Prediction of the ground-state properties of a condensed many-body system of identical particles starting from microscopic two-body interactions is only meaningful if the outer electronic shells of underlying atoms or molecules in the bound phase are not very different from their free state counterparts [1]. If the two-particle potential has a functional form common to a family of substances (for example, of the Lennard-Jones type), then the properties of all the members of the family can be related. This conclusion pioneered by De Boer and collaborators, commonly referred to as *the quantum theorem of corresponding states*, was originally applied to predict the properties of ^3He [2] *before* it had become experimentally available. Later Anderson and Palmer [3] and Clark and Chao [4] used the same approach to estimate the properties of zero-temperature nuclear and neutron-star matter from those of laboratory substances.

The goal of the first two chapters is to conduct a similar program in a strictly one-dimensional case. There are several reasons, both of fundamental and practical nature, why it is important to understand this problem.

First, it is well-known that for ordinary substances zero-point motion is of crucial importance only for the lightest elements such as helium isotopes as well as spin-polarized isotopes of hydrogen. The ground state of all heavier elements (and molecular hydrogen) is crystalline and to a large extent classical. The one-dimensional case is qualitatively different: regardless of the particle mass zero-point motion destroys the long-range crystalline order - a situation that is closely analogous to the destruction of the long-range order by thermal fluctuations in classical two-dimensional systems of continuous symmetry [5]. As a result, the only possible many-body bound state in one dimension is a harmonic or Luttinger liquid - a uniform density condensed phase with algebraically decaying density correlations [6]. This decay, characterized by a nonuniversal exponent, is slower than the exponential fall-off of density correlations in conventional fluids. As the degree of zero-point motion

increases, the many-body bound state can disappear through a transition that has no analog in the three-dimensional world: since the Luttinger liquid phase is more correlated than conventional fluids and less correlated than standard crystals its dissociation combines qualitative features of both laboratory melting and evaporation at once.

Second, in one dimension the difference between fermions and bosons is not very significant as we cannot go from one configuration to another with exchanged particles without bringing the particles in contact at some intermediate step. Then short-distance repulsion among bosons has the same effect on density correlations as the Pauli principle for fermions. On the other hand, zero-temperature properties of three-dimensional matter with an interaction pair potential of the Lennard-Jones form are sensitive to the statistics of the underlying particles [7].

Since experimental discovery of carbon nanotubes in 1991 [8] studying the properties of one-dimensional systems became especially important. In addition to their unique transport, mechanical and chemical properties [9], bundles of carbon nanotubes can play a role of one-dimensional hosts for foreign atoms that can find themselves bound in the interstitial channels or inside the tubes [10]. One of the interesting potential applications of these systems includes storage devices for molecular hydrogen in fuel cells [11].

Recently the quasi-one-dimensional regime has been also realized for Bose-condensates of alkali vapors both for repulsive [12] and attractive interactions [13]. These systems which are relevant for atom interferometry [14] have an additional flexibility as the strength and sign of two-body interactions can be magnetically tuned.

In both of these experimental examples the basic model is a zero-temperature one-dimensional many-body system of fermions or bosons with pairwise interactions. There were several attempts in the past to study this problem:

(i) Diffusion Monte Carlo studies predicted that at zero temperature both one-dimensional ^4He [15, 16] and molecular hydrogen [17] form weakly-bound liquids.

(ii) These conclusions were supported by variational studies based on the Jastrow-Feenberg wave function [18] where additionally it was argued that in one dimension the many-body bound state exists only for those systems which have a dimer, i. e. a two-body bound state. One of the findings common to Refs.[16, 17, 18] is the prediction of a high-density liquid-solid phase transition in which a standing density wave sets in. We note however that the existence of such a one-dimensional solid contradicts the quantum version of the Mermin-Wagner-Hohenberg theorem [5].

(iii) A direct variational treatment based on a Gaussian wave function was performed in Ref.[19] where it was assumed that the particles form a one-dimensional chain with the Morse potential interaction [20] between nearest neighbors. Although it was shown that the chain remained stable for not very strong quantum fluctuations, the accuracy of the method, the nature of the condensed phase, the role of dimerization, and the implications for real systems were not addressed.

The techniques used in Chapter 1 to study quantum dissociation of one-dimensional matter are applied in Chapter 2 to the problem of dissociation at the edge of a one-dimensional system. A classical three-dimensional solid melts through a first-order transition at a temperature when the free energies of the solid and liquid phases coincide. At sufficiently low temperatures quantum effects dominate and a quantum solid can melt due to zero-point motion [49].

The most curious feature of classical melting is the difficulty in overheating the solid while supercooling the liquid is easy. The latter is expected for the first-order transition while the former is explained by the phenomenon of surface melting: often, as the bulk transition is approached, the melting begins at the free surface of a solid. The surface melting is well-documented experimentally, and phenomenologically it can be viewed as a wetting of the solid by its own melt [50]. A well-understood example of surface melting of a quantum solid is that of the edge melting of the two-dimensional Wigner crystal in a strong magnetic field [51].

In Chapter 2 we will show that strictly one-dimensional matter with a free edge can also exhibit an analog of surface melting. Fundamentally this happens because the edge represents a zero-dimensional system subject to stronger quantum fluctuations than the one-dimensional bulk. Due to broken translational symmetry, zero-point motion modifies the cohesive properties of the edge differently from those of the bulk.

Chapter 3 presents an analysis of the Zel'dovich effect. In a variety of applications in physics it is important to understand how the normal Hydrogen spectrum is modified if at small distances the Coulomb law is replaced by a central short-ranged potential. An important aspect of this problem is the existence of two length scales - the Bohr radius of the Coulomb field a_B and the range of action of short-range forces r_0 .

For example, in hadronic atoms formed by charged particles and antiparticles the large distance Coulomb attraction gives way at short distances to nuclear forces whose range r_0 is significantly smaller than a_B [54].

In condensed matter physics a similar problem is that of the energy spectrum of the Wannier-

Mott exciton [55]. When in a semiconductor an electron is excited into the conduction band, a bound state with a hole left in the valence band can form. Due to the large dielectric constant of the medium the electron and the hole in the exciton are spatially well-separated. Therefore the electron-hole interaction is a Coulomb attraction modified at short distances. In this context a_B can exceed many times r_0 which is of the order of the Hydrogen Bohr radius.

Zel'dovich was apparently the first to recognize that in the limit $r_0 \ll a_B$ the spectrum of the distorted Coulomb problem is peculiar [56]. Since the centrifugal barrier decreases the probability of particle penetration in the region of small distances r , the effect of the short-range potential is strongest for the states of zero angular momentum. In this case the radial motion of a particle of mass m and energy E in a central potential $U(r)$ is described by the one-dimensional Schrödinger equation [57]

$$\frac{d^2\chi}{dr^2} + \frac{2m}{\hbar^2} (E - U(r)) \chi = 0 \quad (1)$$

where $\chi(r)/r$ is the radial wave function. Zel'dovich chose $U(r) = -\hbar^2/ma_B r$ for $r \geq r_0$ and $U(r) = U_s(r)$ otherwise and demonstrated that as long as the short-range potential $U_s(r)$ is not resonant, its effect is weak. If, on the other hand, $U_s(r)$ has a low-energy scattering resonance, a drastic reconstruction of the spectrum takes place. Using the example of the square well of depth U_0 he stated that as the dimensionless coupling constant $w \simeq mr_0^2 U_0/\hbar^2$ increases, the spectrum of the problem $E_n(w)$ evolves in a fashion resembling a sharp decreasing staircase. The steps are located at critical values of w at which bound states occur in $U_s(r)$ *only*. As w goes through the first threshold, the Coulomb levels E_n ($n \geq 2$) quickly fall to E_{n-1} while the ground state E_1 rapidly drops downward. The relative width of the region where the spectrum reconstruction takes place, $\Delta w/w \simeq r_0/a_B \ll 1$, is narrow, and qualitatively the same pattern repeats itself upon passing through every subsequent resonance.

A similar spectral behavior has been found by Popov [58] in his analysis of the Dirac equation for an electron in a field of the bare nucleus of charge Ze with $Z > 137$.

The Zel'dovich effect has been re-discovered in the spectra of hadronic atoms, and its generality has been demonstrated for any interaction with two widely different spatial scales [59].

Various aspects of the spectrum reconstruction have been investigated by Popov and collaborators [60]. Their study was motivated by then existing experimental evidence of the large $1s$ -level shift in the proton-antiproton atom which was naturally linked to the Zel'dovich effect. Later it became

clear that the experimental level shifts are small and the interest in the phenomenon declined.

As far as we know, at this time there is no documented experimental evidence of the Zel'dovich effect. This is not surprising because the spectrum reconstruction takes place in a narrow range of parameters in the vicinity of low-energy resonances. However a given experimental system is unlikely to be near resonance. A systematic search for the Zel'dovich effect would consist in looking for spectral changes in response to tuning of the central part of the potential which is often impossible - the strength of the nuclear force cannot be changed in the laboratory.

Recently Karnakov and Popov [61] pointed out that the Zel'dovich spectrum reconstruction takes place for a Hydrogen atom as a function of the external magnetic field thus providing an example of a system where a systematic search for the effect might be possible. Although the phenomenon is observable in numerical studies, direct experimental evidence is lacking and may only come from astrophysical observations as the pertinent magnetic fields are comparable to those on the surface of a neutron star.

The goal of Chapter 3 is to demonstrate that evolution of the Rydberg spectra of ordinary atoms along the Periodic Table provides direct evidence of the Zel'dovich effect. Since the condition $r_0 \ll a_B$ does not hold in atomic systems, the way the phenomenon manifests itself is less dramatic - we will show that it can be seen as a systematic periodic spectral modulation as a function of the cubic root of the atomic number Z .

It is known that for a highly excited s electron of a Rydberg atom the effect of polarization of the ionic core is negligible compared to that of the wave function penetration in the central region of the atom [62]. Therefore the electron dynamics can be adequately described by Eq.(1) where the effective central field $U(r)$ at large distances is that of a positively charged ion of charge e . On the other hand, starting from distances of the order of the size of the ionic core $r_0 \simeq a_B$ the field felt by the electron begins to deviate from the $-e^2/r$ form on-average decreasing, as $r \rightarrow 0$, to $-Ze^2/r$. By increasing Z along the Periodic Table Nature systematically deepens the inner part of the potential leaving the outer $-e^2/r$ tail intact. Thus by analyzing the Rydberg spectra as a function of atomic number Z it may be possible to correlate them with the binding properties of the ionic core which will constitute evidence of the Zel'dovich effect.

In atomic physics the motion of an electron in the field of a residual atomic ion has been studied in the past. Approximating the potential of the ionic core by that of the Thomas-Fermi or Thomas-Fermi-Dirac theories Latter [63] computed numerically the single-electron term values from $1s$ to $7d$

for all atoms. His ns spectra as a function of atomic number Z for largest n studied clearly show modulations on a decreasing energy curve. It is well-known that the large n atomic spectra are described by the Rydberg formula [62]

$$E_n = -\frac{\hbar^2}{2ma_B^2} \frac{1}{(n - \mu)^2} \quad (2)$$

where μ is the quantum defect which in the limit $n \rightarrow \infty$ does not depend on n . Latter's results imply that the dependence of the quantum defect μ on Z has modulations superimposed on an increasing curve.

The $\mu(Z)$ dependence has been numerically computed by Manson [64] and by Fano, Theodosiou and Dehmer [65] who used the Hartree-Slater model [66] to approximate the potential of the ionic core of the atom. Although the periodic variations of $\mu(Z)$ are strongly obscured by the shell effects (included in the Hartree-Slater model), Fano, Theodosiou and Dehmer argued that they are there and that there is a correlation between the location of radial nodes of the function χ from Eq.(1) near r_0 and the slope of the $\mu(Z)$ dependence. In view of the oscillation theorem [57] the nodal structure of the function χ is intimately related to the binding properties which suggests that systematic periodic variations of Rydberg spectra as a function of Z might be related to the Zel'dovich effect.

In order to demonstrate that this connection is correct in Chapter 3 we compute the upper part of the spectrum of the modified Coulomb problem not assuming that $r_0 \ll a_B$. We show that the staircase reconstruction taking place for $r_0 \ll a_B$ and the spectral modulations for $r_0 \simeq a_B$ are different limiting cases of the same phenomenon - sensitivity to the binding properties of the inner part of the potential which we continue to call the Zel'dovich effect. We also compare our results for $\mu(Z)$ with available experimental and numerical data to show that the phenomenon is observable.

Chapter 1

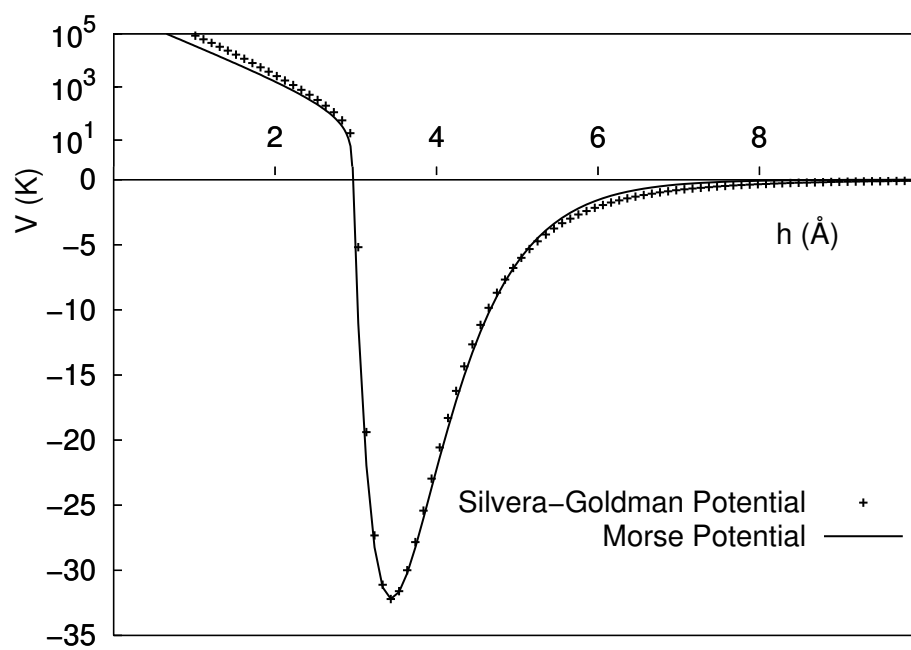
Ground-state properties of one-dimensional matter and quantum dissociation of a Luttinger liquid

1.1 Organization

In this Chapter the problem of the ground-state properties of a one-dimensional many-body system is re-examined for the case when the two-body interparticle interaction can be approximated by the Morse potential [20]. Since it involves three parameters, the Morse potential is more flexible in describing real systems as compared to the two-parameter Lennard-Jones potential. At the same time the quantum theorem of corresponding states [2] still holds in this case. In addition the problem of the Morse dimer is exactly solvable [20]; below we will also show that analytical progress is possible in the many-body case, and the accuracy of our results can be assessed.

The organization of the chapter is as follows. In Section 1.2 we set up the problem in general terms with the quantum theorem of corresponding states [2] as a guide for possible outcomes. The parameters of the Luttinger liquid are computed in Sections 1.3-1.5. In Section 1.3 we describe general properties of the Luttinger liquid and outline the main idea of the calculation. Zero-pressure analysis is carried out in Section 1.4. The main tool here is a combination of variational and renormalization-group treatments. As a by-product we also solve the problem of quantum Brownian

Figure 1.1: The Silvera-Goldman interaction potential between two hydrogen molecules (crosses) and its approximation by the Morse potential (solid curve). To demonstrate the strength of the overlap repulsion, a logarithmic scale is used on the positive energy axis. The energy is given in Kelvin; other details of the fit are explained in the text.



motion in the Morse potential, and show that it exhibits a localization-delocalization transition. Finite-pressure variational analysis is conducted in Section 1.5. Section 1.6 is dedicated to the discussion and applications of our results to various molecular substances. In particular we estimate a pressure at which one-dimensional molecular hydrogen undergoes a transition into a metallic state.

1.2 Formulation of the problem

Our starting point is the Euclidian action for N identical fermions or bosons of mass m with pairwise interactions

$$S = \int d\tau \left[\frac{m}{2} \sum_{i=1}^N \left(\frac{dx_i}{d\tau} \right)^2 + \sum_{i < j}^N V(x_i - x_j) \right], \quad (1.1)$$

where τ is the imaginary time variable, x_i are particle positions, and $V(h)$ is the pair interaction potential. The properties of the function $V(h)$ can be summarized as follows. At large separation h interparticle interaction is dominated by weak rapidly decaying Van der Waals attraction, while at short distances there is a very strong overlap repulsion [1]. As a result, the pair potential $V(h)$ has an asymmetric minimum at some intermediate h . As a typical example Fig.1.1 shows the semi-empirical Silvera-Goldman potential [21] between two H_2 molecules which is extensively used in computations of the properties of molecular hydrogen.

Assume that the pair potential has the form

$$V(h) = \epsilon U[(h - H_0)/l], \quad (1.2)$$

where ϵ is the energy scale of the potential, l is the potential range, H_0 is a length scale, and $U(y)$ is a function common to a family of substances. Introducing dimensionless position and time variables, $q_i = x_i/l$, $t = \epsilon\tau/\hbar$, transforms the reduced action S/\hbar into

$$\frac{S}{\hbar} = \int dt \left[\frac{m\epsilon l^2}{2\hbar^2} \sum_{i=1}^N \left(\frac{dq_i}{dt} \right)^2 + \sum_{i < j}^N U(q_i - q_j - Q_0) \right], \quad (1.3)$$

where $Q_0 = H_0/l$. The quantum theorem of corresponding states [2] then directly follows from representation (1.3): the energy *per particle* E^* measured in units of ϵ is only determined by the dimensionless parameter

$$\lambda_0 = \frac{\hbar}{\pi l (2m\epsilon)^{1/2}}, \quad (1.4)$$

the form of the function U in (1.2), and the particle statistics:

$$E^* = E^*(\lambda_0, \text{statistics}) \quad (1.5)$$

Similar statements can be made about the reduced *relative* equilibrium length per particle $Q - Q_0$ (Q is the one-dimensional version of volume per particle measured in units of l), and other quantities of interest. Apart from numerical factors (introduced for convenience), the quantum parameter λ_0 (1.4) is identical to De Boer's number [2]: its square is proportional to the ratio of the zero-point energy of a particle of mass m localized within a range l to the typical potential energy ϵ . Therefore as λ_0 increases away from its classical value $\lambda_0 = 0$, the strength of zero-point motion increases.

In the presence of several competing phases the function E^* in (1.5) (and other properties) will have several branches; the branch with lowest E^* singles out the ground-state of the system. When two different branches cross, the ground-state changes via a first-order phase transition. Each branch of $E^*(\lambda_0)$ is an analytical function of its argument except possibly at isolated points where critical phenomena take place. One obvious branch of E^* corresponds to a monoatomic gas which must become the ground state of the system at sufficiently large λ_0 . Then all the particles are infinitely far apart from each other, and thus $E_{mono}^*(\lambda_0) = 0$ which we select to be the reference point for the energy.

In what follows we select the pair interaction potential in the Morse form [20]:

$$\begin{aligned} V(h) &= -Ae^{-h/l} + Be^{-2h/l} \\ &\equiv \epsilon[-2e^{-(h-H_0)/l} + e^{-2(h-H_0)/l}], \end{aligned} \quad (1.6)$$

where A and B are the amplitudes of the attractive and repulsive parts of the potential, respectively, $H_0 = l \ln(2B/A)$ is the location of the minimum of (1.6), while $\epsilon = V(H_0) = A^2/4B$ is the depth of the potential well. The second representation of (1.6) shows explicitly that the Morse potential conforms to the general form (1.2). It is physically reasonable to require that the zero of (1.6) is located at positive h which implies $B > A$.

Similar to the applications of the Lennard-Jones potential to laboratory molecular systems [1], Eq.(1.6) should not be taken as literally describing two-particle interactions. The only reason behind our choice (1.6) is the possibility of analytic progress.

For two particles interacting according to (1.6) the ground-state energy is exactly known to be $E_2 = -\epsilon[1 - \hbar/2l(m\epsilon)^{1/2}]^2$ [20]. This implies that in the many-body case one of the possible phases of the system is a *diatomic* gas (a collection of infinitely far separated dimers) with the reduced energy function

$$E_{dimer}^*(\lambda_0) = -\frac{1}{2}\left(1 - \frac{\pi\lambda_0}{\sqrt{2}}\right)^2, \quad (1.7)$$

valid for $\lambda_0 \leq \lambda_{02} = \sqrt{2}/\pi$; the factor of 1/2 accounts for two particles in the dimer. As λ_0 approaches λ_{02} from below, the dimer size diverges, and at $\lambda_0 = \lambda_{02}$ a second-order dissociation transition into the monoatomic gas discussed earlier takes place. The asymmetry of the interaction potential is responsible for the disappearance of the two-body bound state for sufficiently strong zero-point motion.

The diatomic gas might be the ground-state of the system for intermediate λ_0 but for sufficiently small λ_0 a condensed phase must have the lowest energy. For molecular systems in general [1] pair interactions decay rapidly with interparticle separation. As a result, the physics of the condensed phase is dominated by nearest-neighbor interactions. Therefore in what follows in describing the one-dimensional condensed phase we restrict ourselves to nearest-neighbor interactions. Corrections coming from ignoring distant neighbors will be marginally small provided the interaction range l is substantially smaller than the average interparticle spacing (bond length).

In the classical limit, $\lambda_0 = 0$, the ground-state of the system is a one-dimensional crystal of particles with lattice spacing H_0 given by the minimum of the two-body Morse potential (1.6). Indeed, the energy per particle for the crystal, $-\epsilon$, is twice as negative as that for the diatomic gas.

A condensed phase is also the ground-state of the system for a not very large λ_0 . The quantitative theory of the properties of this phase is developed below.

1.3 Luttinger liquid phase and its properties

When zero-point motion is present, the asymmetry of the pair interaction potential about its minimum causes quantum expansion. As a result the average bond length H in the condensed state exceeds its classical, $\lambda_0 = 0$, counterpart H_0 . The low-energy dynamics of the system are described by the harmonic action [6]

$$S_{harm} = \frac{\rho}{2} \int dx d\tau \left[\left(\frac{\partial u}{\partial \tau} \right)^2 + c^2 \left(\frac{\partial u}{\partial x} \right)^2 \right], \quad (1.8)$$

where $u(x, \tau)$ is the particle displacement field, $\rho = m/H$ is the mass density, and c is the sound velocity [1]

$$c^2 = \frac{H^2}{m} \frac{\partial^2 E(h=H)}{\partial h^2}, \quad (1.9)$$

where $E(h)$ is the ground-state energy per particle as a function of (one-dimensional) volume per particle h , and the derivative is evaluated at the equilibrium interparticle spacing H . The function $E(h)$ can be also viewed as an effective pair interaction renormalized by zero-point motion away from its classical form (1.6).

The harmonic liquid is a possible ground state if interparticle interaction is not more long-ranged than an inverse-square potential - this comes from the scaling behavior of the kinetic energy operator in the many-body Schrödinger equation.

The Feynman path integral formulation of quantum mechanics [22] allows us to view the action (1.8) as a Hamiltonian for a classical two-dimensional crystal of line objects (world lines of underlying particles) running in the imaginary time direction. In this correspondence zero-point motion plays a role of thermal fluctuations. But this is exactly the context of applicability of the Mermin-Wagner-Hohenberg theorem [5]: if $n(x, \tau)$ is the instantaneous number density, then long-wavelength low-energy quantum fluctuations captured by the action (1.8) destroy long-range positional order of the particles. The only allowed many-body bound state is a uniform density phase, $\langle n(x, \tau) \rangle = H^{-1}$ ($\langle \rangle$ stands for the expectation value), with algebraic decay of density correlations [6]:

$$\langle n(x, \tau) n(0, 0) \rangle - H^{-2} \propto \frac{\cos(2\pi x/H)}{(x^2 + c^2 \tau^2)^g}, \quad (1.10)$$

where the exponent g is given by

$$g = \frac{\pi \hbar}{\rho c H^2} \quad (1.11)$$

The large distance/time behavior of the density-density correlation function (1.10) is the hallmark of the Luttinger liquid. In order to compute the range of existence of the Luttinger liquid phase, its bond length H , sound velocity c , and correlation exponent g we need to go beyond the harmonic approximation.

Our calculation relies on the assumption underlying the harmonic description (1.8) (and to be verified later) that as long as the Luttinger liquid is stable, the ratio of the typical fluctuation of the bond length to the bond length itself remains small despite the fact that individually both of these

quantities are increasing functions of λ_0 (1.17). Then every bond of the system can be viewed as a quantum-mechanical degree of freedom subject to the external potential $V(h)$ and placed in contact with a bath of *harmonic* oscillators (1.8) corresponding to the rest of the system. The single bond dynamics is thus given by the action:

$$S_{bond} = \frac{\rho}{2} \int_{bath} dx d\tau [(\frac{\partial u}{\partial \tau})^2 + c^2 (\frac{\partial u}{\partial x})^2] + \int d\tau V(h) \quad (1.12)$$

The first integral is over all positions and times except for a small region near $x = 0$ where the bond in question is located. This separates the system into two pieces, so that at all times the displacement field u is discontinuous: $u(x = +0, \tau) - u(x = -0, \tau) = h(\tau) - H_0$. The coupling between the segments of the system joined at the bond is given by the full pair potential $V(h)$, i. e. it goes beyond the harmonic approximation.

The action (1.12) has been previously introduced in Ref.[23] to describe tunneling-assisted fracture of a stretched one-dimensional chain. More generally this type of action corresponds to the Caldeira-Leggett model of coupling between a quantum-mechanical degree of freedom and an environment modeled by a reservoir of harmonic oscillators [24]. Since the last interaction term in (1.12) is restricted to a single spatial point, the bath degrees of freedom can be integrated out away from the bond with the result [23]:

$$S = \frac{\rho c}{4} \int_{-\omega_D}^{\omega_D} \frac{d\omega}{2\pi} |\omega| |h(\omega)|^2 + \int d\tau V(h), \quad (1.13)$$

where the subscript is dropped for brevity and the Fourier transform of the bond length field $h(\omega) = \int h(\tau) \exp(-i\omega\tau) d\tau$ has been introduced [25]. The frequency cutoff ω_D setting the limits of integration in the first kinetic term of (1.13) is the one-dimensional Debye frequency $\omega_D = \pi c/H$ - the vibrational spectrum of the system is approximated by the Debye model.

The unusual $|\omega|$ dependence of the kinetic term of the action (1.13) is due to the many-body nature of the bond dynamics, and can be understood heuristically by noticing that if the bond length oscillates with frequency ω , then during one oscillation period $2\pi/|\omega|$ this disturbance propagates in both directions away from the bond a distance of order $c/|\omega|$. Therefore the standard kinetic energy density, proportional to $\rho\omega^2$ should be multiplied by the size of the region $c/|\omega|$ affected by the motion thus reproducing the $\rho c|\omega|$ term of (1.13).

The action (1.13) allows us in principle to compute how the bath degrees of freedom renormalize the properties of a given bond. The nonanalytic $|\omega|$ dependence in (1.13) guarantees that the bond *cannot* renormalize the bath oscillators (whose properties are accumulated in the ρc combination). This observation combined with the fact that all the bounds of the Luttinger liquid are equivalent provides us with a prescription on how to use (1.13) to solve the problem we are interested in:

The parameters ρ and c of (1.13) should be selected as initially unknown but fully renormalized properties of the Luttinger liquid. The reservoir degrees of freedom will renormalize the microscopic pair interaction $V(h)$ into a form which we will require to be identical (in the harmonic limit) to the rest of the chain. This will determine the parameters of the Luttinger liquid and guarantee that the treatment is insensitive to the choice of the bond.

Since the action (1.13) describes the dynamics of an arbitrary single bond of the system, it can be directly used to compute the energy *per particle* of the original many-body problem.

1.4 Zero-pressure analysis

For a quantitative analysis we use Feynman's [26] variational principle for the ground-state energy:

$$E \leq E_1 = E_0 + (T/\hbar) \langle S - S_0 \rangle_0 \quad (1.14)$$

where T is the temperature, and \hbar/T has a meaning of the system size in the τ direction; the $T = 0$ limit will be taken at the end. The notation $\langle \rangle_0$ denotes an expectation value computed using an arbitrary reference action S_0 , and E_0 is the ground-state energy corresponding to S_0 .

This method has been remarkably successful in analyzing the roughening phase transition [27], multilayer adsorption phenomena [28], wetting transitions [29], the problem of quantum Brownian motion in a periodic potential [30], the Coulomb blockade problem [31], and a variety of problems of quantum mechanics and quantum field theory [32].

It is physically reasonable to select the trial action S_0 in a Gaussian form similar to that in [28], [29], and [31]:

$$S_0 = \frac{\rho c}{4} \int_{-\omega_D}^{\omega_D} \frac{d\omega}{2\pi} |\omega| |h(\omega)|^2 + \frac{K}{2} \int d\tau (h - H)^2, \quad (1.15)$$

where two variational parameters which include the familiar bond length H and a new parameter K (controlling the extent of fluctuations about H) are selected to minimize E_1 in (1.14). The stiffness

parameter K has a meaning of the curvature of the effective pair potential evaluated at its minimum H , and appearing in (1.9), $K = \partial_h^2 E(h = H)$.

Introducing $f = h - H$, the deviation of the bond length away from its equilibrium value H , the reduced root-mean-square (rms) fluctuation, $f^* = (\langle f^2 \rangle_0 / l^2)^{1/2}$, can be computed with the help of (1.15) as

$$f^* = (2\lambda)^{1/2} \ln^{1/2}(1 + \gamma^{-1}), \quad (1.16)$$

where

$$\lambda = \frac{\hbar}{\pi \rho c l^2} \quad (1.17)$$

is the dimensionless parameter quantifying the strength of zero-point motion in the Luttinger liquid, and

$$\gamma = \frac{2K}{\omega_D \rho c} \quad (1.18)$$

is the dimensionless counterpart of K . For the Morse pair interaction (1.6) the classical sound velocity is $c_0 = (H_0/l)(2\epsilon/m)^{1/2}$. It is then straightforward to verify that in the classical limit, $\hbar \rightarrow 0$, the quantum parameter λ (1.17) reduces to De Boer's number λ_0 (1.4).

In the Luttinger liquid the strength of zero-point motion is characterized by the correlation exponent g (1.11) which is related to λ (1.17) by

$$g = \lambda \pi^2 / Q^2, \quad (1.19)$$

where $Q = H/l$ is the reduced bond length. This relationship demonstrates that if the interaction range l is known, then measuring the density-density correlation function (1.10) will allow us to compute λ , and thus the rms fluctuation of the bond length (1.16).

Using (1.15), (1.16), and (1.6) the reduced upper bound $E^* = E_1/\epsilon$ entering (1.14) can be computed as

$$\begin{aligned} E^*(\gamma, Q) &= v^{-1} \ln(1 + \gamma) - 2e^{Q_0 - Q} (1 + \gamma^{-1})^\lambda \\ &+ e^{2(Q_0 - Q)} (1 + \gamma^{-1})^{4\lambda}, \end{aligned} \quad (1.20)$$

where

$$v = \frac{2\pi\epsilon}{\hbar\omega_D} \quad (1.21)$$

is related to the reduced Debye temperature as $\theta^* = \hbar\omega_D/\epsilon = 2\pi/v$.

The expression for E^* should be minimized with respect to γ and Q , and in case of multiple solutions the one minimizing (1.20) must be selected.

Minimizing E^* with respect to Q we arrive at the expression for the reduced bond length which accounts for quantum expansion

$$Q = Q_0 + 3\lambda \ln(1 + \gamma^{-1}) \quad (1.22)$$

Substituting this back into (1.20) the expression for the reduced energy E^* can be written as

$$E^*(\gamma) = v^{-1} \ln(1 + \gamma) - (1 + \gamma^{-1})^{-2\lambda}, \quad (1.23)$$

Minimizing (1.23) with respect to γ we find

$$\gamma = 2v\lambda(1 + \gamma^{-1})^{-2\lambda} \quad (1.24)$$

1.4.1 Approximate solution: $\lambda = \lambda_0$

First we look at a simplified version of the original problem when only one bond of the system is subject to the Morse potential (1.6) while the rest of the chain is harmonic. This situation is described by the action

$$\begin{aligned} S = & \frac{\rho_0 c_0}{4} \int_{-\omega_{D0}}^{\omega_{D0}} \frac{d\omega}{2\pi} |\omega| |h(\omega)|^2 \\ & + \int d\tau (-Ae^{-h/l} + Be^{-2h/l}), \end{aligned} \quad (1.25)$$

where $\rho_0 = m/H_0$, $c_0 = (H_0/l)(2\epsilon/m)^{1/2}$, and $\omega_{D0} = \pi c_0/H_0$ assume their classical values. The parameters A and B are selected so that in the harmonic approximation the Morse bond is identical to the rest of the chain.

If the imaginary time coordinate τ is viewed as a fictitious space variable then (1.25) can be recognized as an effective Hamiltonian defining a classical statistical mechanics problem [22]. If the bond field h is identified with an interface height and zero-point motion with thermal fluctuations, then this problem is a one-dimensional analog of the critical wetting problem [29], [33].

For finite λ_0 zero-point motion softens and lengthens the Morse bond while leaving the harmonic

part of the chain intact. This is described by Eqs.(1.22)-(1.24) with $\lambda = \lambda_0$ and $v = v_0 = 1/(\pi\lambda_0)$. Specifically, Eqs.(1.23) and (1.24) turn into:

$$E^*(\gamma) = \pi[\lambda_0 \ln(1 + \gamma) - \frac{\gamma}{2}] \quad (1.26)$$

$$\gamma = \frac{2}{\pi}(1 + \gamma^{-1})^{-2\lambda_0} \quad (1.27)$$

First we note that $\gamma = 0$ is always a solution to (1.27) with $E^* = 0$ which describes two segments of the chain infinitely far apart from each other. As λ_0 increases away from the classical value $\lambda_0 = 0$, the parameter γ in (1.27) monotonically decreases from $\gamma = 2/\pi$ vanishing at $\lambda_0 = 1/2$. For $\lambda_0 > 1/2$ only $\gamma = 0$ solves Eq.(1.27). When λ_0 approaches the critical value of $1/2$ from below we have

$$\gamma \simeq e^{-\frac{\ln(\pi/2)}{1-2\lambda_0}} \quad (1.28)$$

Correspondingly, the reduced energy (1.26) monotonically increases with λ_0 : in the classical limit, $\lambda_0 \rightarrow 0$, it rises linearly with λ_0 according to $E^* = -1 + \lambda_0[\pi \ln(1 + 2/\pi) + 2 \ln(1 + \pi/2)] \simeq -1 + 3.4361\lambda_0$. Since $\lambda_0 \sim 1/m^{1/2}$, Eq. (1.4), the energy E^* is *not* analytic as $1/m \rightarrow 0$, which is the relevant quantity [3]. This is expected because the crystal ($\lambda_0 = 0$) is qualitatively different from the Luttinger liquid (finite λ_0). Upon approaching $\lambda_0 = 1/2$ from below the reduced energy vanishes as

$$E^* \simeq -\frac{\pi}{2}(1 - 2\lambda_0)e^{-\frac{\ln(\pi/2)}{1-2\lambda_0}} \quad (1.29)$$

As λ_0 approaches $1/2$ the bond length diverges and for $\lambda_0 \geq 1/2$ the two segments of the chain are infinitely far apart from each other.

The behavior of the reduced bond length and its rms fluctuation just below the phase transition can be found by combining (1.16) and (1.22) with (1.28):

$$Q \simeq \frac{3 \ln(\pi/2)}{2(1 - 2\lambda_0)}, \quad f^* \simeq \frac{\ln^{1/2}(\pi/2)}{(1 - 2\lambda_0)^{1/2}} \quad (1.30)$$

We note that although both of these quantities diverge upon approaching the phase transition, the *relative* fluctuation, f^*/Q , vanishes. Thus fluctuating segments of the chain never overlap and our treatment is consistent.

The essential singularities (1.28) and (1.29) at $\lambda_0 = 1/2$ as well as the divergences (1.30) parallel

those found in the context of wetting transitions [29].

The most valuable feature of the variational approach is its nonperturbative nature. The accuracy of variational predictions depends on how close is the variational guess to the physical reality. For the problem defined by the action (1.25) the accuracy of our approach can be assessed and the special role played by $\lambda_0 = 1/2$ can be re-established by using a renormalization-group method.

1.4.2 Perturbative renormalization-group treatment: $\lambda = \lambda_0$

Following the argument of Brézin, Halperin, and Leibler originally given in the classical context of wetting transitions [33] we treat the Morse potential term in (1.25) as a perturbation. Then the lowest-order renormalization-group equations have the form:

$$\frac{d \ln A}{d \ln(\omega_{D0}\zeta)} = (\lambda_0 + 1), \quad \frac{d \ln B}{d \ln(\omega_{D0}\zeta)} = (4\lambda_0 + 1), \quad (1.31)$$

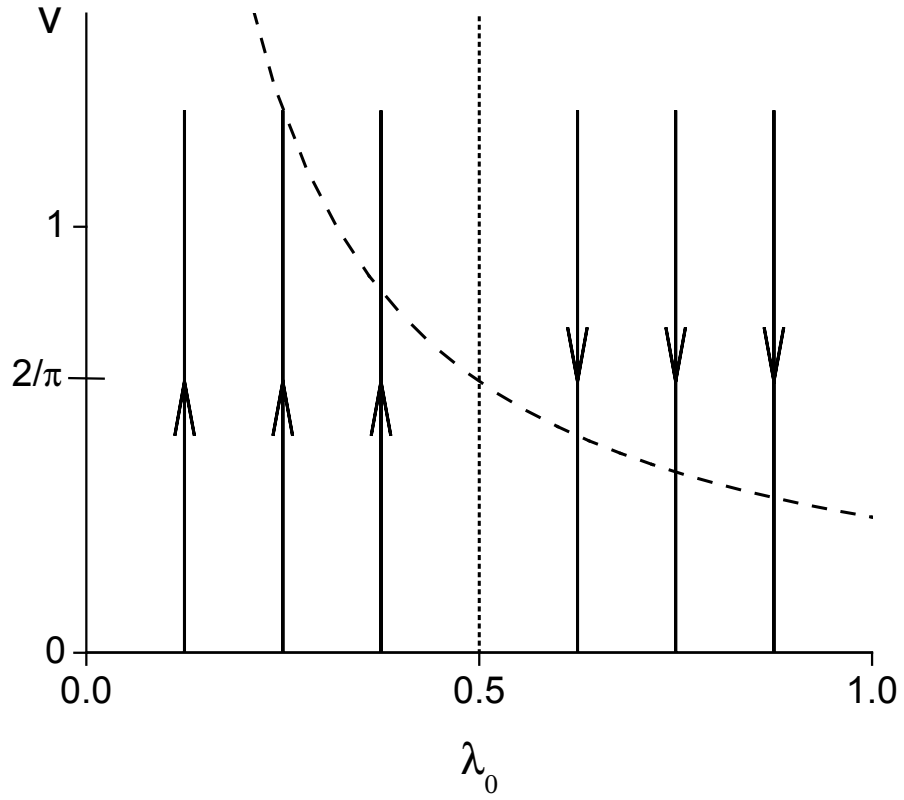
where ζ is the running scale in the τ direction, and the equations describe how the Morse parameters A and B renormalize upon (i) successive integration out of high-frequency modes (first terms) followed by (ii) scaling transformation which restores the cutoff to its original value (second terms). Instead of following separate evolution of the coefficients A and B , it is more appropriate to look at the depth of the Morse well (1.6) $\epsilon = A^2/4B$ which is also proportional to the potential curvature at its minimum. For its dimensionless counterpart v (1.21) Eqs.(1.31) imply

$$\frac{dv}{d \ln(\omega_{D0}\zeta)} = (1 - 2\lambda_0)v \quad (1.32)$$

The flow diagram corresponding to (1.32) is sketched in Fig. 1.2 where we also show the locus of initial conditions $v_0 = 1/\pi\lambda_0$ of the model (1.25).

First we note that verticality of the flow lines is a rigorous property of the model (1.25) as the $\rho_0 c_0$ combination (and thus λ_0) does not renormalize to any order in v . There are clearly two regimes separated by a phase transition at the critical value $\lambda_0 = 1/2$. For $\lambda_0 > 1/2$ the parameter v flows to zero which means that the chain is broken into two infinitely separated segments. On the other hand, for $\lambda_0 < 1/2$ the parameter v grows under renormalization eventually leaving the perturbative regime $v \ll 1$. This means that the Morse bond holds both segments of the chain together. Upon approaching the critical value $\lambda_0 = 1/2$ from below there is a divergent time scale ξ (analog of a

Figure 1.2: The flow diagram of the model (1.25). The arrows indicate the direction of the flow and the dashed line $v_0 = 1/\pi\lambda_0$ is the locus of initial conditions. The stable part of the $v = 0$, $\lambda_0 > 1/2$ fixed line corresponds to two segments of the chain infinitely far away from each other. For $\lambda_0 < 1/2$ the parameter v is relevant and the Morse bond joins the segments together.



correlation length in standard critical phenomena) which can be found from the condition $v(\xi) \simeq 1$:

$$\xi \simeq \omega_{D0}^{-1} e^{\frac{\ln(1/v_0)}{1-2\lambda_0}} \quad (1.33)$$

The one-dimensional nature of the problem then implies that the reduced curvature γ (1.18) of the renormalized potential vanishes as ξ^{-1} . Similarly the critical behavior of the reduced bond length Q can be found as $Q \simeq \ln[B(\xi)/A(\xi)] \simeq (3/2) \ln(\omega_{D0}\xi)$, while its rms fluctuation is $f^* \simeq \ln^{1/2}(\omega_{D0}\xi)$. With ξ given by (1.33) and logarithmic accuracy these results coincide with their variational counterparts, Eq.(1.28) and (1.30). If we set the bare parameter v_0 in (1.33) at $2/\pi$ (the crossing of the locus of initial conditions $v_0 = 1/\pi\lambda_0$ and the $\lambda_0 = 1/2$ line) the renormalization-group results would become identical to those of the variational approach.

From a perturbative renormalization-group treatment alone we would not be able to make reliable statements about the phase transition at $\lambda_0 = 1/2$ as the analysis is valid for $v_0 \ll 1$ while for the problem in question (1.25) one has $v_0 = 2/\pi \simeq 0.64 < 1$ - it is on the border of applicability of perturbative theory. However combining the above results with the nonperturbative variational analysis makes a strong case. Since the latter produces the same answers in the region of parameters where renormalization-group results are less certain, we argue that the variational solution of (1.25) is very accurate in the range of λ_0 between the classical limit $\lambda_0 = 0$ and the dissociation transition $\lambda_0 = 1/2$ which is described exactly.

As a side observation we note that the problem (1.25) is most likely to be related to that of quantum Brownian motion of a particle in a *periodic* potential [30]. Superficially the only similarity between the two is that (1.25) can be also viewed as describing quantum Brownian motion in the Morse potential which has no periodicity.

The similarity between the problems becomes noticeable if one inspects their treatments. A comparison shows that our expression for variational energy (1.23) is identical to that of the periodic version of the problem with the amplitude of the periodic potential proportional to our parameter v (1.21) and our $\lambda = \lambda_0$ corresponding to $1/2\alpha$ of Fisher and Zwerger [30]. With this identification renormalization-group equation (1.32) coincides with its periodic counterpart [30]. Both problems have delocalization transitions of the same universality class driven by zero-point motion.

We remind the reader that the action (1.25) is an approximation to the original problem of the ground-state properties of the Luttinger liquid - only one bond is subject to the Morse potential

while the rest of the system is purely harmonic. This chain is obviously *stiffer* than the original system - a *smaller* level of zero-point motion will be necessary to cause dissociation of the Luttinger liquid. Therefore the results derived for the model (1.25) imply that *a zero-pressure Luttinger liquid phase cannot exist for $\lambda_0 \geq 1/2$* .

We also note that the critical value $\lambda_0 = 1/2$ is *larger* than the dimer dissociation threshold $\lambda_{02} = \sqrt{2}/\pi \simeq 0.4502$. This can be understood qualitatively by noticing that the dynamics of the Morse bond joining two half-infinite harmonic segments is more inertial (and thus more classical) than that of the Morse dimer. Therefore with the same underlying particles a *weaker* level of quantum fluctuations (i. e. *smaller* λ_0) suffices to break the dimer.

1.4.3 Accurate solution

In order to compute the properties of the Luttinger liquid more accurately while relying on the Gaussian approximation, Eq.(1.15), we have to impose the condition that all the bonds of the chain are equivalent. Then using definitions of De Boer's number λ_0 (2.1) and its Luttinger liquid counterpart λ (1.17) the parameter v (1.21) can be calculated as $v = \lambda/\pi\lambda_0^2$; for $\lambda = \lambda_0$ it reduces to $v = 1/\pi\lambda_0$ previously used in approximate treatment of the problem. Similarly the reduced curvature of the effective pair potential (1.18) can be computed with the help of Eq.(1.9) with the conclusion that $\gamma = 2/\pi$. This is exactly what was previously found in the approximate analysis in the classical limit, $\lambda_0 = 0$, when indeed all the bonds of the chain are equivalent.

Substituting $v = \lambda/\pi\lambda_0^2$, and $\gamma = 2/\pi$ in Eq.(1.20) we arrive at the expression for the reduced energy as a function of dimensionless “volume” per particle Q :

$$\begin{aligned} E^*(Q) &= (\pi\lambda_0^2/\lambda) \ln(1 + 2/\pi) - 2e^{Q_0 - Q + \lambda \ln(1 + \pi/2)} \\ &+ e^{2(Q_0 - Q) + 4\lambda \ln(1 + \pi/2)} \end{aligned} \quad (1.34)$$

Similarly Eqs.(1.16), (1.22)-(1.24) transform into

$$f^* = (2\lambda)^{1/2} \ln^{1/2}(1 + \pi/2) \quad (1.35)$$

$$Q = Q_0 + 3\lambda \ln(1 + \pi/2) \quad (1.36)$$

$$E_{LL}^* = e^{-2\lambda \ln(1 + \pi/2)} [\pi\lambda \ln(1 + 2/\pi) - 1] \quad (1.37)$$

$$\lambda_0 = \lambda e^{-\lambda \ln(1+\pi/2)} \quad (1.38)$$

Eqs.(1.34)-(1.37) are the main results of this Section. We note that in view of Eqs.(1.10) and (1.19) Eqs.(1.35)-(1.37) give the dependence of the reduced rms bond length fluctuation f^* , bond length Q , and energy per particle of the Luttinger liquid E_{LL}^* on the experimentally measurable quantum parameter λ .

The dependence of De Boer's number λ_0 on λ is given by Eq.(1.38); we are interested in the inverse dependence, $\lambda(\lambda_0)$.

The right-hand side of (1.38) has a maximum at $\lambda_s = \ln^{-1}(1 + \pi/2) \simeq 1.0591$ of magnitude $\lambda_{0s} = e^{-1} \ln^{-1}(1 + \pi/2) \simeq 0.3896$. For $\lambda_0 < \lambda_{0s}$ Eq.(1.38) has two roots for λ but only the smaller one is physical. For $\lambda_0 = \lambda_{0s}$ these two roots coincide, and for $\lambda_0 > \lambda_{0s}$ Eq.(1.38) has no solutions - the Luttinger liquid phase is no longer stable. We note that the Luttinger liquid cannot sustain a level of zero-point motion stronger than that corresponding to $\lambda_{0s} \simeq 0.3896$ which is *smaller* than the dimer dissociation threshold $\lambda_{02} = \sqrt{2}/\pi \simeq 0.4502$.

The $\lambda(\lambda_0)$ dependence found by inverting Eq.(1.38) is shown in Fig.1.3 by a solid line. In the classical limit, $\lambda_0 \rightarrow 0$, we have $\lambda \rightarrow \lambda_0$ as expected; then the effective pair potential (1.34) reduces to its bare Morse form. As λ_0 grows, the difference between λ and λ_0 increases. We note that De Boer's number λ_0 (1.4) is always *smaller* than its Luttinger liquid counterpart λ (1.17) which reflects softening of the Luttinger liquid by zero-point motion. The end point of the $\lambda(\lambda_0)$ dependence which is the limit of stability of the liquid phase is a critical phenomenon - there the $\lambda(\lambda_0)$ dependence has an infinite slope. Upon approaching λ_{0s} from below we find that λ is given by

$$\lambda = \lambda_s - \left[\frac{2e}{\ln(1 + \pi/2)} (\lambda_{0s} - \lambda_0) \right]^{1/2} \quad (1.39)$$

Although both the reduced rms fluctuation f^* (1.35) and bond length Q (1.36) are increasing functions of the Luttinger liquid parameter λ (1.17), the relative fluctuation f^*/Q has a maximum at $\lambda \ln(1 + \pi/2) = Q_0/3$. While the discussion of specific molecular substances will be postponed until Section 1.4, here we note that in our attempts to fit real two-body potentials into the Morse form the reduced classical bond length was always found to satisfy $Q_0 \gtrsim 5$. The relatively large value of Q_0 is a reflection of the strength of the short-distance overlap repulsion and weakness of the large-distance attraction in the pair interaction potential. With $Q_0 = 5$ (used hereafter for estimates) we find that $\lambda = (5/3) \ln^{-1}(1 + \pi/2) \simeq 1.7651$ at the maximum of the relative fluctuation. But the Luttinger

Figure 1.3: The dependence of the Luttinger liquid quantum parameter λ , Eq.(1.17) on De Boer's number λ_0 , Eq.(1.17). The dashed line is $\lambda = \lambda_0$.

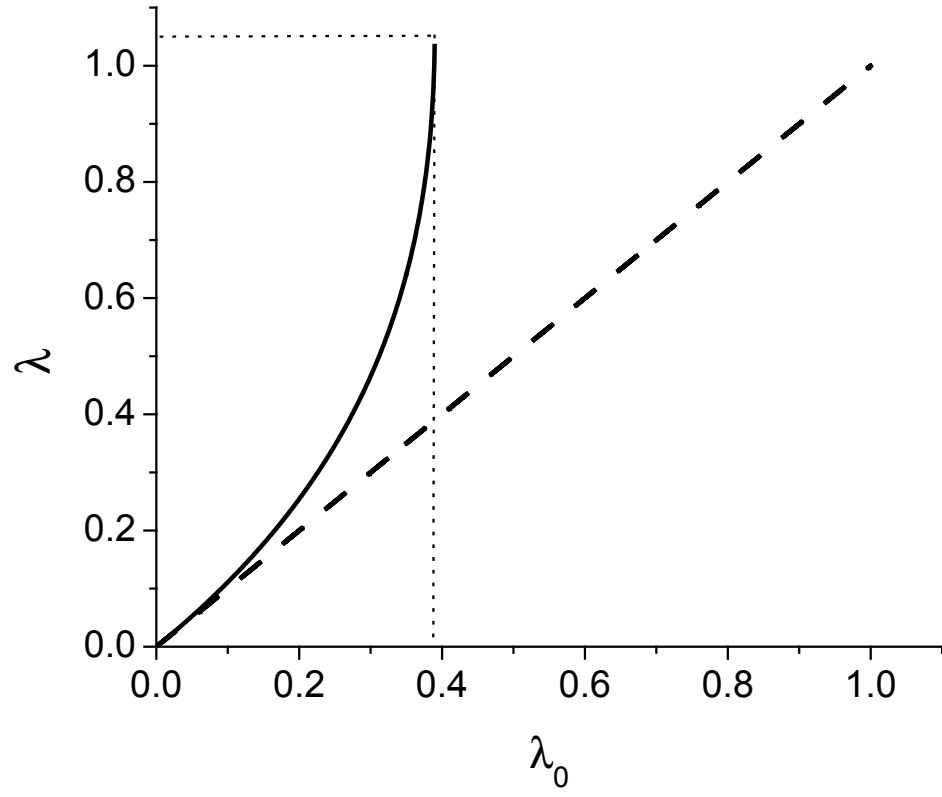
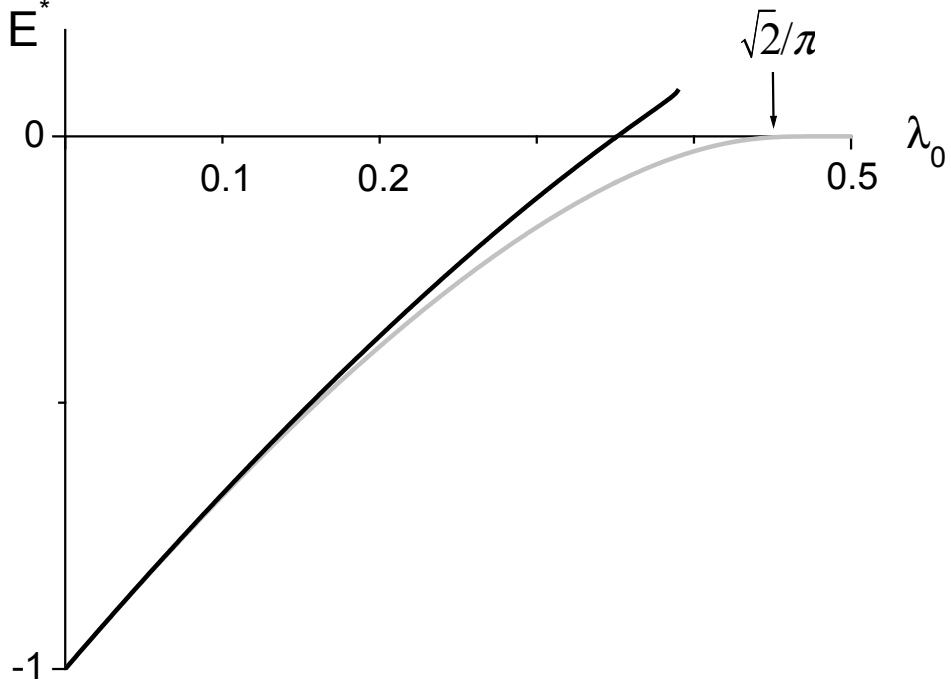


Figure 1.4: The reduced energy per particle of the Luttinger liquid phase as a function of De Boer's number λ_0 (1.17). The lower grey scale curve corresponds to approximate solution described by Eqs.(1.26) and (1.27) while the upper curve is an accurate solution given by Eqs.(1.37) and (1.38). The arrow shows the location of the dimer dissociation threshold $\lambda_{02} = \sqrt{2}/\pi$.



liquid cannot exist for $\lambda > \lambda_s = \ln^{-1}(1 + \pi/2) \simeq 1.0591$.

Therefore the relative fluctuation, f^*/Q , reaches its maximal value at the border of existence of the Luttinger liquid, $\lambda_s \simeq 1.0591$, with the magnitude not exceeding the level of about 0.18. This fact resembling Lindemann's empirical criterion of melting [34] verifies that our description of the bond dynamics as due to coupling to a bath of *harmonic* oscillators is quantitatively correct. The inequality $f^*/Q \ll 1$ implies that underlying particles never come into close contact with each other - the effect of particle statistics is negligible. In addition, having Q_0 substantially larger than unity justifies the nearest-neighbor interaction approximation in our treatment of the liquid.

The only remaining approximation which needs to be addressed is our replacement of the vibra-

tional spectrum of the system, $\omega(k) = (2c/H)|\sin(kH/2)|$, by the Debye model, $\omega(k) = c|k|$, valid for $\omega \leq \omega_D = \pi c/H$. Both spectra are fairly close to each other: they coincide in the long-wavelength limit, $kH \ll 1$, and end at the edges of the first Brillouin zone, $k = \pm\pi/H$. Physically the chain with the Debye spectrum is less susceptible to short-wavelength fluctuations than the original system - the Debye frequency ω_D is $\pi/2$ times larger than the maximal allowed frequency. This difference necessary to have the correct number of degrees of freedom will only have a marginally small effect on final results because of the dominant role played in one dimension by low-energy long-wavelength fluctuations where the Debye approximation becomes exact.

The upper curve of Fig. 1.4 shows the reduced ground-state energy per particle of the Luttinger liquid as a function of De Boer's number λ_0 (1.4) found by combining Eqs.(1.37) and (1.38). Qualitatively similar dependence was found in Ref.[19]; our energy is about 10 percent lower. For the purpose of comparison the lower grey scale curve of Fig. 1.4 shows the approximate reduced energy per particle, Eqs.(1.26) and (1.27), which was argued to constrain the $E_{LL}^*(\lambda_0)$ dependence from below. The quantitative difference between the curves is not very large and becomes noticeable only for $\lambda_0 > 0.15$. Since variational analysis always constrains the ground-state energy from above, the true $E_{LL}^*(\lambda_0)$ dependence must be sandwiched between the curves of Fig. 1.4. We expect however that $E_{LL}^*(\lambda_0)$ is well-approximated by Eqs.(1.37) and (1.38) (the upper curve of Fig. 1.4).

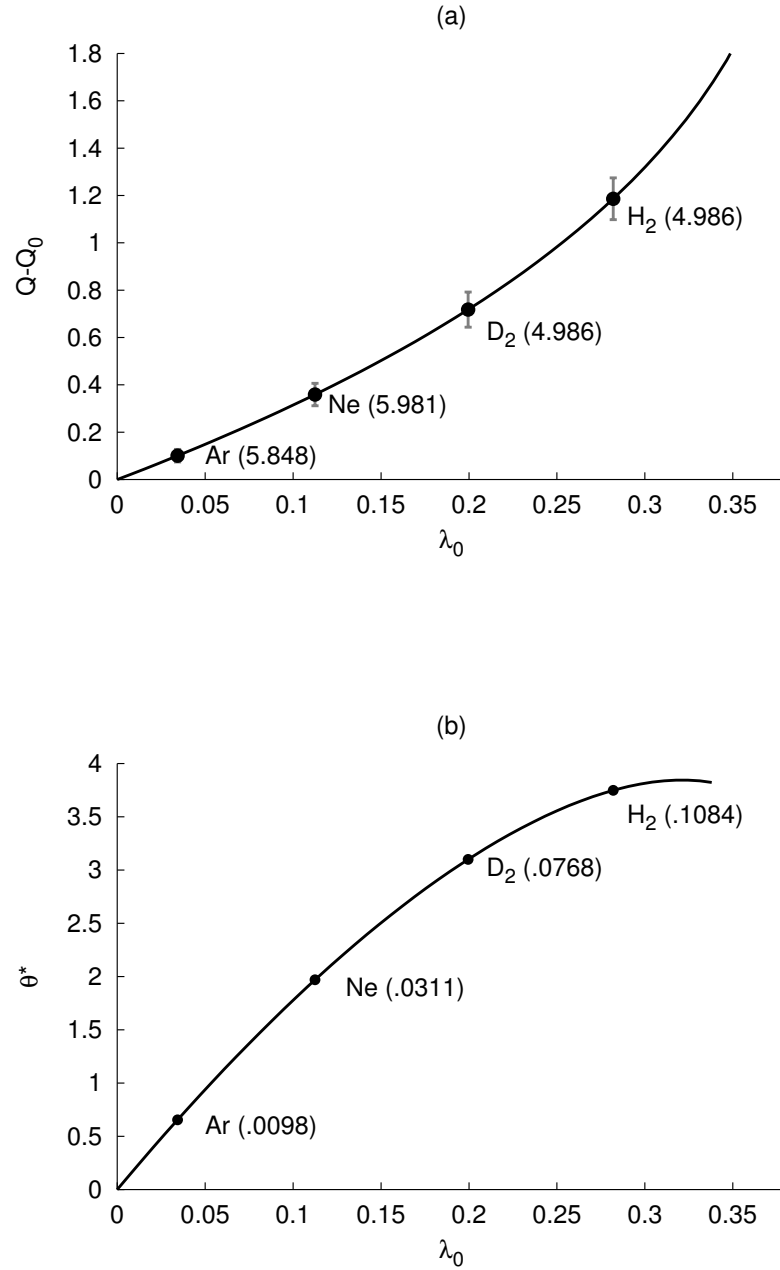
Variation of other properties of the Luttinger liquid with De Boer's number λ_0 (1.4) can be readily calculated. The expression for the reduced sound velocity $c^* = c/c_0$ can be found to be

$$\begin{aligned} c^* &= \lambda_0 Q / \lambda Q_0 \\ &= e^{-\lambda \ln(1+\pi/2)} [1 + 3(\lambda/Q_0) \ln(1 + \pi/2)], \end{aligned} \quad (1.40)$$

which together with (1.38) parametrically determine $c^*(\lambda_0)$. In the range of interest $Q_0 \gtrsim 5$ the reduced sound velocity is a monotonically decreasing function of λ_0 . At the boundary of existence of the Luttinger liquid the reduced sound velocity reaches its minimal (and finite) value and has a square-root singularity implied by Eq.(1.39).

Similarly the dependence of the Luttinger liquid exponent g (1.11) on λ_0 (1.4) can be found by combining Eqs.(1.19), (1.36) and (1.38). Again for $Q_0 \gtrsim 5$ the correlation exponent g is a monotonically increasing function of λ_0 reaching its maximal value at the boundary of existence of the liquid phase.

Figure 1.5: The reduced quantum expansion $Q - Q_0$ (a), and the Debye temperature θ^* (b) of the Luttinger liquid as functions of De Boer's number λ_0 (1.17). Various molecular substances are shown as solid dots on the curves. The numbers in the brackets on the quantum expansion graph are classical reduced bond lengths Q_0 while the size of vertical bars equals the relative bond fluctuation. The numbers in the brackets on the Debye temperature graph are Luttinger liquid exponents g (1.11).



The λ_0 dependence of the reduced Debye temperature θ^* is determined by

$$\theta^* = 2\pi/v = 2\pi^2\lambda e^{-2\lambda \ln(1+\pi/2)}, \quad (1.41)$$

combined with Eq.(1.38). The right-hand side of (1.41) has a maximum at $\lambda = \lambda_s/2 = 0.5 \ln^{-1}(1 + \pi/2) \simeq 0.5295$ which is inside the range of existence of the liquid phase. In view of (1.38) this corresponds to De Boer's number $\lambda_0 = 1/[2e^{1/2} \ln(1 + \pi/2)] \simeq 0.3212$ which is the location of the maximum of the $\theta^*(\lambda_0)$ dependence.

Figure 1.5 shows the dependence of the reduced quantum expansion $Q - Q_0$ and Debye temperature θ^* on De Boer's number λ_0 . The quantum expansion is found by combination of Eqs.(1.36) and (1.38); it is merely a magnified $\lambda(\lambda_0)$ curve of Fig. 1.3. The $\theta^*(\lambda_0)$ dependence (Fig. 1.5b) is constructed by combining Eqs.(1.41) and (1.38). Both properties are linear functions of De Boer's number in the $\lambda_0 \rightarrow 0$ limit.

1.4.4 Zero-pressure phase diagram

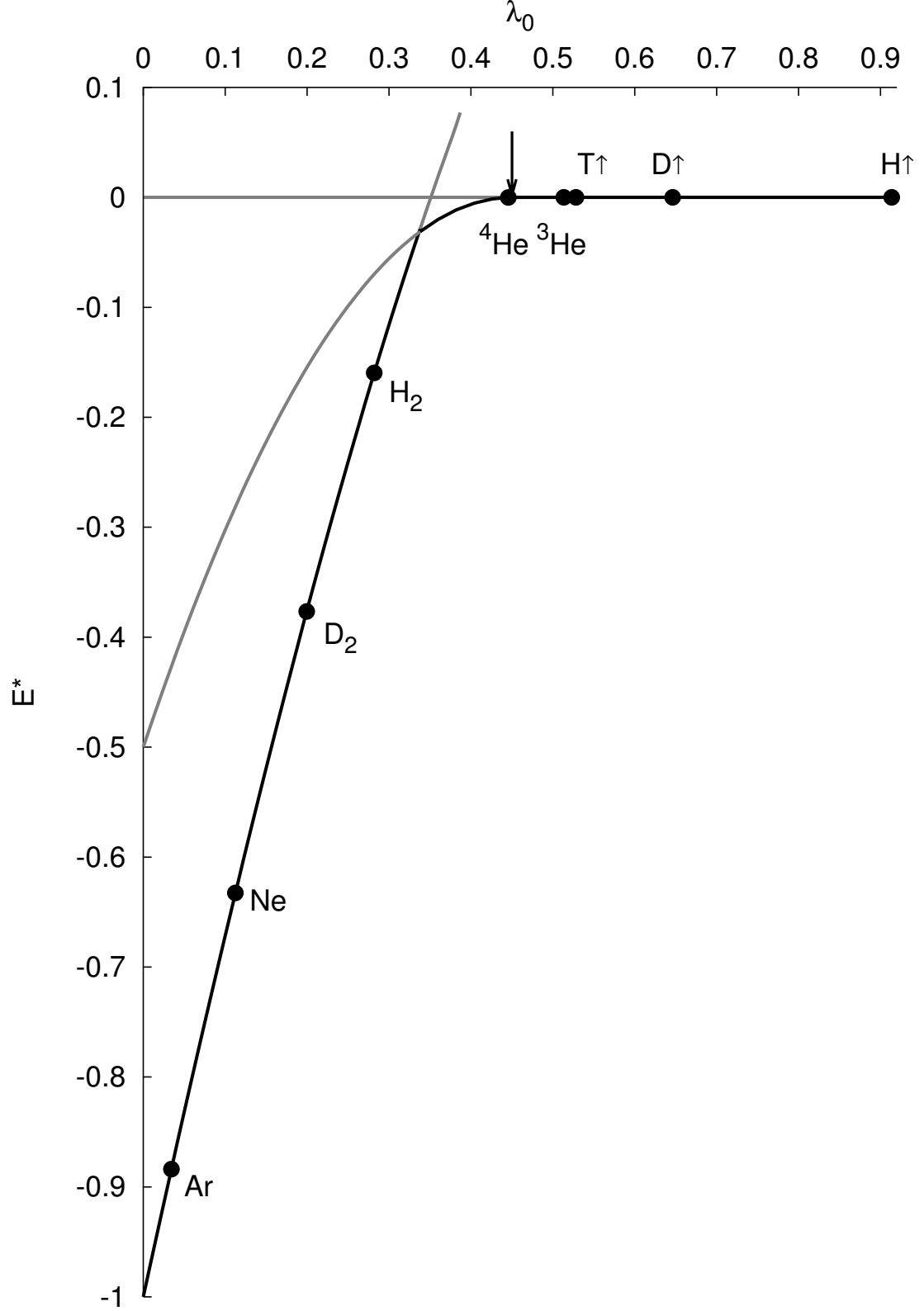
In order to construct the phase diagram of the system we need to compare all the branches of the reduced energy function (1.5); for a given De Boer's number λ_0 the branch with the lowest $E^*(\lambda_0)$ singles out the ground-state. The outcome is shown in Fig. 1.6 where the reduced energy per particle of the Luttinger liquid, Eqs.(1.37) and (1.38), is drawn together with those for diatomic, Eq.(1.7), and monoatomic, $E_{mono}^*(\lambda_0) = 0$, gases.

We see that as λ_0 increases away from the classical limit, $\lambda_0 = 0$, the reduced energy per particle of the Luttinger liquid increases, and at $\lambda_{0ev} \simeq 0.3365$ a crossing with the dimer gas energy curve, Eq.(1.7), takes place - the liquid phase evaporates into the diatomic gas via a discontinuous transition. We note that the Luttinger liquid can still coexist (as a metastable state) with the gas phases in the narrow range $0.3365 \lesssim \lambda_0 \lesssim 0.3896$. This is shown by the grey scale part of the energy curve.

The diatomic gas is the ground-state of the system in the range $0.3365 \lesssim \lambda_0 < \sqrt{2}/\pi \simeq 0.4502$: at $\lambda_{02} = \sqrt{2}/\pi$ it undergoes a continuous dissociation transition into a monoatomic gas. For $\lambda_0 > \sqrt{2}/\pi$ quantum fluctuations are too strong and no bound state can exist: a monoatomic gas is the only possible state of the system.

In determining the ground-state one needs to take into account all possible competing phases of

Figure 1.6: The dependencies of the reduced energy per particle on De Boer's number λ_0 (1.4) for various phases. The bold parts of the curves correspond to ground states of the system while the grey scale segments indicate metastable states. The loci of a series of substances are shown by solid dots, and the arrow pointing down is the dimer dissociation threshold.



the system in question. We however neglected the possibility that trimers (and generally N -atomic molecules) may come into play. This is because we only know how to treat the $N = 1, 2, \infty$ cases in a controlled fashion. Although it appears unlikely, we cannot rule out that for sufficiently large λ_0 , $N > 2$ -atomic gases might become relevant; resolving this issue is left for future study.

A critical reader still may argue that our prediction of the diatomic gas phase is an artifact of the variational treatment - the exact energy curve corresponding to the Luttinger liquid may go lower than what Fig.1.6 shows. If this is the case, then the dimer gas ground state may disappear altogether.

A finite-pressure treatment described next provides additional evidence that the physics is incomplete with only a liquid and monoatomic gas present.

1.5 Finite pressure

At zero pressure there is a qualitative difference between a liquid which is a bound many-body state and a gas which is a collection of infinitely far separated particles. Arbitrarily small confining pressure necessarily brings a gas to a finite density. As a result the two gas phases previously discussed turn into Luttinger liquids. The difference between the “parent” Luttinger liquid and what used to be a monoatomic gas becomes merely quantitative - they will have differing densities, sound velocities, correlation exponents and other properties. The liquid of dimers is more complicated as in addition its oscillation spectrum will have an extra optical branch.

To avoid confusion we will keep referring to these pressure-induced Luttinger liquids as gases. As the pressure and De Boer’s number λ_0 change, they may undergo gas-gas and gas-liquid transitions. At sufficiently large pressure and λ_0 the quantitative difference between the gases and the liquid must disappear.

In what follows we will not be able to discuss these transitions as at the moment it is unclear how to describe the effect of pressure on the diatomic gas phase in a controlled fashion. On the other hand, the generalization of our formalism to both monoatomic gasses and Luttinger liquids is straightforward. Thus we will restrict ourselves to finding ranges of existence of these phases.

The difference between the liquid and gas becomes most extreme at *negative* pressure. Here the liquid may still exist as a metastable state while the gas phase is impossible.

In one dimension the pressure has dimensionality of a force. Assume our system is compressed

by a constant force p applied to its ends. The system responds by exerting an *outward* force of magnitude p on the compressing agent which corresponds to the definition of positive pressure. Similarly, if the system is stretched by an external force, it responds by exerting an *inward* force on the stretching agent which corresponds to the definition of negative pressure. These two cases will be distinguished by the sign of p .

Since every particle of the system is in mechanical equilibrium, the whole effect of pressure translates into replacing the bond potential $V(h)$ by $V(h) + ph$, the total potential energy in the external field [23]. Then the finite-pressure analog of Eq.(1.20) becomes

$$\begin{aligned} E^*(\gamma, Q) &= v^{-1} \ln(1 + \gamma) - 2e^{Q_0 - Q}(1 + \gamma^{-1})^\lambda \\ &+ e^{2(Q_0 - Q)}(1 + \gamma^{-1})^{4\lambda} + p^*Q, \end{aligned} \quad (1.42)$$

where $p^* = pl/\epsilon$ is the reduced pressure. Eq.(1.42) should be minimized with respect to γ and Q , and then $v = \lambda/\pi\lambda_0^2$ and $\gamma = 2/\pi$ substituted in the outcome will guarantee translational invariance. The results are finite pressure analogs of Eqs.(1.34), (1.36), and (1.38):

$$\begin{aligned} E^*(Q) &= (\pi\lambda_0^2/\lambda) \ln(1 + 2/\pi) - 2e^{Q_0 - Q + \lambda \ln(1 + \pi/2)} \\ &+ e^{2(Q_0 - Q) + 4\lambda \ln(1 + \pi/2)} + p^*Q, \end{aligned} \quad (1.43)$$

$$\begin{aligned} Q &= Q_0 + 3\lambda \ln(1 + \pi/2) \\ &- \ln[(1 + \sqrt{1 + 2p^*e^{2\lambda \ln(1 + \pi/2)}})/2], \end{aligned} \quad (1.44)$$

$$\begin{aligned} \lambda_0 &= \lambda e^{-\lambda \ln(1 + \pi/2)} [(1 + 2p^*e^{2\lambda \ln(1 + \pi/2)}) \\ &+ \sqrt{1 + 2p^*e^{2\lambda \ln(1 + \pi/2)}}/2]^{1/2} \end{aligned} \quad (1.45)$$

The expressions for the reduced rms fluctuation (1.35) and Debye temperature (1.41) as functions of λ remain the same while the $\lambda(\lambda_0)$ dependence is determined by (1.45). Similarly the reduced sound velocity is given by the first representation of Eq.(1.40) with Q and λ determined by Eqs.(1.44) and (1.45), respectively.

We note that the parameter λ (1.17) now accounts for both the effects of pressure and zero-point

motion.

1.5.1 Classical limit

In the classical limit $\lambda_0, \lambda \rightarrow 0$ and $p^* > 0$ the position of the minimum of (1.43) given by (1.44) naturally shifts to values smaller than Q_0 . In addition Eq.(1.44) predicts that at a very large pressure $p_0^* \simeq 2e^{2Q_0} = 2e^{10} \simeq 44000$ the bond length vanishes. This conclusion is an artifact because for small interparticle separation the Morse potential underestimates the true strength of overlap repulsion - the bond length can only go to zero in the limit of infinite pressure. This flaw implies that only $p^* \ll p_0^*$ results are credible which is not really restrictive as p_0^* is unrealistically large.

The pressure dependence of the reduced sound velocity follows from the first representation of (1.40), and Eqs.(1.44) and (1.45).

For not very large negative pressure the pair potential (1.43) has a minimum given by (1.44) and a maximum - the “broken” ground state of the chain is separated from the metastable stretched crystal by a potential barrier. As the magnitude of the pressure increases, the amplitude of the barrier decreases, and at the classical limit of mechanical stability, $p_{ms}^* = -1/2$, the barrier disappears altogether - no bound state can exist for $p^* < -1/2$. As the pressure approaches the limit of mechanical stability from above, the reduced bond length tends to $Q = Q_0 + \ln 2$ while the reduced sound velocity vanishes as $(1 + 2p^*)^{1/4}$ in agreement with general arguments of Ref.[23].

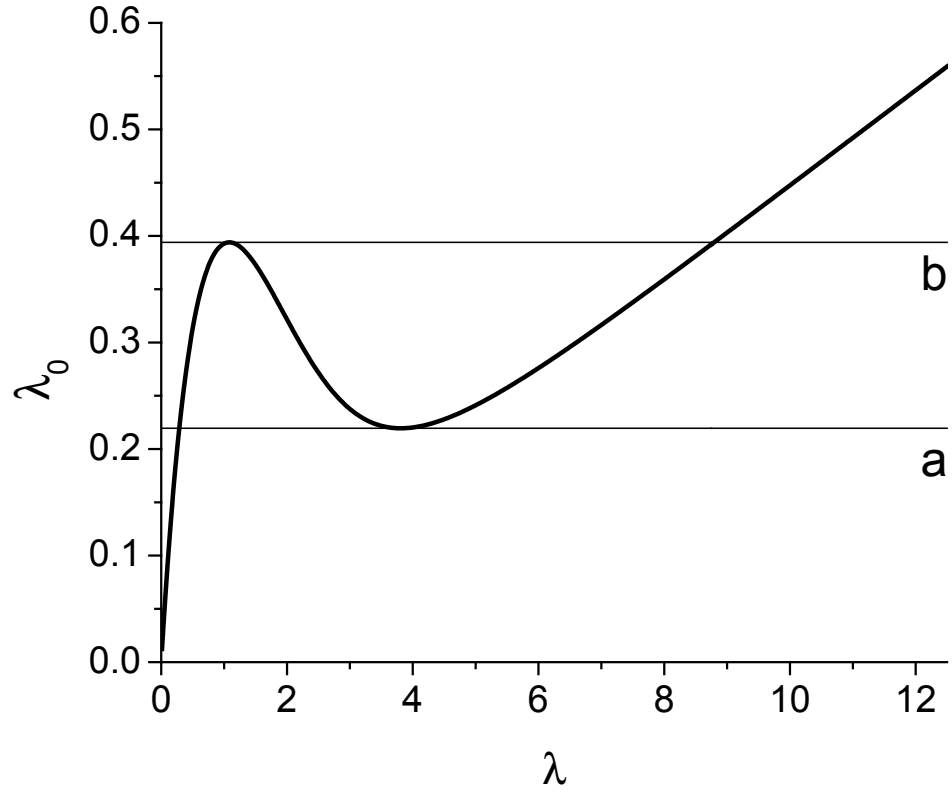
1.5.2 Quantum case

With quantum effects included, the pressure at which the bond length vanishes (and the Morse potential approximation fails) will be even larger than its classical counterpart as zero-point motion counteracts the compression. Therefore the restriction $p^* \ll p_0^*$ remains unchanged in the quantum case.

Since quantum fluctuations lead to the expansion and softening of the liquid phase, a smaller in magnitude negative pressure will suffice to destabilize the liquid - the dependence of the limit of mechanical stability on De Boer’s number (1.4), $p_{ms}^*(\lambda_0)$, should be a monotonically increasing function of λ_0 satisfying $p_{ms}^*(0) = -1/2$ (classical limit) and $p_{ms}^*(\lambda_{0s}) = 0$ (zero-pressure limit of stability of the Luttinger liquid).

For $p^* = 0$ the right-hand-side of (1.45) vanishes both at $\lambda = 0$ and $\lambda = \infty$ reaching a maximum at $\lambda = \lambda_s$ which determined the limit of stability of the liquid in the zero-pressure case (see Section

Figure 1.7: The $\lambda_0(\lambda)$ dependence, Eq.(1.45), for sufficiently small positive pressure ($p^* = 0.002$ is shown). The lines of fixed $\lambda_0 = \lambda_{0a,b}$ are the limits of stability of gas and liquid, respectively.



1.4.3). For finite positive pressure and $\lambda \rightarrow \infty$ the right-hand-side of (1.45) behaves as $p^{*1/2}\lambda$ which implies that for not very large p^* the $\lambda_0(\lambda)$ dependence is a nonmonotonic function which has both a maximum and a minimum. The position of the minimum shifts to infinity as $p^* \rightarrow 0$. An example of the $\lambda_0(\lambda)$ dependence, Eq.(1.45), for sufficiently small positive pressure is displayed in Fig.1.7 where we also show two lines of constant λ_0 to help identify possible phases of the system.

For fixed small positive pressure and $\lambda_0 < \lambda_{0a}$ Eq.(1.45) has a unique solution for λ describing the liquid. For $\lambda_{0a} < \lambda_0 < \lambda_{0b}$ Eq.(1.45) has three solutions. Out of them only the smallest (corresponding to liquid) and the largest (corresponding to gas) are physical. For $\lambda_0 > \lambda_{0b}$ there is only one solution for λ describing a gas phase. The liquid and gas phases can coexist in the range of λ_0 between the limit of existence of the gas phase, λ_{0a} , and that of liquid, λ_{0b} .

If the condition

$$p^* \exp[(2\lambda_0/p^{*1/2}) \ln(1 + \pi/2)] \gg 1 \quad (1.46)$$

holds, then the explicit λ_0 -dependence of the properties of the gas phase can be deduced from Eqs.(1.44) and (1.45)

$$\lambda = \lambda_0/p^{*1/2} \quad (1.47)$$

$$\begin{aligned} Q - Q_0 = & -(1/2) \ln(p^*/2) \\ & + \frac{1}{\sqrt{p^*}} [2\lambda_0 \ln(1 + \frac{\pi}{2}) - \frac{1}{\sqrt{2}} e^{-(\lambda_0/p^{*1/2}) \ln(1 + \frac{\pi}{2})}] \end{aligned} \quad (1.48)$$

We note the range of applicability of these results is rather wide - small pressure and nonzero λ_0 , large pressure and arbitrary λ_0 , and arbitrary pressure and large λ_0 . The pressure dependence of the reduced length per particle Q (1.48) is the equation of state of the Morse gas.

As the pressure increases, the distance between the minimum and maximum of the right-hand-side of (1.45) decreases, and at the critical pressure $p^* = p_c^* \simeq 0.0185$ the difference between the properties of liquid and gas disappears for the first time. At this pressure and $\lambda_{0c} \simeq 0.4387$ the size of the liquid-gas coexistence region shrinks to a point.

The negative pressure analysis is similar to what we did for $p^* = 0$ in Section 1.4.3. For negative pressure of sufficiently small magnitude the right-hand-side of Eq.(1.45) vanishes both at $\lambda = 0$ and $1 + 2p^*e^{2\lambda \ln(1 + \pi/2)} = 0$ reaching a maximum in between. If De Boer's parameter λ_0 is below this maximum, then Eq.(1.45) has two solutions for λ . The smaller (physical) solution describes

a metastable Luttinger liquid. As λ_0 increases, the two solutions approach each other. When λ_0 reaches the maximum of the right-hand-side of (1.45), we are at the limit of mechanical stability of the system - no liquid can exist for larger λ_0 .

Alternatively, for sufficiently small fixed λ_0 the height of the maximum of (1.45) decreases upon increase of the magnitude of pressure, and at some $p_{ms}^*(\lambda_0)$ the maximum of (1.45) reaches the level of λ_0 thus bringing the system to the limit of mechanical stability. It is curious that in the quantum case the “liquid” solution disappears *before* the condition $1 + 2p^*e^{2\lambda \ln(1+\pi/2)} = 0$ is reached. Therefore at the stability threshold both the energy barrier (between “broken” ground-state and stretched metastable liquid) and sound velocity remain finite. Only in the classical limit $\lambda_0 \rightarrow 0$ do these quantities vanish.

The pressure-De Boer’s parameter diagram showing ranges of existence of liquid and gas is displayed in Fig. 1.8.

We deliberately selected different scales on the positive and negative parts of the pressure axis in order to be able to show the complete picture. As a result of this choice there is an illusory change of slope of the line of mechanical stability of the liquid at zero pressure - in reality the $p_{ms}^*(\lambda_0)$ dependence is smooth.

The point C having coordinates $\lambda_{0c} \simeq 0.4387$, $p_c^* \simeq 0.0185$ where the limits of existence of liquid and gas meet is a candidate for the liquid-gas critical point. Then the line of a liquid-gas evaporation transition should also pass through C. This curve, found by equating the ground-state energy (1.43) for both phases is shown in Fig. 1.8 by a dotted line. It *does not* end at C, and everywhere within the DC segment of the metastability line the Luttinger liquid has lower energy than the gas. These results imply that a direct liquid-monoatomic gas transition is impossible. Another gas phase, diatomic, must intervene. Although the existence of this phase will set phase boundaries at finite pressure, it will not affect the ranges of existence of the Luttinger liquid and monoatomic gas.

Other finite pressure properties of the system can be readily found. As an example, Fig. 1.9 illustrates the dependence of the reduced quantum expansion $Q - Q_0$ on De Boer’s number λ_0 for three different pressures. The curve of Fig. 1.9a shows the expansion of the Luttinger liquid due to the combined effect of zero-point motion and negative pressure of sufficiently large magnitude ($p^* = -0.1$ was used). The end point of the dependence is the limit of mechanical stability of the liquid. In Fig. 1.9b the pressure is selected to be within the region of the liquid-gas coexistence ($p^* = 0.002$ was used). As a result the quantum expansion dependence is not unique: the lower (larger density) curve

Figure 1.8: The $p^*(\lambda_0)$ diagram showing ranges of existence of liquid and monoatomic gas phases. Different scales are selected on the positive and negative parts of the pressure axis. The liquid and gas can be in equilibrium along the dotted line.

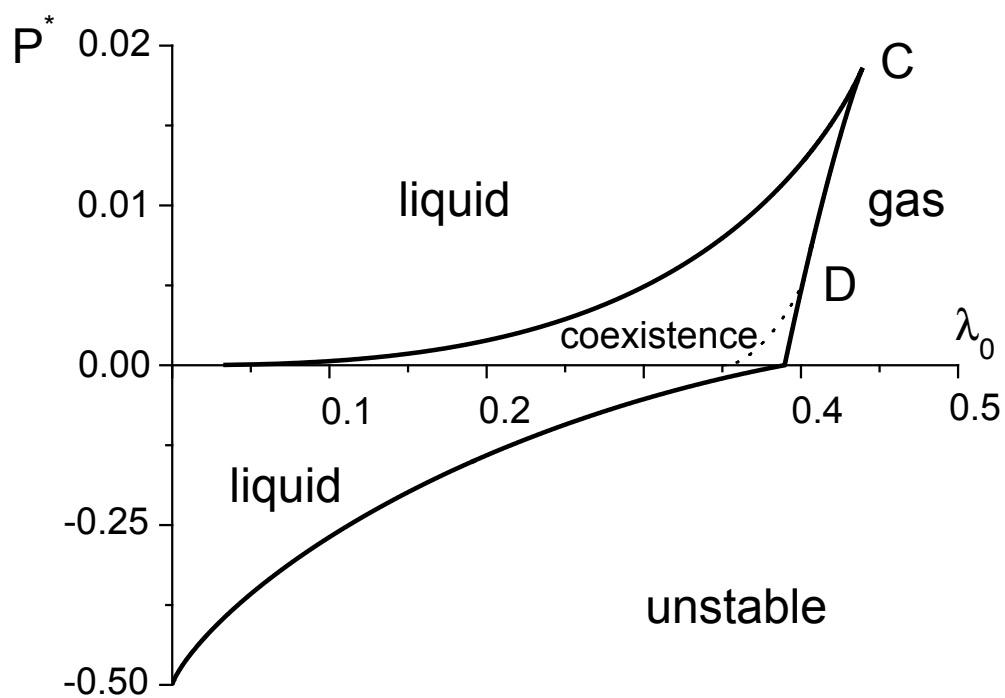


Figure 1.9: The dependence of the reduced quantum expansion $Q - Q_0$ on De Boer's parameter λ_0 at a negative pressure of large magnitude (a), within the liquid-gas coexistence region (b), and past the point C of Fig. 1.8 (c).

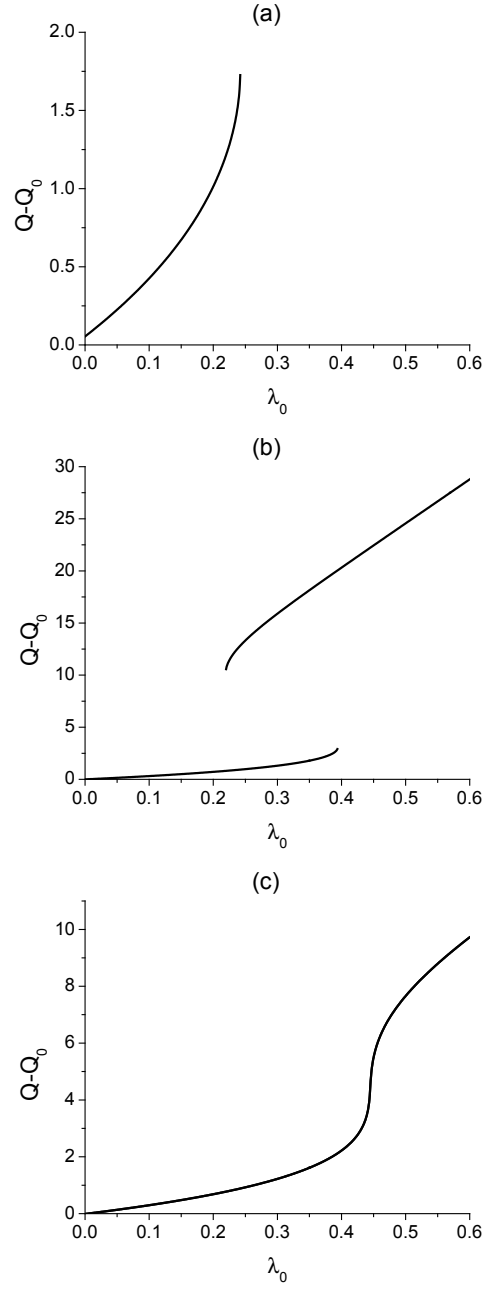


Table 1.1: Morse parameters for a series of molecular substances and some of their computed properties at zero pressure. Substances are arranged in the order of decrease of their De Boer's number λ_0 . Blank entries correspond to gas ground states when interparticle separation is infinite.

| | m a.u. | ϵ K | ℓ Å | H_0 Å | λ_0 | $Q - Q_0$ | Q | $-E^*$ 10^{-3} |
|--------------|-------------|-----------------|-------------|------------|-------------|-----------|-------|---------------------|
| $H \uparrow$ | 1.008 | 6.19 | .6869 | 4.153 | .9136 | | | 0 |
| $D \uparrow$ | 2.014 | 6.19 | .6869 | 4.153 | .6463 | | | 0 |
| $T \uparrow$ | 3.016 | 6.19 | .6869 | 4.153 | .5281 | | | 0 |
| 3He | 3.016 | 10.8 | .5350 | 2.980 | .5134 | | | 0 |
| 4He | 4.003 | 10.8 | .5350 | 2.980 | .4456 | | | .0509 |
| H_2 | 2.016 | 32.2 | .6900 | 3.440 | .2819 | 1.1860 | 6.172 | 159.6 |
| D_2 | 4.028 | 32.2 | .6900 | 3.440 | .1994 | .7178 | 5.703 | 376.6 |
| Ne | 20.18 | 35.6 | .5200 | 3.110 | .1124 | .3591 | 6.340 | 632.6 |
| Ar | 39.95 | 120 | .6600 | 3.860 | .0343 | .1005 | 5.949 | 883.9 |

corresponds to the liquid while the upper (lower density) curve is for the monoatomic gas. The end of the “liquid” curve and the beginning of the “gas” curve are limits of existence of these phases. In Fig. 1.9c the pressure is selected to satisfy the condition $p^* > p_c^*$ i.e. past the point C of Fig. 1.8. Now there is no quantitative difference between liquid and gas. The presence of a relatively steep part around $\lambda_0 \simeq 0.44$ is the effect of the proximity of $p^* = 0.02$ to $p_c^* \simeq 0.0185$.

To test the limits of applicability of our theory we also investigated the reduced sound velocity and relative bond fluctuation at various pressures. We found that at fixed λ_0 the reduced sound velocity initially increases with pressure but then at pressures exceeding the level of about 6000 or larger, it begins to decrease vanishing at the point where the bond length Q vanishes. The fall and vanishing of the sound velocity do not correspond to physical reality and have their origin in the inadequacy of the Morse potential approximation at small interparticle distances. Similarly, the relative fluctuation diverges upon approaching the nonphysical $Q = 0$ point. These artifacts do not pose practical limitations to our theory because they occur at unrealistically large pressures. We verified that if we limit ourselves to pressures not exceeding 5000, then the relative fluctuation is smaller than 0.5, and the behavior of other properties of the system is in agreement with physical expectations.

1.6 Applications and Discussion

Fitting two-body potentials of molecular substances into the Morse form can provide us with the depth of the potential well ϵ , the interaction range l , and the position of the potential minimum H_0 . Supplemented by the masses of the underlying particles, this information is an input of our theory which then allows us to determine De Boer's quantum parameter λ_0 (1.4), the ground state and virtually any property.

The fitting procedure can introduce uncertainties because real two-body interactions do not have the Morse form. We already know that the Morse potential underestimates the strength of the overlap repulsion at short distances but as long as the reduced pressure does not exceed 5000, this flaw is practically irrelevant.

The Morse potential also underestimates the magnitude of Van der Waals attraction at large distances. We found that in the condensed state this shortcoming can be kept under the control by carrying out a Morse potential fit in a range of interparticle distances followed by a consistency check verifying that the segment of most probable particle location (formed by computed equilibrium bond length plus/minus its rms fluctuation) is well inside the fitting range.

The first four columns of Table 1.1 represent Morse parameters of various molecular substances which are used to compute De Boer's number λ_0 shown in the fifth column. The remaining three columns are reduced quantum expansion $Q - Q_0$, bond length Q , and the energy per particle E^* (all at zero pressure) calculated using the theory developed in this paper. The loci of all these substances are also indicated on the reduced energy curve $E^*(\lambda_0)$ of Fig. 1.6. For the substances whose ground state is the Luttinger liquid, Fig. 1.5a also shows the magnitudes of the reduced classical bond length Q_0 and its relative fluctuation f^*/Q , while Fig. 1.5b gives the values of the Luttinger liquid exponent g .

In computing these properties we also assumed that the three-dimensional form of the interaction does not change upon one-dimensional confinement of the particles and that translational symmetry is preserved. Both these assumptions are approximations if the confinement is achieved in carbon nanotube bundles because interparticle interaction is mediated by the carbon environment [35] while the axial motion takes place in a periodic potential [15]. The former effect generally weakens interparticle attraction at large distances thus making the system more quantum. On the other hand the external periodic potential due to the carbon environment has an opposite effect leading

to upward renormalization of the mass. Therefore the properties of strictly one-dimensional matter may differ qualitatively from those of the matter inside nanotube bundles. The effect of an axial periodic potential may be even more dramatic, and the effective mass approximation insufficient if the corrugation is strong enough to introduce a commensurate-incommensurate phase transition [36]. This potentially important effect is beyond the scope of our method and cannot be discussed here.

Before considering individual substances it is useful to look at the properties of one-dimensional matter as a whole and compare them with those of laboratory substances. The corresponding states analysis of three-dimensional molecular matter is based on the Lennard-Jones pair potential and except for the vicinity of the classical limit $\lambda_0 = 0$, it is empirical [2, 3, 4].

The substances in Table 1.1 are arranged in the order of decreasing De Boer's number λ_0 which is naturally the same as in three dimensions. The main qualitative difference from the ordinary substances occurs because of the dominant role played by zero-point motion which in one dimension forbids the crystal ground state. We find that spin-polarized isotopes of hydrogen (hydrogen $H \uparrow$, deuterium $D \uparrow$, and tritium $T \uparrow$) and ${}^3\text{He}$ are monoatomic gases, ${}^4\text{He}$ is diatomic gas, while molecular hydrogen and heavier substances are Luttinger liquids. If we view the Luttinger liquid as the counterpart of the crystal in three dimensions, then the bold part of the reduced energy curve, Fig. 1.6, closely resembles its three-dimensional counterpart [3]. There is a change of slope somewhere between H_2 and ${}^4\text{He}$ which in our case is the dissociation of the Luttinger liquid into a diatomic gas while in the three-dimensional world it is a melting transition.

Our dependence of the reduced Debye temperature θ^* on De Boer's number λ_0 , Fig. 1.5b, also looks very similar to its three-dimensional counterpart [2], and even empirical values of the reduced Debye temperature are close to their computed one-dimensional analogs. We also find that the $\theta^*(\lambda_0)$ dependence has a maximum somewhere past molecular hydrogen; from empirical data it seems impossible to tell whether this effect is present or not in three dimensions.

Before comparing quantum expansion in one and three dimensions, we note that the quantum theorem of the corresponding states applied to the Lennard-Jones system predicts that the reduced volume per particle (length in one dimension) Q is only determined by De Boer's quantum parameter λ_0 . At the same time for the Morse system the analogous statement is valid for the reduced quantum expansion $Q - Q_0$. However the inspection of Table 1.1 (see also Fig. 1.5b) shows that the values of the reduced classical bond length $Q_0 = H_0/l$ belong to the relatively narrow interval roughly

between 5 and 6.3. Therefore the variation of Q_0 from substance to substance can be ignored and within experimental error our results can be compared to their empirical counterparts [2, 3]. Again we find that the λ_0 dependencies of the reduced quantum expansion in one and three dimensions are qualitatively similar.

In three dimensions all these properties can be computed perturbatively in the $\lambda_0 \rightarrow 0$ limit [2, 3] with the conclusion that to leading order $E^*(\lambda_0) - E^*(0)$, $Q - Q_0$, and θ^* all vanish linearly with λ_0 . This behavior is identical to the $\lambda_0 \rightarrow 0$ limit of our theory.

As a final comment, we note that from the viewpoint of their electron transport properties all the molecular substances are normally insulators as they have completely filled electronic shells. However at sufficiently large pressure when electron wave functions of neighboring molecules overlap considerably, any substance should turn into a metal [37]. At that point our “molecular” approximation describing many-body physics in terms of additive two-body interactions fails. Typically this happens at a very large pressure, and a different approach explicitly accounting for the dynamics of the electron degrees of freedom is necessary. This complex problem is beyond the scope of the present paper. For the case of molecular hydrogen, however, we will be able to estimate this critical pressure when the metal-insulator transition takes place without leaving the framework of our method.

In subsequent discussions of individual substances we first present the results based on the pair interaction potential in free space. These conclusions are robust. On the other hand, our comments about the properties of matter inside nanotubes are speculative as they rely on the assumption that the effect of carbon environment can be accommodated within the framework of our method by adjusting De Boer’s parameter λ_0 . It is also important to keep in mind that inside nanotube bundles there will be an additional interaction between different one-dimensional channels filled with absorbed substances. This interaction is responsible for exotic crossover effects which can be viewed as an effective change of space dimensionality [38]. These effects are also beyond the scope of our one-dimensional theory.

1.6.1 Spin-polarized hydrogen and its isotopes

The pair interaction between two particles of the spin-polarized hydrogen family has been computed by Kolos and Wolniewicz [39]. Etters, Dugan and Palmer [40] have found a very good Morse fit to the Kolos-Wolniewicz potential; the Morse parameters shown in Table 1.1 are their values.

Compared to the other elements in Table 1.1, these substances have the shallowest potential well which is only $6.19K$ deep. Combined with its smallest mass, this makes $H \uparrow$ the “quantummost” element with $\lambda_0 = 0.9136$. Spin-polarized deuterium $D \uparrow$ is second in line with $\lambda_0 = 0.6463$ while spin-polarized tritium $T \uparrow$ takes the third place, $\lambda_0 = 0.5281$. All these elements are monoatomic gases at zero pressure as can be seen from Fig. 1.6. On the other hand at zero pressure in three dimensions the heaviest of the family, $T \uparrow$, forms a liquid while $H \uparrow$ and $D \uparrow$ are gases [40].

External pressure confines these gases to a finite density but because De Boer’s numbers are larger than $\lambda_{0c} \simeq 0.4387$ corresponding to point C of Fig. 1.8, applying pressure is not going to turn them into liquids.

1.6.2 Helium

The pair interaction between two helium atoms is accurately described by the semi-empirical Aziz potential [41] which is $10.8K$ deep; this is the second entry in Table 1.1. The authors of Ref.[19] proposed the Morse fit of the Aziz potential with the parameters $l = 0.5828\text{\AA}$ and $H_0 = 2.89\text{\AA}$ claiming that “the integrated square of the deviation of the fit from the Aziz potential does not exceed 1% in the range of localization of a He atom”. These parameters produce $\lambda_0 \simeq 0.41$ for 4He which according to our theory makes it a diatomic gas. It is indeed experimentally known [42] that 4He can form very large dimers with the bond length of 52\AA . We verified however that at interparticle distances that large the Morse fit proposed in Ref.[19] is very poor.

Our own attempts to improve the fit increased the value of λ_0 bringing it into a narrow vicinity of the dimer dissociation threshold $\lambda_{02} = \sqrt{2}/\pi$, and without extra knowledge we could not make a decision whether λ_0 is larger or smaller than λ_{02} . We resolved this dilemma by invoking the experimental result [42] that the binding energy of the 4He dimer is $-1.1mK$. Halving this value and dividing the outcome by $10.8K$, the depth of the $He - He$ potential well, produces the last entry in Table 1.1, the reduced energy per particle of the diatomic gas. This can be substituted into Eq.(1.7) to recover the fifth entry, $\lambda_0 = 0.4456$. As expected, this is only marginally smaller than the dimer dissociation threshold λ_{02} . Using the definition of De Boer’s number, Eq.(1.4), we can now recover the interaction range (the third entry in Table 1.1) to be $l = 0.5350\text{\AA}$. Finally the position of the minimum of the Morse potential $H_0 = 2.980\text{\AA}$ was chosen to optimize the fit.

Upon application of pressure the gas of 4He dimers will turn into a Luttinger liquid; calculation of the properties of this dimer liquid is beyond the scope of our method.

De Boer's quantum parameter for ${}^3\text{He}$ can be obtained from that for ${}^4\text{He}$ by invoking their mass ratio. This gives us the value quoted in the fifth column of the ${}^3\text{He}$ row in Table 1.1. It is higher than the dimer dissociation threshold λ_{02} thus ruling out earlier prediction [43] that ${}^3\text{He}$ can form a dimer in one dimension. A many-body system of ${}^3\text{He}$ particles in one dimension will form a monoatomic gas with properties close to those of spin-polarized tritium. Similar to $T \uparrow$, the ${}^3\text{He}$ gas will not condense under pressure.

Our result that ${}^4\text{He}$ forms a diatomic gas strictly in one dimension is in variance with earlier work [15, 16, 18] which predicted a liquid ground state with a binding energy on the order of a few to tens of mK . This is the same order of magnitude as the energy per particle in the diatomic gas. However Refs.[16, 18] also predict a liquid-solid phase transition which is forbidden in one dimension.

In applying our results to nanotubes one has to bear in mind that ${}^4\text{He}$ atoms are strongly attracted to the interstitial channels inside nanotube bundles. The corrugation felt by the individual atom is so strong that the effective mass enhancement is very large: $m^* \simeq 18m$ [44]. There is also a weaker opposing effect: 28% reduction in the well depth of the pair interaction mediated by the carbon environment [35]. Combining these effects and assuming the interaction range does not change significantly, we find that De Boer's number will *decrease* by a factor of 3.6 away from its purely one-dimensional value thus implying a liquid ground state. Similar outcome is expected for ${}^3\text{He}$.

1.6.3 Molecular hydrogen

The pair interaction between two hydrogen (or deuterium) molecules is commonly described by the semi-empirical Silvera-Goldman potential [21]. Fig.1.1 shows this potential together with its Morse fit; the calculated Morse parameters are quoted in Table 1.1.

As can be deduced from Figs.1.5 and 1.6, and Table 1.1 the many-body system of H_2 molecules is a Luttinger liquid with strongest effects of zero-point motion. It is characterized by $-5.14K$ cohesive energy (ground-state energy per particle) which is an 84% reduction in magnitude away from the depth of the $H_2 - H_2$ potential, largest Debye temperature of $121K$, largest Luttinger liquid exponent $g \simeq 0.1$, largest quantum expansion of 0.82\AA , and largest, just under 18%, relative fluctuation of the bond length.

The equilibrium distance between the H_2 molecules is 4.26\AA . As can be seen from Fig.1.1 in a range around the equilibrium bond length significantly exceeding its rms fluctuation the Morse

potential is a very good approximation to the Silvera-Goldman potential. The fit worsens at interparticle separations exceeding 5\AA ; there are also deviations from the Silvera-Goldman potential at distances smaller than 3\AA . However at these compressions Hemley and collaborators [45] have found a softening effect unaccounted for by the Silvera-Goldman potential. We verified that the Morse potential shown in Fig.1.1 provides a very good fit to the Hemley-corrected version of the Silvera-Goldman potential.

Previous work [17] finds a liquid ground-state with the energy per particle to be $-4.8K$ and the bond length of 4.6\AA . These values are close to our results. However we disagree with the existence of a liquid-solid transition found in Ref.[17] at higher density; such a transition is forbidden in one dimension.

The building blocks of one-dimensional molecular hydrogen are H_2 molecules whose size of 0.75\AA [37] is significantly smaller than the computed intermolecular distance of 4.26\AA . Such structure can be understood qualitatively from a complementary viewpoint:

There is exactly one electron per every hydrogen atom, and if the protons are arranged equidistantly, then the valence band is half-full, and the resulting system is an alkali metal [1]. However Peierls [46] noticed that in one dimension the energy can be further lowered by displacing every second nucleus by a prescribed distance. As a result of the period doubling the valence band becomes full, and the resulting dimer chain is an insulator. We conclude that one-dimensional molecular hydrogen is an example of Peierls-distorted one-dimensional structure; the dimers are hydrogen molecules.

Peierls' arguments rely on an adiabatic approximation which ignores zero-point motion of the nuclei; the former may change the answer qualitatively. Our theory which starts from interacting H_2 molecules shows that even for one-dimensional hydrogen the ground-state is a Peierls-distorted insulator despite strong quantum fluctuations.

This conclusion may change upon application of pressure which brings hydrogen molecules closer to each other and increases relative fluctuation of the bond length. We argue that the distortion disappears and thus an insulator-metal transition takes place when all the hydrogen atoms become translationally identical. This transition is a one-dimensional version of the metallization transition predicted by Wigner and Huntington [37]. In one dimension the mechanism of the transition consists in “undoing” the Peierls distortion.

Since the bond between the two hydrogen molecules is significantly softer than that holding the

H_2 molecule together, we assume that upon application of pressure, only the former decreases. Thus the translational equivalence of all the hydrogen atoms will be achieved when intermolecular spacing reaches the value of order 1.5\AA , twice the size of the H_2 molecule. With zero-pressure intermolecular spacing being 4.26\AA , this corresponds to compression by a factor of 2.84. The corresponding reduced pressure $p^* \gg 1$ can be found by inverting Eq.(1.48):

$$p^* \simeq 2e^{2\{Q_0 - Q + [\sqrt{2}\lambda_0 \ln(1 + \frac{\pi}{2}) - \frac{1}{2}]\}e^{Q - Q_0}} \quad (1.49)$$

Substituting here $Q_0 = 4.986$, $Q = H/l = 2.174$, and $\lambda_0 = 0.2819$ we arrive at the reduced pressure of 545. Our theory which does not explicitly consider electronic degrees of freedom fails in the vicinity of the inverse Peierls transition.

For molecular hydrogen in one dimension the unit of pressure is a *force* of $\epsilon/l \simeq 6.44 * 10^{-12}N$ strong. Multiplying this by 545 we find that $3.51 * 10^{-9}N$ force compressing one-dimensional hydrogen may suffice to induce a transition into a metallic state. If this force is applied at the 1\AA^2 area, then the corresponding three-dimensional pressure will be $351GPa$. We note that three-dimensional solid hydrogen subject to pressure that big still resists metallization [47]. Unfortunately the accuracy of our estimate is not great because of the exponential dependencies in (1.49) - the actual one-dimensional transition may happen at lower or larger pressures.

For hydrogen confined inside interstitial channels of carbon nanotube bundles the carbon environment effectively reduces the well depth of the pair interaction by 54% [35]. This effect alone would suffice to turn the many-body system of hydrogen molecules into a gas of $(H_2)_2$ complexes. However if the effective mass enhancement is comparable to that for He [44], the liquid ground state might be restored.

As can be seen from Fig. 1.6 and Table 1.1, the ground state of molecular deuterium is a Luttinger liquid. The quantitative difference from the properties of molecular hydrogen is solely due to the fact that D_2 has a larger mass. The cohesive energy of the one-dimensional D_2 liquid is $-12.1K$ (62% reduction in the magnitude of the $D_2 - D_2$ pair potential well), the Debye temperature is $99.8K$ while the equilibrium distance between D_2 molecules is 3.94\AA .

1.6.4 Heavier substances

While discussing the physics of molecular hydrogen in one dimension we came to the conclusion that it can be viewed as an example of a Peierls-distorted structure. The same arguments are applicable to any element with odd number of electrons: the period doubling should take place and the resulting system must be an insulator. We note that three-dimensional counterparts of these substances are metals. These observations imply that our theory is also applicable to substances which traditionally are not considered to belong to the molecular group. For example, one-dimensional lithium must be an insulating Luttinger liquid of Li_2 molecules [48]. Similar to molecular hydrogen, under pressure it should undergo a metallization transition. Had we known the pair interaction between two Li_2 molecules, we could have computed the properties of the lithium liquid. From the viewpoint of the quantum theorem of corresponding states molecular lithium is expected to occupy a place somewhere between D_2 and Ne .

Table 1.1 also contains the Morse data for Ne and Ar . They were obtained from the parameters of the Lennard-Jones interaction potential [1] which is commonly used to describe these noble gases. Some of the properties of these substances in one dimension can be found in Table 1.1 and in Figs.1.5 and 1.6. The equilibrium interparticle spacing, cohesive energy and Debye temperature can be extracted from what is shown in the same manner as was done for lighter elements. As the underlying particles become heavier, the effect of zero-point motion decreases. For elements heavier than Ar quantum fluctuations can be ignored for most practical purposes.

Chapter 2

Quantum dissociation of an edge of a Luttinger liquid

As in Chapter 1, we begin with a many-body system of identical particles of mass m with pairwise interaction $V(h)$ corresponding to molecular matter [1], given by eq. (1.2). With this choice the quantum theorem of the corresponding states [2] holds stating that every property measured in appropriate dimensionless units is only determined by the function $U(y)$, particle statistics and De Boer's number

$$\lambda_0 = \frac{\hbar}{\pi l (2m\epsilon)^{1/2}}, \quad (2.1)$$

measuring the intensity of zero-point motion.

The possibility of several bulk phases in the system translates into a corresponding number of branches of the energy as a function of λ_0 ; the lowest of them singles out the ground state of the system. When two energy curves cross, the ground state changes via a first-order phase transition. For sufficiently large λ_0 and zero pressure the ground state must correspond to individual particles infinitely far apart from each other. This is a monoatomic gas which will be chosen as the zero reference point for the energy.

As in section 1.2 we select the pair interaction potential in the Morse form [20]:

$$V(h) = \epsilon(e^{-2(h/l-Q_0)} - 2e^{-(h/l-Q_0)}), \quad (2.2)$$

where ϵ is the depth of the potential well and Q_0 is the location of the minimum of (2.2) measured in units of the potential range l . Similar to the applications of the Lennard-Jones potential to laboratory molecular systems [1], the only reason behind this choice is the possibility of analytic progress. Morse parameters for a series of molecular substances and corresponding De Boer's numbers (2.1) were computed in Ref.[53] and were given in Table 1.1. Hereafter the energy and length scales will be measured in units of ϵ and l , respectively. As appropriate for molecular substances, we restrict ourselves to nearest-neighbor interactions.

In the classical limit, $\lambda_0 = 0$, the ground state of the system is a crystal; its quantum counterpart for sufficiently small λ_0 is a Luttinger liquid [6] whose properties have been computed in Ref.[53] as follows:

The length of any bulk bond h as a function of imaginary time τ is viewed as a quantum-mechanical degree of freedom subject to the external potential $V(h)$. This bond joins together two half-infinite segments representing the rest of the system, the “bath”. After the bath is approximated by a harmonic liquid, the latter can be integrated out away from the anharmonic bond leading to a problem of the Caldeira-Leggett type [24]. The latter has been analyzed by a combination of variational and renormalization-group techniques, and it has been demonstrated that the approximation is a controlled way of dealing with the interplay of zero-point motion and anharmonicity of the two-body interaction [53]. Similar consideration applied to the edge bond of a half-infinite Luttinger liquid leads to the Euclidian action of the form

$$S_{edge} = \frac{\rho c}{8} \int_{|\omega| < \omega_D} \frac{d\omega}{2\pi} |\omega| |h(\omega)|^2 + \int d\tau V(h), \quad (2.3)$$

where ρ and c are the mass density and sound velocity, respectively, and $h(\omega)$ is the Fourier transform of the bond-length field; the frequency cutoff is given by the Debye frequency ω_D .

The calculation of the properties of the edge of a Luttinger liquid proceeds through the application to the action (2.3) of Feynman's variational principle [26] which states that for any trial action S_0 with associated ground-state energy E_0 , the system's true ground-state energy is bounded above by $E_0 + (T/\hbar) \langle S - S_0 \rangle_0$ where the zero-temperature limit $T = 0$ is taken at the end and $\langle \cdot \rangle_0$ denotes an expectation value computed with S_0 .

Similar to the bulk problem [53] the trial action is selected in the Gaussian form

$$S_0 = \frac{\rho c}{8} \left(\int_{|\omega| \leq \omega_D} \frac{d\omega}{2\pi} |\omega| |h(\omega)|^2 + \gamma \omega_D \int d\tau (h - Ql)^2 \right), \quad (2.4)$$

where dimensionless variational parameters Q and γ have a meaning of the bond length and its stiffness, respectively. Then the root-mean-square (rms) fluctuation of the bond length can be computed as

$$\langle f^2 \rangle_0^{1/2} = 2\lambda^{1/2} \ln^{1/2}(1 + \gamma^{-1}), \quad (2.5)$$

where

$$\lambda = \frac{\hbar}{\pi \rho c l^2} \quad (2.6)$$

quantifies the strength of zero-point motion in the Luttinger liquid. The binding energy of the edge particle E_{edge} is approximated by $E_0 + (T/\hbar) \langle S - S_0 \rangle_0$, i. e. by its upper bound:

$$\begin{aligned} E_{edge}(\gamma, Q) &= (\pi \lambda_0^2 / \lambda) \ln(1 + \gamma) - 2e^{Q_0 - Q} (1 + \gamma^{-1})^{2\lambda} \\ &+ e^{2(Q_0 - Q)} (1 + \gamma^{-1})^{8\lambda} \end{aligned} \quad (2.7)$$

Minimizing E_{edge} with respect to Q we arrive at the expression for the quantum expansion of the edge bond

$$Q_{edge} - Q_0 = 6\lambda \ln(1 + \gamma^{-1}) \quad (2.8)$$

Substituting this back into (2.7), E_{edge} can be written as

$$E_{edge}(\gamma) = (\pi \lambda_0^2 / \lambda) \ln(1 + \gamma) - (1 + \gamma^{-1})^{-4\lambda} \quad (2.9)$$

Minimizing Eq.(2.9) with respect to γ , and substituting the outcome back into (2.9) we find

$$\gamma = (4\lambda^2 / \pi \lambda_0^2) (1 + \gamma^{-1})^{-4\lambda} \quad (2.10)$$

and

$$E_{edge} = (\pi \lambda_0^2 / 4\lambda^2) (4\lambda \ln(1 + \gamma) - \gamma) \quad (2.11)$$

respectively. The results (2.5), (2.8), (2.10), and (2.11) should be compared with their bulk counterparts [53] Eqs. (1.35)-(1.37) which are reproduced below:

$$\langle f^2 \rangle_{0 \text{ bulk}}^{1/2} = (2\lambda)^{1/2} \ln^{1/2}(1 + \pi/2), \quad (2.12)$$

$$Q_{\text{bulk}} - Q_0 = 3\lambda \ln(1 + \pi/2), \quad (2.13)$$

$$\lambda_0 = \lambda(1 + \pi/2)^{-\lambda} \quad (2.14)$$

$$E_{\text{bulk}} = (1 + \pi/2)^{-2\lambda} (\pi\lambda \ln(1 + 2/\pi) - 1) \quad (2.15)$$

Substituting Eq.(2.14) back in Eqs.(2.10) and (2.11) brings them into a form convenient for analysis

$$\gamma = (4/\pi)(1 + \pi/2)^{2\lambda}(1 + \gamma^{-1})^{-4\lambda} \quad (2.16)$$

$$E_{\text{edge}} = (\pi/4)(1 + \pi/2)^{-2\lambda} (4\lambda \ln(1 + \gamma) - \gamma) \quad (2.17)$$

The properties of the edge as a function of the quantum parameter λ (2.6) can be computed by finding a solution $\gamma(\lambda)$ to Eq.(2.16) minimizing the energy (2.17) and substituting the outcome in the expressions for the rms fluctuation (2.5) and quantum expansion (2.8); the dependence on De Boer's number (2.1) follows from Eq.(2.14).

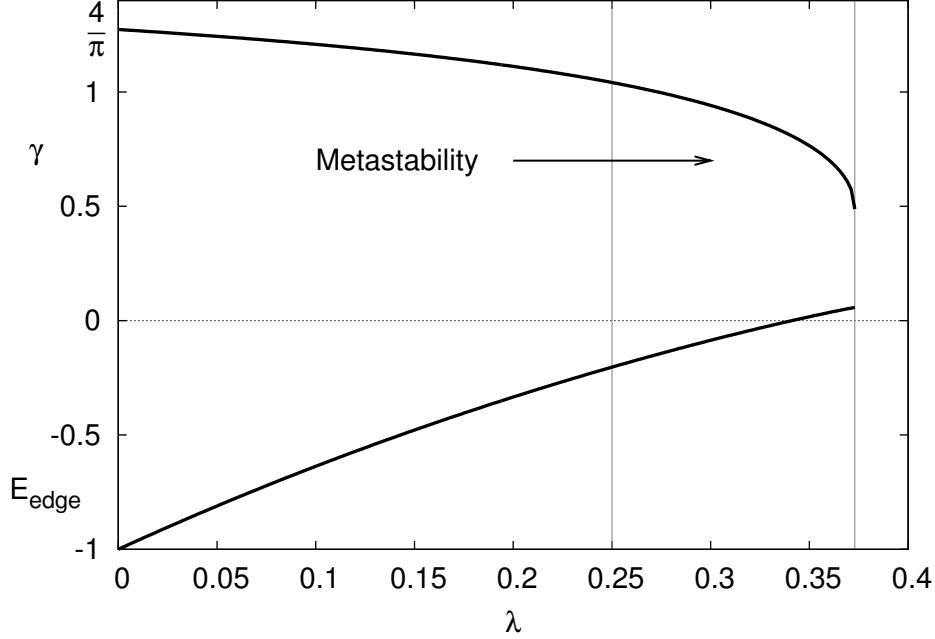
In the classical limit, $\lambda \rightarrow 0$, the only solution to (2.16) is $\gamma = 4/\pi$ with the energy (2.17) $E_{\text{edge}} = -1$ as expected. As the degree of zero-point motion intensifies (λ increases), the bond stiffness γ decreases and the energy E_{edge} increases. For finite λ Eq.(2.16) may have more than one solution. One of them is always $\gamma = 0$ corresponding to the delocalized edge particle. For large λ this solution must correspond to the lowest (zero) energy (2.17).

For $\gamma \ll 1$ the right-hand-side of Eq.(2.16) behaves as $\gamma^{4\lambda}$ while for $\gamma \rightarrow \infty$ it approaches a γ -independent limit, thus implying that (2.16) cannot have more than three solutions and that $\lambda = 1/4$ plays a special role.

For $0 < \lambda \leq 1/4$ Eq.(2.16) has two solutions and the larger of them (whose $\lambda = 0$ limit is $\gamma = 4/\pi$) corresponds to the lowest energy (2.17). For $\lambda = 1/4$ the explicit solution to (2.16) is $\gamma = (4/\pi)(1 + \pi/2)^{1/2} - 1 \simeq 1.0415$

As λ increases beyond $1/4$, Eq.(2.16) acquires a third root whose $\lambda \rightarrow 1/4 + 0$ limit is $\gamma =$

Figure 2.1: Dimensionless stiffness of the edge bond γ and corresponding binding energy of the edge particle E_{edge} of a half-infinite Luttinger liquid as functions of the quantum parameter λ (2.6). The region of metastability is confined to the $1/4 \leq \lambda \leq 0.3730$ range.

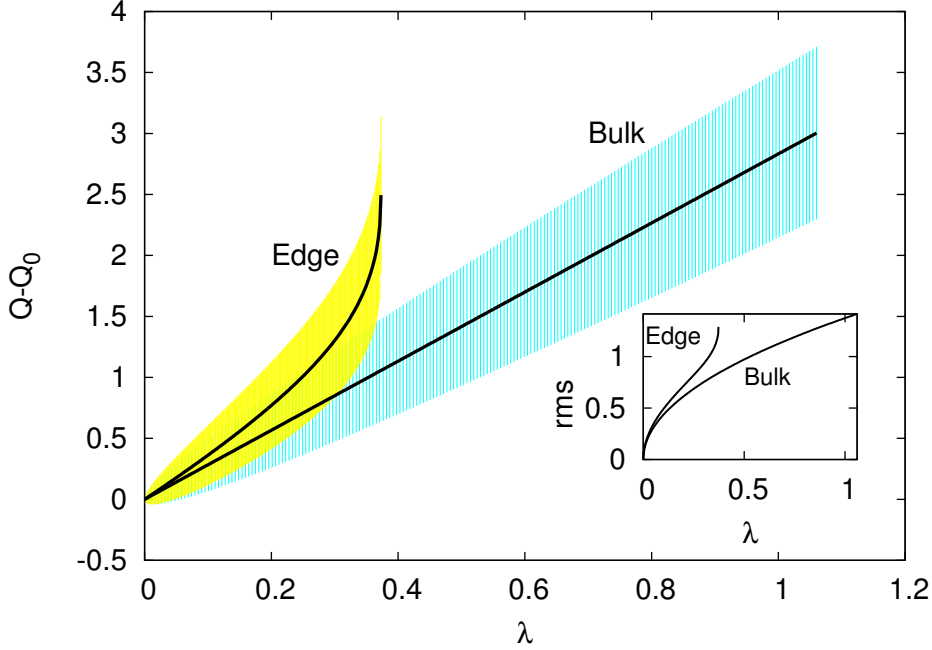


$(\pi/4(1 + \pi/2)^{1/2})^{1/(4\lambda-1)} \rightarrow 0$. However this solution leads to a larger energy (2.17) than even the delocalized solution $\gamma = 0$. The lowest energy (bound) state continues to be described by the largest solution to (2.16).

As λ continues to increase, the finite solutions to (2.16) approach each other and at some λ they coalesce. This is a critical phenomenon corresponding to the limit of stability of the bound edge. At that point the slopes of the right- and left-hand-sides of Eq.(2.16) coincide which leads to the limiting values $\gamma \simeq 0.4920$ and $\lambda \simeq 0.3730$ satisfying the relationship $\gamma = 4\lambda - 1$. At larger values of λ Eq.(2.16) has only one solution $\gamma = 0$ corresponding to an unbound edge. The transition between the bound and unbound states actually happens before the limit of stability is reached, namely when the energy (2.17) vanishes. Numerical analysis shows that it happens at $\lambda \simeq 0.3412$. This is close to the limit of stability thus implying that the edge delocalization is a weak first-order transition.

The results of the analysis are summarized in Fig. 2.1 where we show the bond stiffness γ and the edge binding energy E_{edge} as functions of the quantum parameter λ . The metastability develops in the $1/4 \leq \lambda \leq 0.3730$ range: for $\lambda < 0.3412$ the bound edge has lower energy while for $\lambda > 0.3412$ the ground state corresponds to a delocalized edge particle.

Figure 2.2: (Color online) Quantum expansion $Q-Q_0$ and rms fluctuation of the bulk and edge bonds as functions of the quantum parameter λ (2.6). The rms fluctuation is shown both as the vertical extent of shaded regions centered around the quantum expansion curves, and explicitly in the inset.



These conclusions should be contrasted with the properties of the bulk Luttinger liquid. Its range of existence is given by [53] $0 < \lambda \leq 1.0591$ (or equivalently $0 < \lambda_0 \leq 0.3896$) which is the condition that a solution $\lambda(\lambda_0)$ to Eq.(2.14) can be found for given De Boer's number λ_0 (2.1). Therefore in the $0.3730 < \lambda \leq 1.0591$ range the bulk Luttinger liquid is stable against the disordering effect of quantum fluctuations while the edge is not. This is due to the stronger softening effect that zero-point motion has on the free edge as compared to the bulk of the system. The direct evidence of this is presented in Fig. 2.2 where we show the quantum expansion and rms fluctuation of the bulk and edge bonds as functions of the quantum parameter λ (2.6) within their corresponding ranges of existence. The quantum expansion in the bulk (2.13) is a linear function of λ while the edge bond expands faster than linearly because the bond stiffness γ entering the argument of the logarithm in (2.8) is a decreasing function of λ as shown in Fig. 2.1. Since the $\gamma(\lambda)$ dependence is not very strong one can say that the edge expansion is roughly twice the bulk value as suggested by the ratio of pre-logarithmic factors in Eqs.(2.8) and (2.13). This can be understood by noticing that any bulk bond joins two half-infinite Luttinger liquids thus implying that its dynamics is twice as inertial as that of the edge. In this sense zero-point motion at the edge is about twice as strong as that in

the bulk. The same argument explains why the edge rms fluctuation is roughly square-root of two larger than its bulk counterpart (compare Eqs.(2.5) and (2.12)).

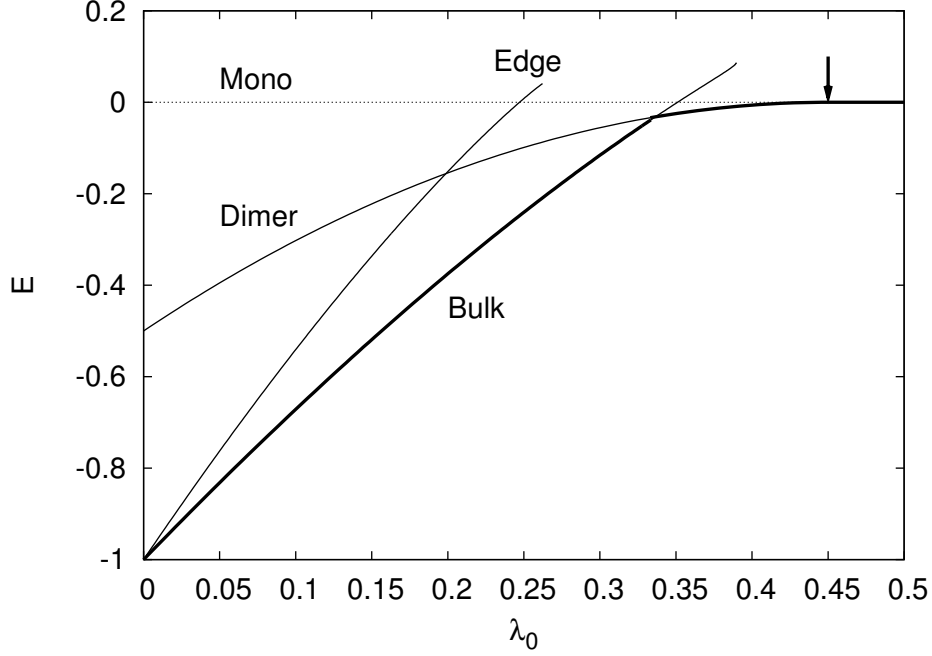
In describing the dynamics of the edge bond the rest of the system was approximated by a harmonic liquid with the bulk properties which means that the bond adjacent to the edge has the length and rms fluctuation identical to those in the bulk. This is an artifact and in reality, as one goes inside the bulk, the bond lengths and their rms fluctuations decrease approaching the bulk values asymptotically. This deficiency would be acceptable provided the calculated length of the edge bond and its rms fluctuation are not very different from their bulk counterparts. Since for molecular matter with pair interaction potential of the Morse form the classical bond length satisfies the condition $Q_0 \gtrsim 5$ [53], inspection of Fig. 2.2 shows that even at the limit of its stability the length of the edge bond and its rms fluctuation do not exceed their bulk counterparts by more than an acceptable 25%.

Moreover, the relative fluctuation $\langle f^2 \rangle_0^{1/2} / Q_{edge}$ is always significantly smaller than unity which implies that our conclusions are weakly sensitive to the statistics of the underlying particles and that the deficiencies of the Morse potential in mimicking the true pair interaction at largest and shortest distances are ignorable. The latter allows us to argue that the edge dissociation pre-empting the bulk instability is a general property of one-dimensional molecular matter.

In order to gain an insight into the consequences of this effect in Fig. 2.3 we plot the ground-state energy per particle of the bulk Luttinger liquid (given by Eqs.(2.14) and (2.15)) and the binding energy of the edge particle (determined through Eqs.(2.14), (2.16), and (2.17) as functions of De Boer's number λ_0 (2.1). Additionally we show the ground-state energy per particle for an infinitely diluted gas of Morse dimers, $E_{dimer}(\lambda_0) = -(1/2)(1 - \pi\lambda_0/\sqrt{2})^2$ [20]. The bold parts of the curves describe the ground states of the bulk matter: as De Boer's number increases, at $\lambda_0 \simeq 0.3365$ the Luttinger liquid evaporates via a discontinuous transition into a gas of dimers followed by a continuous dissociation transition at $\lambda_0 = \sqrt{2}/\pi$ into a monoatomic gas [53]. For a system with a free edge the binding energy of the edge particle E_{edge} can become smaller than its dimer counterpart E_{dimer} : for $\lambda_0 \gtrsim 0.1981$ the whole Luttinger liquid comes unraveled, *two* particles at a time despite the fact that the bulk condensed state is energetically favorable. Since our bulk and edge binding energies are variational upper bounds, in actuality the dimer gas may not come into play; its role then will be played by the monoatomic gas.

If the escape of the edge particles to infinity is impossible due to a distant obstacle, this will

Figure 2.3: The dependences of the energy per particle for various bulk phases of the system on De Boer's number λ_0 (2.1) together with edge binding energy. The arrow pointing down is the dimer dissociation threshold.



generate a vapor pressure and the bulk Luttinger liquid may coexist with a gas of particles. As λ_0 increases toward the point of the bulk transition, dissociation proceeds inside the bulk in a manner similar to that in surface melting [50]. We hasten to mention the speculative character of the statements of this paragraph which we plan to clarify in the future.

Two examples of one-dimensional matter with a dissociated edge and a stable bulk, $0.1981 < \lambda_0 < 0.3365$, include H_2 and D_2 in free space, and more cases can be found in the presence of a medium [53].

Chapter 3

The Zel'dovich effect and evolution of atomic Rydberg spectra along the Periodic Table

3.1 Organization

The organization of this chapter is as follows. In Section 3.2 we provide a short derivation of the Rydberg formula (2) and arrive at the expression for the quantum defect in terms of the dimensionless range of the inner potential and its scattering length. This general result is further analyzed in the $r_0 \ll a_B$ limit and the main features of the Zel'dovich spectral reconstruction are recovered (Section 3.2.1). In Section 3.2.2 we establish a relationship between the Zel'dovich effect and Levinson's theorem of quantum mechanics. This is followed (Section 3.2.3) by the analysis of the opposite $r_0 \gg a_B$ limit where we demonstrate that the Zel'dovich effect manifests itself in the form of a spectral modulation whose origin still lies in the binding properties of the inner potential $U_s(r)$. These general findings are illustrated in Section 3.2.4 where we use the exactly-solvable example of the rectangular well as a model for the inner potential. In Section 3.2.5 we observe that only a treatment more accurate than semiclassical can capture the Zel'dovich effect.

Section 3.3 focuses on the computation of the systematic quantum defect of the Rydberg electron as a function of atomic number Z . First (Section 3.3.1), for the inner potential having an attractive

Coulombic singularity at the origin, we derive a semiclassical expression for the quantum defect and show that it is equal to the number of de Broglie's half-waves fitting inside the inner potential minus a contribution proportional to $(r_0/a_B)^{1/2}$. Going beyond the semiclassical approximation we also demonstrate that the Zel'dovich modulation of the quantum defect is a periodic function of the number of de Broglie's half-waves fitting inside the ionic core of the atom. This is followed by an explicit calculation based on Latter's model of the ionic core [63]. Here, the semiclassical quantum defect is calculated as a function of $Z^{1/3}$ (Section 3.3.2). Then (in Section 3.3.3) a full computation capturing the Zel'dovich effect is performed. An important ingredient here is an approximate calculation of the scattering length of the ionic core of the atom. Both the scattering length and the related Zel'dovich modulation of the quantum defect turned out to be nearly periodic functions of $Z^{1/3}$.

In Section 3.4 the results of our systematic calculation are compared with experimental and numerical data. First, we observe that the bulk of the quantum defect values is well-captured semiclassically. Then (Section 3.4.1) we demonstrate that the gross features of the deviation away from semiclassics are due to the effects of the shell structure. This is done by establishing and demonstrating a correlation between the variation of the radius of the ionic core of the atom and the corresponding variation of the quantum defect. Finally, in Section 3.4.2 a Fourier analysis of the quantum defect variation with $Z^{1/3}$ is conducted which singles out the Zel'dovich effect. As a by-product we also find a $Z^{1/3}$ periodic contribution coming from the shell effects.

We conclude (Section 3.5) by outlining our main result and directions of future work.

3.2 Distorted Coulomb problem and quantum defect

We will be interested in low energy bound states with the classical turning point being far away from the boundary of the central region, i. e. $\hbar^2/ma_B|E| \gg r_0$. Then the quickest way to derive the spectrum is via semiclassical arguments derived from those given by Migdal [67]:

For $r_0 < r < \hbar^2/ma_B|E|$ the semiclassical solution to Eq.(1) can be written in two equivalent

forms:

$$\begin{aligned}\chi_{sc} &\propto \frac{1}{\sqrt{p}} \sin \left(\frac{1}{\hbar} \int_r^{\hbar^2/ma_B|E|} p dr + \frac{\pi}{4} \right) \\ &\propto \frac{1}{\sqrt{p}} \sin \left(\frac{1}{\hbar} \int_{r_0}^r p dr + \alpha \right)\end{aligned}\quad (3.1)$$

where $p = (-2m|E| + 2\hbar^2/ra_B)^{1/2}$ is the momentum. The first representation in Eq.(3.1) is the standard result with the phase of $\pi/4$ improving on the deficiency of the semiclassical approximation near the classical turning point, while the yet undetermined phase α in the second representation in Eq.(3.1) both corrects for the failure of the semiclassical approximation in a Coulomb field at distances $r \lesssim a_B$ and accounts for the short-range potential $U_s(r)$.

For $r_0 < r \ll \hbar^2/ma_B|E|$ the Schrödinger equation (1) simplifies to

$$\frac{d^2\chi}{dr^2} + \frac{2}{ra_B}\chi = 0 \quad (3.2)$$

and can be exactly solved:

$$\chi \propto r^{1/2} \left(J_1(\sqrt{8r/a_B}) - Y_1(\sqrt{8r/a_B}) \tan \delta \right) \quad (3.3)$$

where $J_\nu(x)$ and $Y_\nu(x)$ are the order ν Bessel functions of the first and second kind respectively [68]. The solution (3.3) is a linear combination of the regular $J_1(0) = 0$ and irregular $Y_1(0) = \infty$ Coulomb functions of zero energy, and for the purely Coulomb problem, $U_s(r) = -\hbar^2/ma_B r$, one has to recover $\tan \delta = 0$.

For $a_B \ll r \ll \hbar^2/ma_B|E|$ the semiclassical approximation is accurate, and the second representation of Eq.(3.1) yields $\chi \propto r^{1/4} \sin(\sqrt{8r/a_B} - \sqrt{8r_0/a_B} + \alpha)$. On the other hand, the $r \gg a_B$ limit of (3.3) is $\chi \propto r^{1/4} \sin(\sqrt{8r/a_B} - \pi/4 + \delta)$ which determines α in (3.1) to be $\sqrt{8r_0/a_B} - \pi/4 + \delta$. It also implies that δ in (3.3) is the zero-energy phase shift due to the small-distance deviation of the potential from the Coulomb form.

The energy spectrum can be found from the requirement that the semiclassical expressions (3.1)

coincide. Combined with $\alpha = \sqrt{8r_0/a_B} - \pi/4 + \delta$ this gives the quantization rule

$$\frac{1}{\hbar} \int_{r_0}^{\hbar^2/ma_B|E|} p dr = \pi n - \delta - x_0 \quad (3.4)$$

where the dimensionless parameter

$$x_0 = \sqrt{\frac{8r_0}{a_B}} \quad (3.5)$$

measures the range of the short-range forces. Calculating the integral we arrive at Eq.(2) with $\delta = \pi\mu$ which is the statement of Seaton's theorem [62] relating the quantum defect to the zero-energy phase shift.

The range of applicability of Eq.(2), $n - \mu \gg (r_0/a_B)^{1/2} \simeq x_0$, follows from the condition $|E| \ll \hbar^2/ma_B r_0$ which also implies that in order to calculate the quantum defect entering the spectrum (2), we only need to match (3.3) with its zero energy counterpart at $r < r_0$.

We proceed by computing $h = [d \ln \chi / d \ln r]_{r \rightarrow r_0+0}$, the logarithmic derivative of the function (3.3) evaluated at the boundary of the inner region:

$$h = \frac{x_0}{2} \frac{J_0(x_0) - Y_0(x_0) \tan \pi\mu}{J_1(x_0) - Y_1(x_0) \tan \pi\mu} \quad (3.6)$$

where we used $\delta = \pi\mu$. The quantum defect μ is determined by setting eq. (3.6) equal to $h_s = [d \ln \chi / d \ln r]_{r \rightarrow r_0-0}$ which can be found by solving the $E = 0$ Schrödinger equation (1) for $r < r_0$ with $U(r) = U_s(r)$:

$$\frac{d^2 \chi}{dr^2} - \frac{2m}{\hbar^2} U_s(r) \chi = 0 \quad (3.7)$$

The parameter h_s can be equivalently expressed in terms of the scattering length corresponding to the inner potential *only*. Indeed for motion in a short-range potential the scattering length a_s is defined from the asymptotic $r \rightarrow \infty$ behavior $\chi(r) \propto 1 - r/a_s$ of the solution to (3.7). For a potential well identically vanishing for $r > r_0$, this is also the exact behavior outside the well with the implication that [56, 60]

$$h_s^{-1} = \left(\frac{d \ln \chi(r \rightarrow r_0 - 0)}{d \ln r} \right)^{-1} = 1 - \frac{a_s}{r_0} \quad (3.8)$$

Then substituting $h = h_s$ in Eq.(3.6) and using (3.8) we arrive at the formula for the quantum defect

$$\tan \pi\mu = \frac{2x_0^{-1}J_1(x_0) + (a_s/r_0 - 1)J_0(x_0)}{2x_0^{-1}Y_1(x_0) + (a_s/r_0 - 1)Y_0(x_0)} \quad (3.9)$$

If the short-distance potential is selected in the form $U_s(r) = -\hbar^2/ma_B r$, i. e. we have the ordinary Coulomb problem in the whole space, the quantum defect μ entering the Rydberg formula (2) must vanish identically. It is straightforward to verify that this is indeed the case: the $E = 0$ inner $r < r_0$ solution to (1), $\chi \propto r^{1/2}J_1(\sqrt{8r/a_B})$, leads to the expression for the scattering length nullifying the numerator of (3.9). This argument defines the zero of the quantum defect and implies that μ is necessarily positive if for all $r \leq r_0$ the inner potential $U_s(r)$ is more attractive than the Coulomb potential $-\hbar^2/ma_B r$; otherwise the quantum defect is negative. For example, for $U_s(r) = 0$ the quantum defect $\mu(0, x_0)$ is a negative monotonically decreasing function of x_0 such as $\mu = -x_0^4/32$ for $x_0 \ll 1$, and $\mu = 3/4 - x_0/\pi$ in the opposite $x_0 \gg 1$ limit. The $\mu(0, x_0)$ dependence as well as its $x_0 \gg 1$ limit are shown in Fig. 3.1.

3.2.1 Zel'dovich effect in the $r_0 \ll a_B$ limit

For $x_0 \ll 1$ Eq.(3.9) simplifies to a form accumulating the physics of the Zel'dovich effect:

$$\frac{a_B}{2\pi a_s} \equiv \frac{4}{\pi x_0^2(1 - h_s^{-1})} = -\cot \pi\mu - \frac{2}{\pi} \ln \frac{2}{\gamma x_0} \quad (3.10)$$

where $\ln \gamma = 0.5772$ is Euler's constant. Terms of higher order in x_0 which for $U_s(r) = 0$ lead to small negative values of the quantum defect are neglected in (3.10).

We verified that Eq.(3.10) matches the upper portion of the ns spectrum which for $r_0 \ll a_B$ is known in closed form for any n [60]. We also note that with some effort Eq.(3.10) can be deduced from the expression for the phase shift of the proton-proton scattering given by Landau and Smorodinskii [69]: in their formula we have to (i) reverse the sign of the Bohr radius, (ii) take the limit of zero energy, and (iii) employ Seaton's theorem [62] $\delta = \pi\mu$.

Fig. 3.2 shows the dependence of $a_B/2\pi a_s$ on μ given by Eq.(3.10); its inverse $\mu(a_B/2\pi a_s)$ is a multivalued function consisting of a series of increasing step-like curves sandwiched between nearest non-negative integers. The slope of $\mu(a_B/2\pi a_s)$ is small everywhere except for the vicinity of half-integer μ .

Figure 3.1: Quantum defect for $U_s(r) = 0$ as a function of the range parameter x_0 , Eq.(3.5), and its $x_0 \gg 1$ limit, $\mu(0, x_0) = 3/4 - x_0/\pi$ (shown in gray scale).

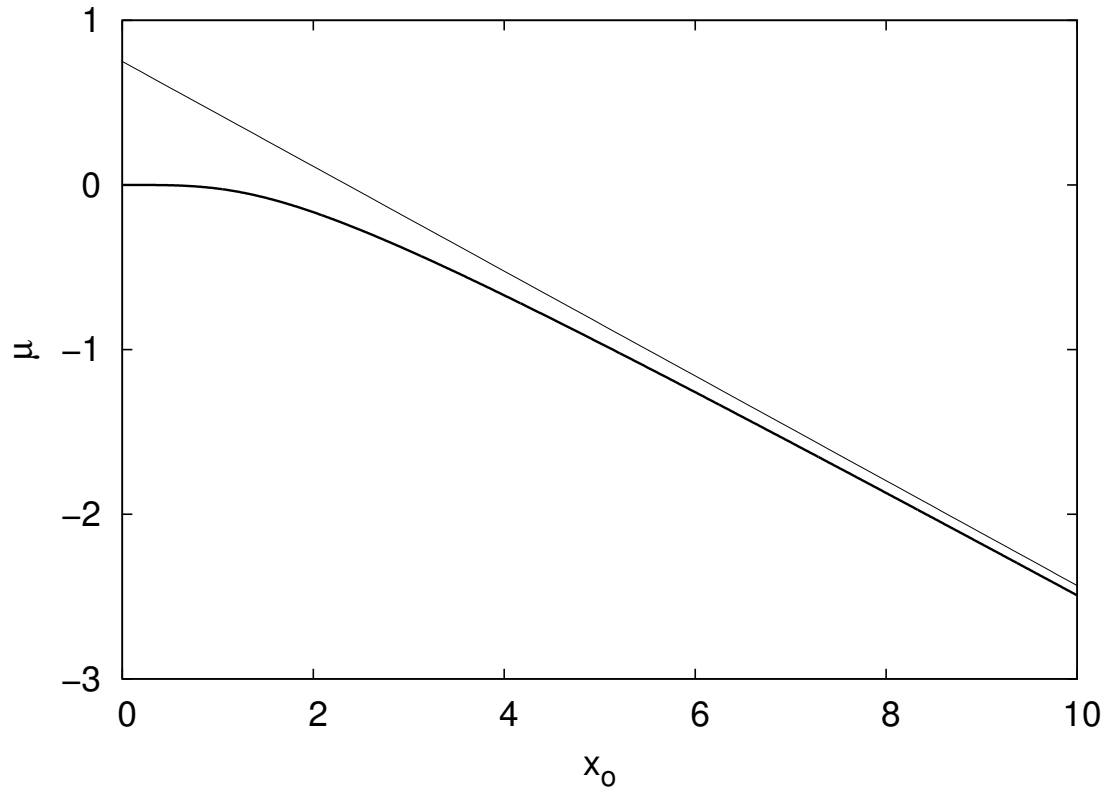
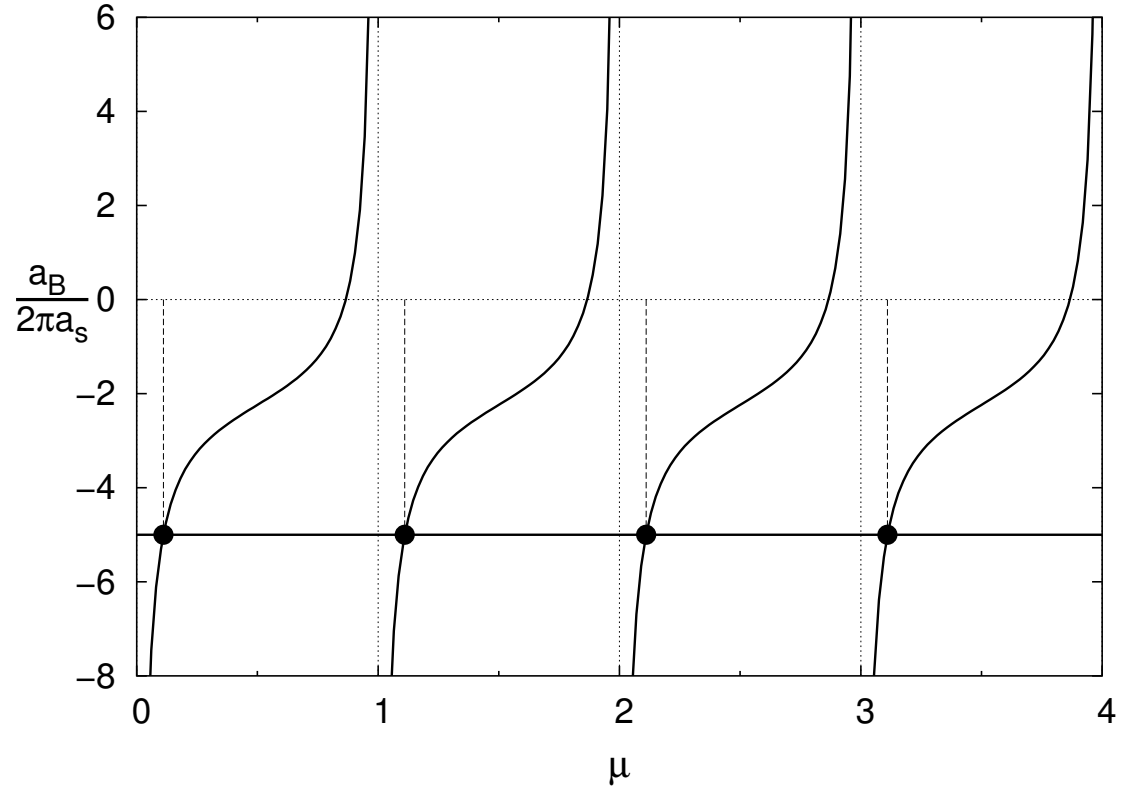


Figure 3.2: Graphical solution of Eq.(3.10); $x_0 = 1/30$ has been used to construct the graph. The quantum defect μ is given by the intersections of the right-hand side of (3.10) with the line of constant $a_B/2\pi a_s$.



Since typically the central potential $U_s(r)$ is not resonant, $|h_s|$ in (3.10) is not small. Then the magnitude of the scattering length is of the order of the size of the inner well, $|a_s| \simeq r_0$ and $a_B/2\pi|a_s| \simeq 1/x_0^2$ is significantly larger than the last term in (3.10). This implies that the quantum defect is very close to an integer, $\mu = -2a_s/a_B \pmod{1}$, with $|a_s|/a_B \simeq r_0/a_B \ll 1$. This conclusion is in quantitative agreement with the results of perturbation theory in a_s/a_B when the deviation from the Bohr Hydrogen formula is small [70, 56]. It is applicable to an attractive non-resonant well of arbitrary strength; for weak $U_s(r)$ which cannot support a bound state we have $\mu = -2a_s/a_B > 0$ [71] represented by the leftmost intersection in Fig. 3.2. We also note that the spectrum is exactly Hydrogenic if the scattering length is zero which can be viewed as an analog of the Ramsauer effect [72]: in the present context it refers to a resonant phenomenon when the distortion of the Coulomb potential at small distances is invisible to the low-energy bound (or incident) particle.

Exactly at half-integer μ the scattering length is negative with the magnitude given by $|a_s| = (a_B/4) \ln^{-1}(2/\gamma x_0) = 2r_0 x_0^{-2} \ln^{-1}(2/\gamma x_0)$ significantly exceeding the size of the central region r_0 . This implies that the slope of the $\mu(a_B/2\pi a_s)$ dependence is largest when $U_s(r)$ itself is almost resonant so that it supports a low-energy *virtual* state. At the point of steepest slope we also have $[d\chi/dr]_{r=r_0} \propto h_s \simeq (x_0^2/2) \ln(2/\gamma x_0) \ll 1$. Since this is practically zero, one can equivalently say that the slope of the $\mu(a_B/2\pi a_s)$ dependence is largest when the antinode of the function χ in Eq.(1) occurs at the boundary of the inner region r_0 . This criterion resembles that given by Fano, Theodosiou and Dehmer [65] for the dependence of the quantum defect μ on atomic number Z . We note however, that for a Rydberg atom the size of the residual ion does not satisfy the condition $r_0 \ll a_B$; this issue is further addressed below.

If for all r the central well is attractive, its effect can be quantified by a single dimensionless coupling constant $w \simeq mr_0^2|U_s|/\hbar^2 > 0$ where $|U_s|$ has a meaning of the characteristic depth of the well. Then the inverse scattering length a_s^{-1} is known to be a monotonically increasing function of w [60] - an a_s dependence shown in Fig. 3.3 in gray scale is typical and may help illustrate the argument given below.

The step-like features of the function $\mu(a_B/2\pi a_s)$ are amplified in the $\mu(w)$ dependence. Indeed, for $w \ll 1$ the scattering length a_s is very small and negative. Then the line of constant $a_B/2\pi a_s$ in Fig. 3.2 lies at very large negative values, the quantum defect satisfies $\mu = -2a_s/a_B \ll 1$, and the deviation from the normal Hydrogen spectrum is small. As the well deepens, the coupling constant w increases, the scattering length becomes more negative and the horizontal line of constant $a_B/2\pi a_s$

moves upward. However as long as the well remains non-resonant, the quantum defect μ will only grow very little. The strongest increase of $\mu(w)$ in response to deepening of the well (and thus the largest deviation from the Bohr Hydrogen formula) occurs when the scattering length reaches a very large negative value $a_s = -2r_0x_0^{-2} \ln^{-1}(2/\gamma x_0)$. For $x_0 \ll 1$ this takes place very close to a threshold value of the coupling constant w when the first bound state is about to appear in $U_s(r)$. The relative width of the reconstruction region $\Delta w/w$ centered around $\mu = 1/2$ thus can be estimated from the scaling behavior of the scattering length near the threshold $a_s \simeq r_0 w / \Delta w$ and the condition $a_B \simeq |a_s|$. This leads to the original result of Zel'dovich [56] $\Delta w/w \simeq r_0/a_B$.

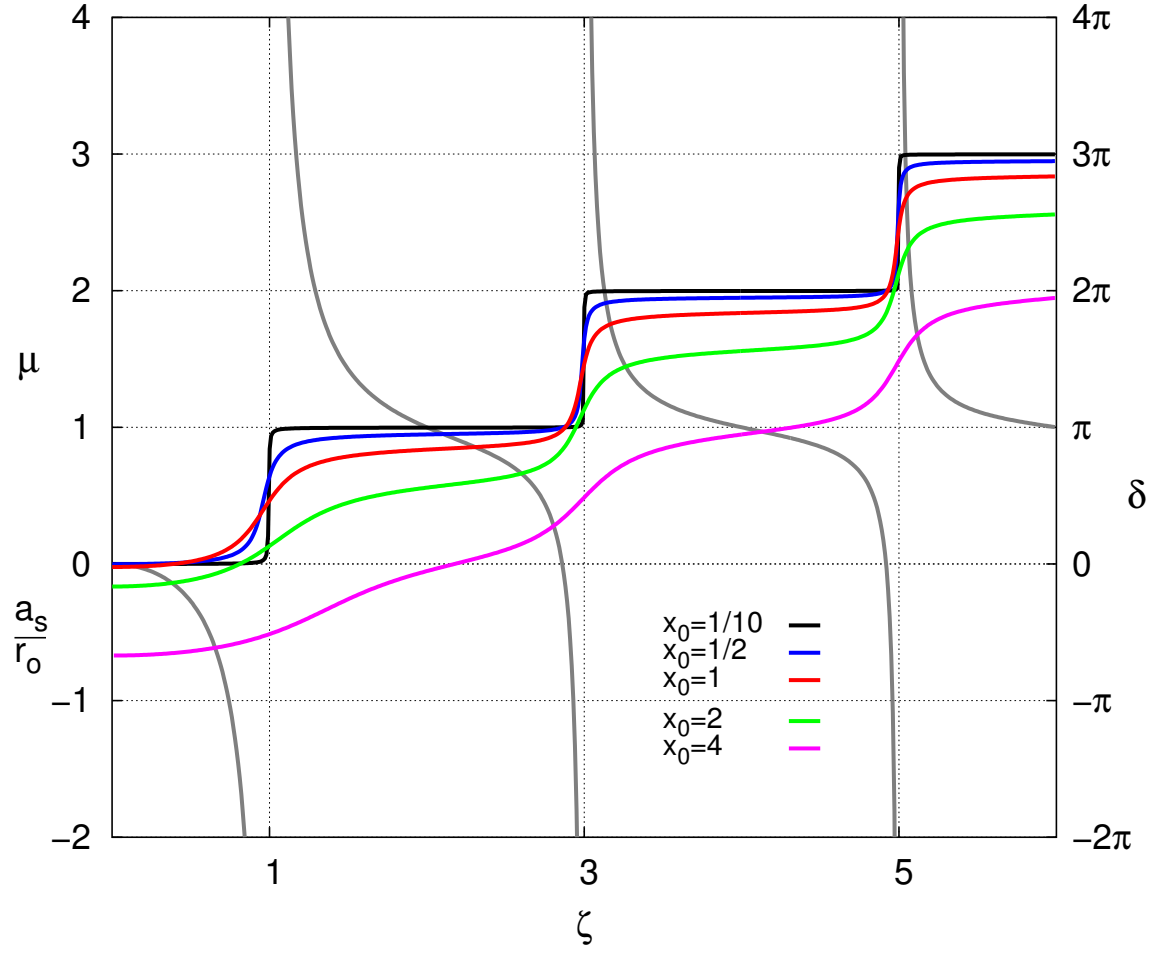
As the coupling constant w increases through the first binding threshold, the inverse scattering length changes sign, and the line of constant $a_B/2\pi a_s$ in Fig. 3.2 enters the region of positive values. After passing through the reconstruction region, the positive scattering length decreases in magnitude, for $a_s/a_B \ll 1$ the quantum defect is close to unity, $\mu = 1 - 2a_s/a_B$, and the deviation from the normal Hydrogen spectrum is again small. In the region $a_s \simeq r_0$ the scattering length does not vary strongly with the depth of the well, and one can say that the slope of the $\mu(w)$ dependence will be minimal when the node of the function χ in Eq.(1) is near the boundary of the central region r_0 which parallels the criterion of Fano, Theodosiou and Dehmer [65]. Upon further increase of the coupling constant w , the scattering length gets smaller and the line of constant $a_B/2\pi a_s$ in Fig. 3.1 enters the region of very large positive values becoming infinite at $a_s = 0$.

The correlation with the binding properties of the well is seen from the plot of the reduced scattering length a_s/r_0 (gray scale). Shown are also the values of the zero-energy phase shift $\delta = \pi\mu$ relating the Zel'dovich effect to Levinson's theorem.

To summarize, as $a_s(w)$ goes through one complete cycle decreasing from zero, passing through the binding resonance, and then approaching zero from above, the quantum defect $\mu(w)$ increases from zero to unity in a staircase fashion: it is mostly zero or unity except for the narrow region $\Delta w/w \simeq r_0/a_B \ll 1$, $\mu \simeq 1/2$ near the first binding threshold of $U_s(r)$. Combined with the Rydberg formula (2) this implies that the Coulomb levels E_n quickly fall to E_{n-1} which constitutes the essence of the Zel'dovich effect [56].

As the coupling constant w continues to increase away from $a_s(w) = 0$, the next cycle, $1 < \mu(w) < 2$, begins and qualitatively the same pattern repeats itself. This remains true for every subsequent cycle with $\mu(w)$ sandwiched between nearest integers. Overall the quantum defect is an increasing function of w having the form of a staircase with practically integer plateaus and sharp

Figure 3.3: Evolution of the Zel'dovich effect for the rectangular well of radius r_0 and depth U_0 for a series of range parameters x_0 , Eq.(3.5), manifested in the dependences of the quantum defect μ on $\zeta = (8mU_0r_0^2/\pi^2\hbar^2)^{1/2} \simeq w^{1/2}$.



steps located at half-integer μ . The steps correspond to the presence of the low-energy scattering resonances in $U_s(r)$.

To illustrate this behavior we choose the inner potential in the form of a rectangular well of depth U_0 whose scattering length is given by $a_s/r_0 = 1 - 2 \tan(\pi\zeta/2)/\pi\zeta$ with dimensionless parameter $\zeta = (8mU_0r_0^2/\pi^2\hbar^2)^{1/2} \simeq w^{1/2}$ quantifying the depth of the well. The scattering length diverges at odd values of ζ which correspond to consecutive occurrences of bound states in the well; the respective dependence of a_s/r_0 on ζ is shown in Fig. 3.3 in gray scale. We also plot the dependences of the quantum defect μ on ζ found from the general expression (3.9) for a series of representative x_0 . The analysis based on Eq.(3.10) is illustrated by the $x_0 = 1/10$ and $x_0 = 1/2$ curves; the latter corresponds to the case of the proton-antiproton atom [60]. These dependences have the form of staircases with nearly integer plateaus; the steepness of the steps where the quantum defect varies by unity and the flatness of the plateaus increase as x_0 gets smaller. An inspection reveals that the points of maximal slope of $\mu(\zeta)$ somewhat precede the scattering resonances in accordance with the analysis given above. This is seen most clearly for the $\zeta \simeq 1$ step of the $x_0 = 1/2$ curve. Fig. 3.2 of Zel'dovich's work [56] has this feature as well. From a practical standpoint the steps can be considered to coincide with the binding resonances of the well.

The relative width of the reconstruction region $\Delta\zeta/\zeta$ can be estimated as $r_0/a_B\zeta^2$. Since the threshold values ζ grow linearly with the number of bound states, then for fixed x_0 the steepness of the steps increases with ζ as can be seen in Fig. 3.3. This is merely the consequence of the sharpening of the binding resonances. Similarly the flatness of the plateaus improves as ζ increases, and the points of least slope of the $\mu(\zeta)$ dependence asymptotically approach even values of ζ . This is where the node of the function χ in Eq.(1) coincides with the boundary of the central region, $a_s = r_0$.

Finally we note that the quantum defect takes on exactly integer values whenever the scattering length vanishes.

3.2.2 Connection to Levinson's theorem

There is a deep parallel between the Zel'dovich reconstruction of the upper $E \rightarrow 0$ part of the Coulomb spectrum in the $r_0 \ll a_B$ limit and the low-energy scattering by a short-range potential well. For a particle of energy $E = \hbar^2 k^2/2m$ whose wave vector \mathbf{k} is small in magnitude, $kr_0 \ll 1$, scattered by the short-range potential $U_s(r)$ vanishing for $r > r_0$ the scattering length a_s can be

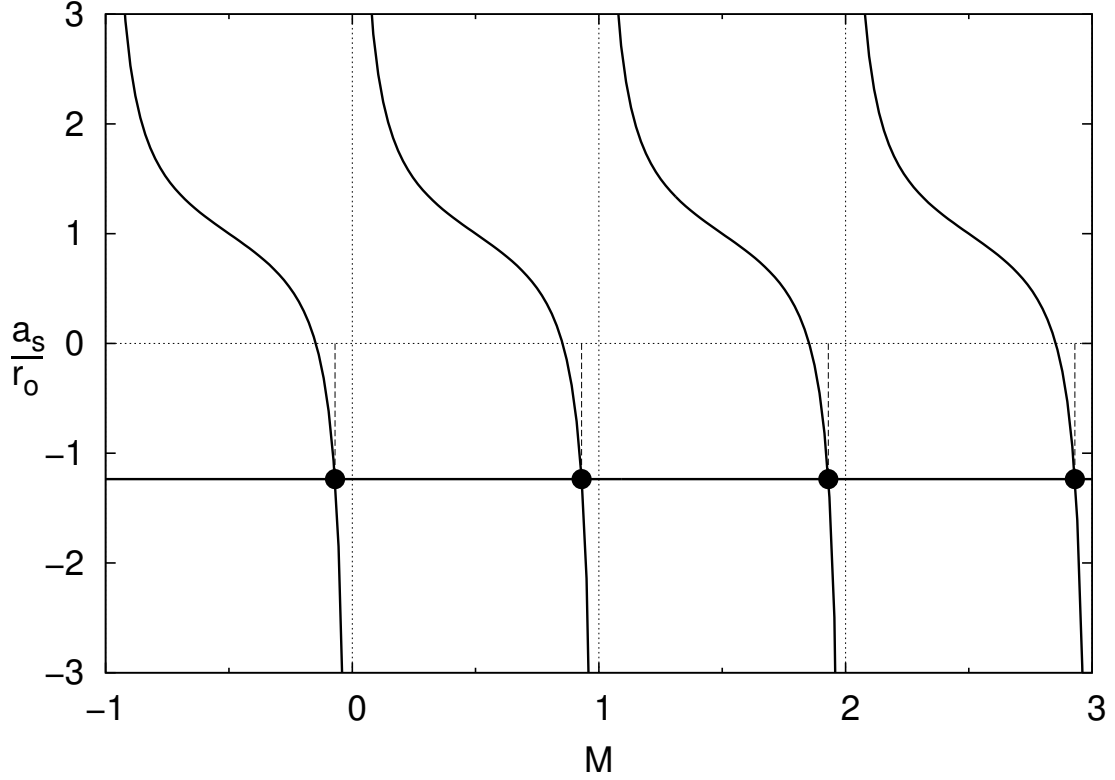
defined [73] through the $k \rightarrow 0$ limit of the relationship

$$1/ka_s = -\cot \delta_s(k) \quad (3.11)$$

where $\delta_s(k)$ is the phase shift. Employing Seaton's theorem [62] $\delta = \pi\mu$ relating the quantum defect to the zero-energy phase shift it is straightforward to realize that Eqs.(3.10) and (3.11) are direct analogs. The Coulomb field is characterized by its own length scale, the Bohr radius a_B . Its free particle counterpart entering Eq.(3.11) is the de Broglie wavelength $2\pi/k$. The range of applicability of Eq.(3.10) $r_0 \ll a_B$ parallels the low-energy condition $kr_0 \ll 1$ necessary for Eq.(3.11) to hold. The analysis which led to the explanation of the Zel'dovich effect can be repeated for Eq.(3.11) with the conclusion that the phase shift $\delta_s(k)$ as a function of the dimensionless depth w of the scattering well has the form of a sharp increasing staircase whose plateaus practically coincide with $\delta_s(k) = 0 \pmod{\pi}$. The steps where the phase shift changes by π are very narrow, $\Delta w/w \simeq kr_0 \ll 1$, and the points of steepest slope are located at $\delta_s(k) \simeq \pi/2 \pmod{\pi}$. In the limit $k \rightarrow 0$ the staircase becomes perfect. This can be recognized as Levinson's theorem [73] relating the number of bound states in a well with the zero-energy scattering phase shift. We conclude that for $r_0 \ll a_B$ the Zel'dovich effect expressed in terms of the zero-energy phase shift δ is the Coulombic cousin of Levinson's theorem [74]. A special case of this correspondence, the Ramsauer-like recovery of the normal Hydrogen spectrum for $a_s = 0$, was already mentioned earlier. In the limit $x_0 = \sqrt{8r_0/a_B} \rightarrow 0$ Zel'dovich's staircase becomes perfect and identical to Levinson's staircase. This can be understood as a result of taking the neutral limit, $a_B \rightarrow \infty$, when the Coulomb part of the binding potential $U(r)$ in (1) vanishes. From this viewpoint, Levinson's theorem is a consequence of the Zel'dovich effect. To emphasize the connection to Levinson's theorem, in Fig. 3.3 we additionally show the zero-energy phase shift $\delta = \pi\mu$.

Fig. 3.3 also demonstrates that as x_0 increases, the staircase $\mu(\zeta)$ dependence with well-defined steps and plateaus evolves into an increasing function with modulations: the "plateaus" develop noticeable slope and the "steps" acquire a width. Moreover for sufficiently large $x_0 \gtrsim 1$ the staircase-like appearance seems to emerge only for a sufficiently deep well, i. e. large ζ . Another feature is the presence of a negative offset which is a growing function of x_0 . This is due to the fact that for $U_s(r) = 0$ the quantum defect is a monotonically decreasing negative function of x_0 as shown in Fig. 3.1.

Figure 3.4: Graphical solution of Eq.(3.12); $x_0 = 4$ has been used to construct the graph. The reduced quantum defect $M = \mu + x_0/\pi - 3/4$ is given by the intersections of the right-hand side of (3.12) with the line of constant a_s/r_0 .



3.2.3 Zel'dovich effect in the $r_0 \gg a_B$ limit

In the $x_0 \gg 1$ limit Eq.(3.9) simplifies to the form

$$\frac{a_s}{r_0} = \frac{2}{x_0} \cot(\pi\mu + x_0 - \frac{3\pi}{4}) + 1 \quad (3.12)$$

allowing model-independent treatment. The analysis of Eq.(3.12) is convenient to conduct in terms of the reduced quantum defect $M = \mu + x_0/\pi - 3/4$ whose zero gives the $x_0 \gg 1$ asymptotic of μ for $U_s(r) = 0$. Eq.(3.12) can be investigated in a manner analogous to that of Eq.(3.10); a brief summary is given below.

Fig. 3.4 shows the dependence of a_s/r_0 on $M = \mu + x_0/\pi - 3/4$ given by Eq.(3.12); its inverse $M(a_s/r_0)$ is a multivalued function consisting of a series of decreasing step-like segments sandwiched between nearest integers.

The magnitude of the slope of $M(a_s/r_0)$ is smallest at integer M which occurs at binding resonances, $a_s = \pm\infty$, i. e. when the antinode of the function χ in Eq.(1) coincides with the boundary of the inner region r_0 . In the vicinity of integer M we find $M = 2r_0/\pi x_0 a_s \pmod{1}$. This translates into an explicit result for the quantum defect $\mu = 3/4 - x_0/\pi + 2r_0/\pi x_0 a_s \pmod{1}$ valid in the limit $x_0 \gg 1$ and $r_0/x_0 a_s \ll 1$, thus roughly covering the range of $|a_s|$ from r_0 to infinity. In the vicinity of the first binding resonance we have $\mu = 3/4 - x_0/\pi + 2r_0/\pi x_0 a_s$ which is represented by the leftmost intersection in Fig. 3.4.

The magnitude of the slope of the $M(a_s/r_0)$ dependence is largest at half-integer M which occurs at $a_s = r_0$, i. e. when the node of the function χ in Eq.(1) coincides with the boundary of the inner region r_0 . Since the reduced quantum defect M is a decreasing function of a_s/r_0 , and the scattering length a_s is a decreasing function of the well depth w [60], then for fixed x_0 the parameter M (and thus the original quantum defect μ) is an increasing function of w .

In contrast to the $x_0 \ll 1$ regime, here the step-plateau features of the function $M(a_s/r_0)$ are generally suppressed in the $M(w)$ dependence. This is because the dependence of the scattering length a_s on the depth of the well w is weakest in the region $a_s \simeq r_0$ where the $M(a_s/r_0)$ dependence shows a “step”. By the same token the “plateaus” acquire a noticeable slope since the $a_s(w)$ dependence is strongest near the binding resonance, $a_s = \pm\infty$, i. e. where the $M(a_s/r_0)$ dependence is weakest. As a result the dependence of the quantum defect μ on the depth of the well w is more appropriately viewed as consisting of modulations superimposed on an increasing curve. These modulations still have their origin in the binding properties of the inner potential $U_s(r)$.

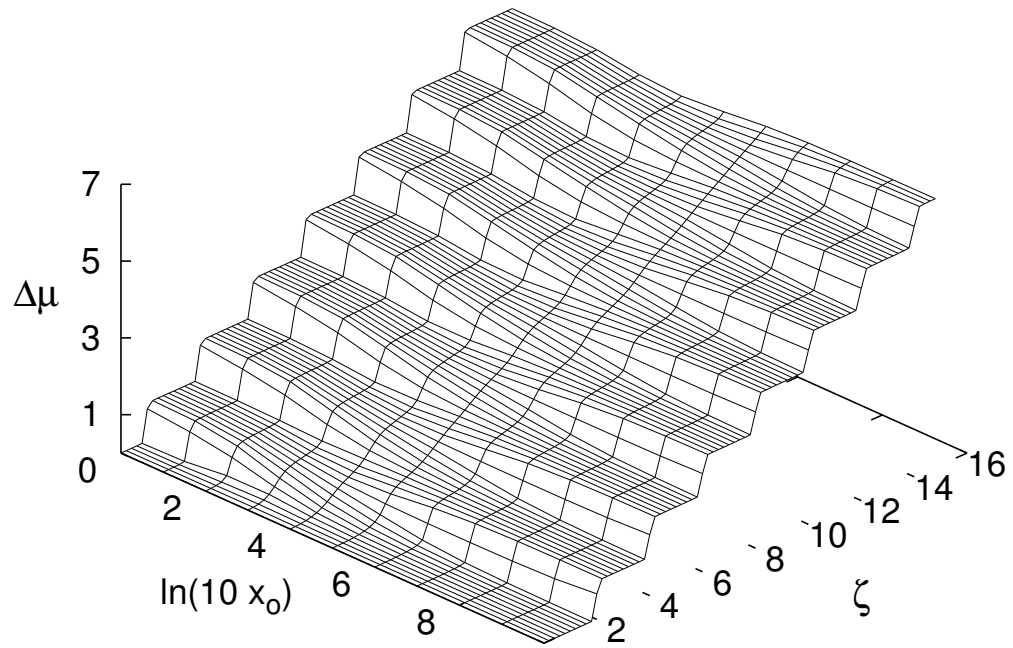
3.2.4 Rectangular well example

The analysis of Sections 3.2.1 and 3.2.3 is illustrated in Fig. 3.5 where using the example of the rectangular well and Eq.(3.9) we plot the surface of the relative quantum defect $\Delta\mu(\zeta, x_0) = \mu(\zeta, x_0) - \mu(0, x_0)$. The point of subtracting $\mu(0, x_0)$ from $\mu(\zeta, x_0)$ is to isolate the physics of binding from the background $\mu(0, x_0)$ which is a monotonically decreasing function of x_0 shown in Fig. 3.1. The peculiar shape of the resulting surface can then be understood as follows:

For $x_0 \ll 1$ the background contribution $\mu(0, x_0)$ is negligible (see Fig. 3.1), the relative quantum defect $\Delta\mu(\zeta, x_0)$ reduces to $\mu(\zeta, x_0)$ which, according to our earlier analysis, is a staircase function of ζ with steps located at odd ζ , i. e. when the bound states occur in the well.

For $x_0 \gg 1$ the background contribution $\mu(0, x_0)$ is $3/4 - x_0/\pi$, and we find that $\Delta\mu(\zeta, x_0) =$

Figure 3.5: Plot of the surface of the relative quantum defect $\Delta\mu(\zeta, x_0) = \mu(\zeta, x_0) - \mu(0, x_0)$ for a rectangular potential well with dimensionless range and depth parameters x_0 and ζ , respectively, according to Eq.(3.9).



$\mu(\zeta, x_0) - \mu(0, x_0) = \mu(\zeta, x_0) + x_0/\pi - 3/4 = M$ which, according to Fig. 3.2, is a decreasing staircase function of a_s/r_0 . For not very deep well the dependence on ζ has a form of a rounded staircase with “steps” and “plateaus” centered at even ($a_s = r_0$) and odd ($a_s = \pm\infty$) values of ζ , respectively. In this regime the underlying step-plateau character of the $M(a_s/r_0)$ function is preserved in the $M(\zeta)$ dependence due to the appreciable slope of the $a_s(\zeta)$ dependence at $a_s = r_0$ and relatively weak divergence at $a_s = \pm\infty$. To recapitulate, both for $x_0 \ll 1$ and $x_0 \gg 1$ and not very deep well the relative quantum defect $\Delta\mu(\zeta, x_0)$ is an increasing staircase function of the depth parameter ζ with the steps located at odd ($x_0 \ll 1$) or even ($x_0 \gg 1$) values of ζ . The crossover between the two regimes can be seen in Fig. 3.5 as a relatively narrow stripe of very weak modulations.

A qualitatively different staircase-like dependence emerges for $x_0 \gg 1$ and sufficiently deep well because as $\zeta \rightarrow \infty$ the slope of the $a_s(\zeta)$ function at $a_s = r_0$ tends to zero while the binding resonances, $a_s = \pm\infty$, become progressively more singular. As a result the “steps” and “plateaus” switch places - the former becomes centered at odd while the latter at even values of ζ . This is somewhat similar to what happens in the $x_0 \ll 1$ limit. This observation explains why the small modulation crossover stripe in Fig. 3.5 runs at an angle to the $(\Delta\mu, \zeta)$ plane. The important qualitative difference between the $x_0 \ll 1$ and $x_0, \zeta \gg 1$ staircases is that the latter have “plateaus” centered at half-integer values of M , thus corresponding to the coincidence of a node of the function χ in Eq.(1) with the boundary of the inner region $r = r_0$.

3.2.5 Semiclassical treatment

For most realistic models of the inner potential $U_s(r)$ the exact analytical calculation of the scattering length a_s entering the general expression for the quantum defect Eq.(3.9) may not be possible. Therefore it is pertinent to understand whether there is an approximate analytical treatment capturing the Zel’dovich spectrum reconstruction. This is especially relevant to the $x_0 \gg 1$ regime when the phenomenon manifests itself only as a modulation of the quantum defect superimposed on a monotonic curve.

For $x_0 \gg 1$ and sufficiently smooth $U_s(r)$ the standard semiclassical approximation is applicable, and the corresponding solution to Eq.(3.7) can be written as

$$\chi_{sc}(r) \sim (S'(r))^{-1/2} \sin \frac{S(r)}{\hbar}, \quad (3.13)$$

where

$$S(r) = \int_0^r (-2mU_s(r))^{1/2} dr \quad (3.14)$$

is the classical action acquired by a zero-energy particle moving radially out from zero to r , and the prime in Eq.(3.13) denotes differentiation with respect to r . The semiclassical expression for the scattering length which can be deduced from Eq. (3.13) with the help of Eq. (3.8) has been given by Berry [75]

$$\frac{a_s}{r_0} = 1 - \left(-\frac{\hbar^2}{2mr_0^2 U_s(r_0)} \right)^{1/2} \tan \frac{S_0}{\hbar} \quad (3.15)$$

where $S_0 \equiv S(r_0)$. Eqs.(3.13) and (3.15), generalizing the “rectangular well” expressions for the wave function and the scattering length, are applicable when the number of de Broglie’s half-waves $S_0/\pi\hbar$ fitting inside $U_s(r)$ is very large. If we additionally assume the continuity of the central potential $U(r)$ in Eq.(1) at the boundary of the inner region,

$$U_s(r_0) = -\hbar^2/mar_0, \quad (3.16)$$

then Eq.(3.15) simplifies to $a_s/r_0 = 1 - (2/x_0) \tan(S_0/\hbar)$. Combining this with Eq.(3.12) we find an explicit semiclassical expression for the quantum defect

$$\mu_{sc} = \frac{3}{4} - \frac{x_0}{\pi} + \frac{S_0}{\pi\hbar} - \frac{1}{2} \quad (3.17)$$

which can be interpreted as approximately the sum of $3/4 - x_0/\pi$, the quantum defect for $U_s(r) = 0$, and the number of de Broglie’s half-waves $S_0/\pi\hbar$ fitting inside the inner part of the potential; the estimate $\mu_{sc} \simeq S_0/\pi\hbar$ has been given earlier [62]. The number of de Broglie’s half-waves can be estimated in terms of the dimensionless depth of the inner well $w \simeq mr_0^2|U_s|/\hbar^2$ as $S_0/\pi\hbar \simeq w^{1/2}$ which implies that for fixed x_0 the quantum defect (3.17) is a monotonically increasing function of w without any modulations. We conclude that the Zel’dovich modulations of the quantum defect are lost in the semiclassical approximation despite the fact that the corresponding scattering length (3.15) does exhibit binding resonances. Thus for $x_0 \gg 1$ a treatment better than semiclassical is required to capture the deviations from monotonic behavior; a similar conclusion has been reached earlier [65].

For the rectangular well of radius r_0 and depth U_0 characterized by the coupling constant $\zeta =$

$(8mU_0r_0^2/\pi^2\hbar^2)^{1/2}$ the expression for the scattering length (3.15) is exact, and then Eq.(3.17) predicts that $\mu = 1/4 - x_0/\pi + \zeta/2 = 1/4 - \zeta/2 < 0$. This is the $x_0, \zeta \gg 1$ value of the quantum defect in the middle of the small modulation stripe in Fig. 3.5 whose locus, $x_0 = \pi\zeta$, can be deduced from Eq.(3.16). The quantum defect is negative because for continuous $U(r)$ the short-distance rectangular well potential is always less attractive than the Coulomb potential.

3.3 Quantum defect of Rydberg electron

Now when we understand the manifestations of the Zel'dovich effect, and what kind of accuracy is required to approximately capture it, we begin computing the quantum defect of the Rydberg electron as a function of position along the Periodic Table. The quantum defect is given by the exact result Eq.(3.9) with r_0 and a_s , being the size and the scattering length of the residual atomic ion, respectively, both dependent upon atomic number Z . The resulting $\mu(Z)$ dependence will exhibit modulations both due to systematic (Zel'dovich) and shell effects. As discussed in the Introduction, the shell effects obscure systematic trends making it difficult to see that some modulations of $\mu(Z)$ have their origin in the binding properties of the ionic core. To circumvent this inconvenience below we conduct a calculation capturing only systematic effects. The comparison of the results with both experimental and numerical data (additionally containing the shell effects) will allow us to disentangle physically different sources of deviation from purely monotonic behavior.

3.3.1 Method of comparison equations

The short-distance potential $U_s(r)$ characterizing the residual atomic ion will be assumed to match at its boundary the Coulomb potential of unit charge [63],[65] (see Eq.(3.16)). As the Rydberg electron moves inside the ionic core, the screening of the nuclear charge by the inner shell electrons diminishes which implies that for $r < r_0$ the short-distance potential $U_s(r)$ is more attractive than the Coulomb potential of unit charge. Therefore the quantum defect is a necessarily positive and increasing function of atomic number Z . As $r \rightarrow 0$, the inner potential approaches that of a nucleus of charge Ze , i. e. $U_s(r \rightarrow 0) \rightarrow -Ze^2/r = -Z\hbar^2/ma_B r$, and Eq.(3.7) reduces to

$$\frac{d^2\chi}{dr^2} + \frac{2Z}{ra_B}\chi = 0 \quad (3.18)$$

This presents a convenient starting point for obtaining an approximate solution to the differential equation (3.7) via the method of comparison equations as described by Berry and Mount [76]. Since Eq.(3.18) is exactly solvable, and the potentials of Eqs.(3.7) and (3.18) are somewhat similar, the solution to (3.7) should be also similar to that of (3.18) and can be transformed into it by a slight deformation of coordinates and an amplitude adjustment. The details of finding an appropriate mapping are given in Ref. [76]; the resulting approximate solution of (3.7) is then given by

$$\chi(r) \sim \left(\frac{S(r)}{S'(r)} \right)^{1/2} J_1 \left(\frac{S(r)}{\hbar} \right) \quad (3.19)$$

The method of comparison equations includes the conventional semiclassical treatment as a special case [76]. From this more general viewpoint Eq. (3.13) can be viewed as a result of the deformation and amplitude adjustment of the “rectangular well” sine solution.

To assess the accuracy of (3.19) let us first look at the limit $S(r)/\hbar \ll 1$. According to Eq.(3.14) this corresponds to $r \rightarrow 0$ when $U_s(r) \rightarrow -Zh^2/ma_B r$. Then $S(r \rightarrow 0)/\hbar \rightarrow (8Zr/a_B)^{1/2}$ and $\chi(r \rightarrow 0) \sim r^{1/2} J_1(\sqrt{8Zr/a_B})$ which can be recognized as the solution to (3.18).

In the opposite limit $S(r)/\hbar \gg 1$ a semiclassical approximation is expected to be valid and Eq.(3.19) simplifies to $\chi(r) \sim (S'(r))^{-1/2} \sin(S(r)/\hbar - \pi/4)$. This is similar to the naive semiclassical result (3.13) with the extra phase of $-\pi/4$ correcting for the failure of the standard semiclassical treatment in the Coulomb field of charge Ze at distances $r \lesssim a_B/Z$. Thus for the inner potential $U_s(r)$ which has a Coulombic singularity as $r \rightarrow 0$ but is otherwise smooth the analog of Eq.(3.17) is

$$\mu_{sc} = -\frac{x_0}{\pi} + \frac{S_0}{\pi\hbar} \quad (3.20)$$

The expression for the scattering length corresponding to Eq.(3.19) can be found with the help of Eq.(3.8)

$$\frac{a_s}{r_0} = 1 - 4 \left(x_0 \left(\frac{\hbar}{S_0} + \frac{J_0(\frac{S_0}{\hbar}) - J_2(\frac{S_0}{\hbar})}{J_1(\frac{S_0}{\hbar})} \right) - \frac{r_0 U'_s(r_0)}{U_s(r_0)} \right)^{-1} \quad (3.21)$$

where we also used the condition of continuity (3.16). Eq.(3.21) can be used to go beyond the semiclassical expression (3.20). Combining Eqs.(3.12) and (3.21) we find that in the $x_0, S_0/\hbar \gg 1$ limit the quantum defect can be presented as $\mu = \mu_{sc} + \delta\mu$ where μ_{sc} is the semiclassical answer (3.20) and the correction,

$$\delta\mu = \frac{r_0 U'_s(r_0)}{4\pi x_0 U_s(r_0)} \left(1 - \sin \frac{2S_0}{\hbar} \right), \quad (3.22)$$

captures the Zel'dovich effect now manifesting itself as a simple harmonic modulation superimposed on the semiclassical background. The period of the oscillation is exactly one de Broglie's half-wave while the amplitude is of the order x_0^{-1} . The fact that the latter is independent of the number of de Broglie's half-waves fitting inside $U_s(r)$ implies that the Zel'dovich effect persists for any value of $S_0/\pi\hbar$.

3.3.2 Thomas-Fermi model of atomic ion: semiclassical solution

Below we follow Latter [63] and assume that the potential of the atomic ion $U_s(r)$ can be approximated by the Thomas-Fermi theory [77]:

$$U_s(r) = -\frac{\hbar^2 Z}{ma_B r} \phi\left(\frac{rZ^{1/3}}{ba_B}\right) \quad (3.23)$$

where $b = (3\pi/4)^{1/2}/2 \simeq 0.885$, and the universal function $\phi(y)$ is the solution to the nonlinear Thomas-Fermi equation

$$y^{1/2} \frac{d^2 \phi}{dy^2} = \phi^{3/2} \quad (3.24)$$

subject to the boundary conditions $\phi(0) = 1$ and $\phi(\infty) = 0$ [77]. Then the size of the ion r_0 and thus the range parameter x_0 (3.5) are determined by the continuity condition (3.16), i. e. when the Thomas-Fermi potential (3.23) meets the Coulomb potential of unit charge:

$$\phi\left(\frac{x_0^2 Z^{1/3}}{8b}\right) = \frac{1}{Z} \quad (3.25)$$

Eqs. (3.23) and (3.25) imply that the natural variable to characterize the strength of the potential of the atomic ion is $Z^{1/3}$. Indeed, the typical length scale of the Thomas-Fermi theory is $a_B/Z^{1/3}$, the magnitude of the typical potential is $(Z\hbar^2/ma_B)(Z^{1/3}/a_B) = (\hbar^2/ma_B^2)Z^{4/3}$, and thus the dimensionless coupling constant $w \simeq mr_0^2|U_s|/\hbar^2$ which entered the general analysis of Section 3.2 is of the order $Z^{2/3}$; the parameter $Z^{1/3}$ then parallels $\zeta \simeq w^{1/2}$ used in the rectangular well example of the inner potential.

Since the Thomas-Fermi function $\phi(y)$ is a monotonically decreasing function of its argument, the $x_0(Z^{1/3})$ dependence defined through Eq.(3.25) is a monotonically increasing function of $Z^{1/3}$. The boundary condition $\phi(0) = 1$ implies that $x_0(1) = 0$ which is in accordance with the expectation that for Hydrogen ($Z = 1$) we have the standard Coulomb problem in the whole space ($x_0 = 0$). As

evident from (3.25) small values of ϕ are relevant for large Z ; in view of $\phi(y \rightarrow \infty) \rightarrow 144/y^3$ [77] this means that there is an upper bound to the range parameter, $x_0(\infty) = 2^{13/6} 3^{1/3} b^{1/2} \simeq 6.092$.

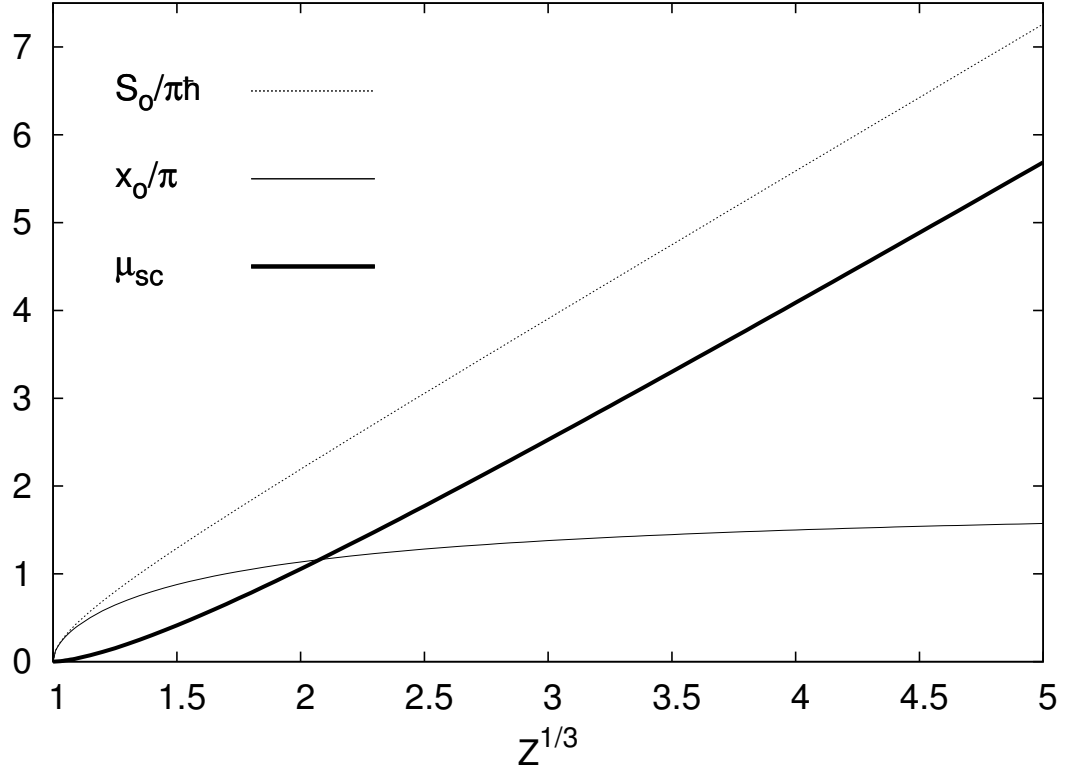
Another quantity of interest is the number of de Broglie's half-waves fitting inside the Thomas-Fermi atomic ion

$$\begin{aligned} \frac{S_0}{\pi\hbar} &= \int_0^{r_0} \left(\frac{-2mU_s(r)}{\pi^2\hbar^2} \right)^{1/2} dr \\ &= \frac{(2b)^{1/2} Z^{1/3}}{\pi} \int_0^{x_0^2 Z^{1/3}/8b} \left(\frac{\phi(y)}{y} \right)^{1/2} dy \end{aligned} \quad (3.26)$$

which is a monotonically increasing function of $Z^{1/3}$: for $Z \rightarrow 1$ it vanishes as x_0/π while for large Z we have $S_0/\pi\hbar \sim Z^{1/3}$, a known result [67].

For intermediate values of the atomic number the $Z^{1/3}$ dependences of the range parameter x_0 and the number of de Broglie's half-waves $S_0/\pi\hbar$ can be found by numerically solving the Thomas-Fermi equation (3.24), inverting (3.25), and computing the integral (3.26). The results are displayed in Fig. 3.6 where we show x_0/π and $S_0/\pi\hbar$ as functions of $Z^{1/3}$. These functions are used to also plot the semiclassical quantum defect given by Eq.(3.20). To assess the accuracy of the resulting $\mu_{sc}(Z^{1/3})$ dependence we need to verify whether approximations used to derive Eq.(3.20) are adequate. The first assumption, $x_0 \gg 1$, is equivalent to the assertion that the quantum defect for $U_s(r) = 0$ can be replaced by its large x_0 limit. Looking at Fig. 3.1 where the dependences in question are compared we conclude that “large” here really means $x_0 \gtrsim \pi$. The second, semiclassical assumption $S_0/\hbar \gg 1$ in practice has a good accuracy provided $S_0/\pi\hbar$, the number of de Broglie's half-waves fitting into the inner potential $U_s(r)$, is anything more than one or two. Inspecting Fig. 3.6 we see that the conditions $x_0/\pi \gtrsim 1$ and $S_0/\pi\hbar \gtrsim 2$ are satisfied for $Z \gtrsim 8$. This is also the practical condition for the Thomas-Fermi-Latter model of the residual ion to be applicable. We note additionally that although Eq.(3.20) is not expected to be valid for smallest Z , the limit $\mu(1) = 0$ is nevertheless correctly reproduced and for any Z the semiclassical quantum defect is an increasing positive function of $Z^{1/3}$ in accordance with physical expectation. We conclude that except possibly for the elements of the first row of the Periodic Table, the semiclassical result for the quantum defect Eq.(3.20) shown in Fig. 3.6 is accurate; only qualitative agreement is expected for lightest elements.

Figure 3.6: Plots of the number of de Broglie's half-waves $S_0/\pi\hbar$, (3.26), the range parameter x_0/π , (3.25), and semiclassical quantum defect μ_{sc} , (3.20) as functions of $Z^{1/3}$ for the Thomas-Fermi model of the residual atomic ion.



3.3.3 Beyond semiclassical approximation: connection to binding properties of ionic core

A more accurate $\mu(Z^{1/3})$ dependence can be found by computing the scattering length (3.21) and substituting the outcome together with the $x_0(Z^{1/3})$ dependence, Fig. 3.6, in our general expression for the quantum defect (3.9). The result is shown in Fig. 3.7 where we also plot the semiclassical quantum defect, μ_{sc} , Eq.(3.20) (gray scale). It now becomes obvious that for any Z the bulk contribution into the quantum defect is well-captured semiclassically. The Zel'dovich spectral modulation clearly visible in Fig. 3.7 is a relatively weak effect. To separate the modulation from the monotonic semiclassical background the inset shows the difference $\delta\mu = \mu - \mu_{sc}$ which appears to be a nearly periodic function of $Z^{1/3}$. To better understand the meaning of this periodicity the inset also shows the limiting expression (3.22) (gray scale) [78]. Both curves are exactly in phase and for sufficiently heavy elements their magnitudes agree semi-quantitatively. This observation implies that the Zel'dovich modulation is a periodic function of the number of de Broglie's half-waves fitting inside the ionic core of the atom.

A complementary way to see the connection between the spectral modulation and the binding properties is presented in Fig. 3.8 where we compare the $\delta\mu(Z^{1/3})$ dependence with the behavior of the scattering length of the residual atomic ion (3.21). The latter, numerically computed for the Thomas-Fermi model of the residual atomic ion, Eqs.(3.23) - (3.26), is shown in gray scale. The binding singularities of the scattering length are nearly equidistant confirming the earlier observation that the parameter $Z^{1/3}$ is analogous to ζ used in Figs. 3.3 and 3.5 to display the Zel'dovich effect for the rectangular well model of the inner potential. A qualitatively similar behavior of the scattering length of the Thomas-Fermi atom as a function of Z has been reported by Robinson [79]; quantitative differences may be attributed to the assumption [79] that the Thomas-Fermi potential vanishes at a distance of the order $a_B/Z^{1/3}$ which is different from our choice of r_0 , Eqs.(3.16) and (3.25).

Fig. 3.8 makes it clear that the maxima of the oscillations of $\delta\mu$ occur when $a_s = r_0$, i. e. when the node of the function $\chi(r)$ in Eq.(1) coincides with the boundary of the atomic ion. On the other hand, the minima of $\delta\mu$ are correlated with binding singularities of the ionic core, $a_s = \pm\infty$, thus corresponding to the antinode of $\chi(r)$ being near the ion boundary.

Figure 3.7: Dependence of the quantum defect μ on $Z^{1/3}$ along with its semiclassical approximant μ_{sc} , Eq.(3.20) (gray scale). The inset shows the Zel'dovich modulation $\delta\mu(Z^{1/3}) = \mu - \mu_{sc}$ together with the limiting expression, Eq.(3.22) (gray scale).

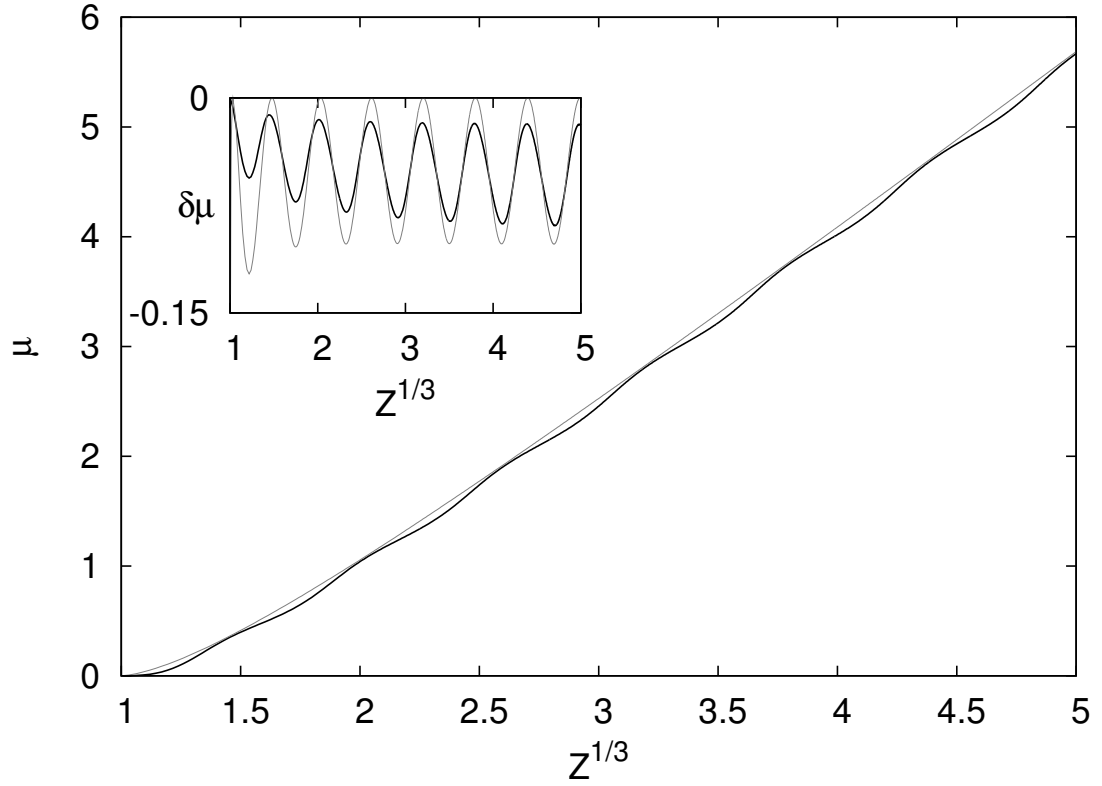
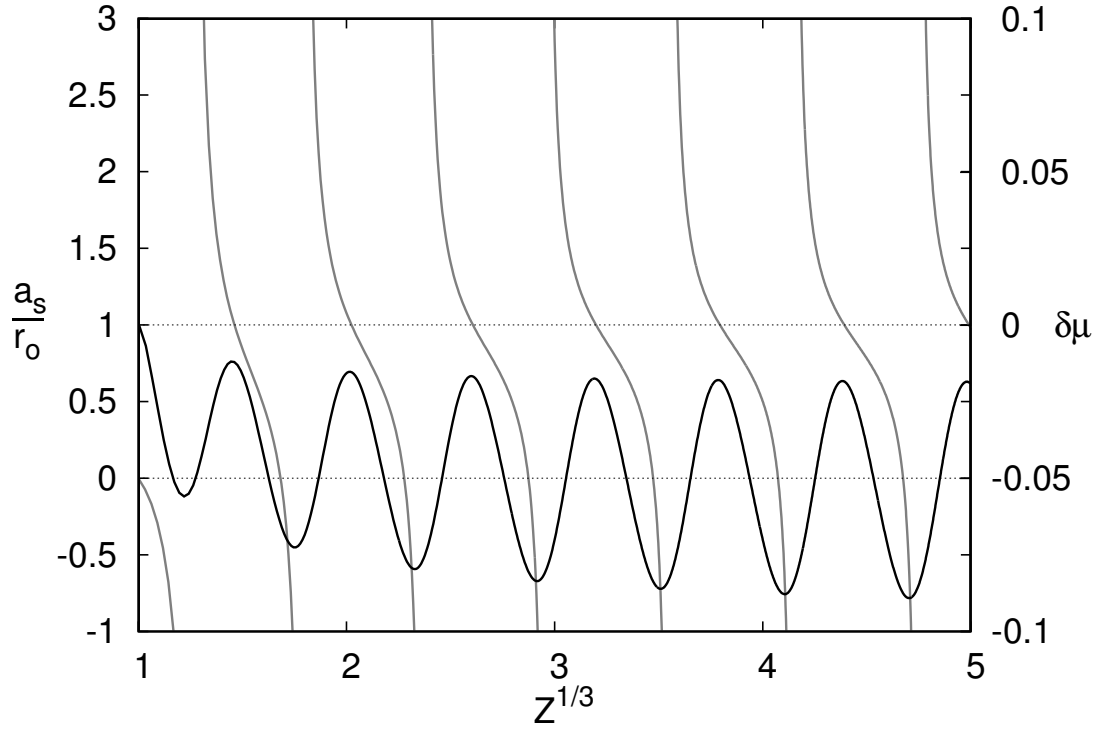


Figure 3.8: Dependences of the Zel'dovich modulation $\delta\mu = \mu - \mu_{sc}$ and the reduced scattering length of the ionic core a_s/r_0 (gray scale) on $Z^{1/3}$. The lines $a_s/r_0 = 0$ and $a_s/r_0 = 1$ are also shown to help the eye.



3.4 Comparison with experimental and numerical data

We found experimental values of quantum defects for 37 elements of the Periodic Table. These data and their sources are compiled in Table 3.1 where we also list systematic quantum defects of our work (also displayed in Fig. 3.7). Some of the figures which we regard as “experimental” came from an on-line database [82] where the quantum defect is computed from available spectroscopic data.

In cases of He, Be, Mg, Ca, and Mo there is more than one value of the quantum defect available depending on the angular momentum of the ionic core of the atom. Since our theory represents average properties and does not distinguish between different LS terms of an atomic configuration, in Table 3.1 we chose to show only the values corresponding to lowest angular momentum of the ionic core. It turns out they better agree with our calculation than those left out.

The works of Manson [64] and Fano, Theodosiou and Dehmer [65] contain graphs of numerically evaluated $\mu(Z)$ dependence for all elements. After verifying that the results of both studies are nearly identical, we chose to restrict ourselves to those of the later Ref.[65].

Experimental, numerical and systematic $\mu(Z^{1/3})$ dependences are displayed in Fig. 3.9. In order to produce the numerical curve, the data [65] have been scanned, digitized, and replotted as a function of $Z^{1/3}$. We also circled locations of alkali metals because their ionic cores have noble element electronic configurations thus marking (for the Rydberg atom problem) the end of a period.

Fig. 3.9 makes it clear that all three dependences are in fairly good agreement and $Z^{1/3}$ is certainly the right variable to use for analysis. It is not surprising that numerical results [65] are generally in better agreement with experimental data than our systematic findings because our calculation omits the shell effects.

3.4.1 Effects of shell structure

In order to be able to separate systematic and shell effects, in Fig. 3.10 we display $\delta\mu = \mu - \mu_{sc}$, the modulation of the quantum defect relative to the monotonic semiclassical background, Eq.(3.20), which accounts for the bulk of the quantum defect value. Fig. 3.10 shows that the experimental and numerical variations of the quantum defect are bounded which is consistent with the view that they are due to repetitive physics. Moreover, the systematic modulation due to the Zel’dovich effect appears to have an amplitude which is several times smaller than those of experimental and numerical data. This observation implies that it may be possible to understand gross features of the

Table 3.1: Experimentally measured quantum defects for series of elements with their atomic numbers Z and corresponding references. Systematic quantum defects of this work are also displayed for comparison.

| Z | Element | Experimental μ | Reference | Systematic μ |
|-----|---------|--------------------|-----------|------------------|
| 2 | He | .139 | [80] | .110 |
| 3 | Li | .400 | [81] | .336 |
| 4 | Be | .670 | [82] | .478 |
| 5 | B | 1.000 | [82] | .600 |
| 6 | C | 1.050 | [82] | .744 |
| 7 | N | 1.091 | [82] | .904 |
| 8 | O | 1.132 | [82] | 1.040 |
| 9 | F | 1.203 | [82] | 1.144 |
| 10 | Ne | 1.300 | [83] | 1.229 |
| 11 | Na | 1.348 | [81] | 1.307 |
| 12 | Mg | 1.517 | [82] | 1.388 |
| 13 | Al | 1.758 | [84] | 1.476 |
| 14 | Si | 1.816 | [82] | 1.574 |
| 16 | S | 1.947 | [82] | 1.774 |
| 17 | Cl | 2.128 | [85] | 1.861 |
| 18 | Ar | 2.140 | [83] | 1.935 |
| 19 | K | 2.180 | [81] | 1.999 |
| 20 | Ca | 2.340 | [80] | 2.056 |
| 22 | Ti | 2.400 | [86] | 2.161 |
| 23 | V | 2.300 | [86] | 2.134 |
| 26 | Fe | 2.600 | [86] | 2.390 |
| 29 | Cu | 2.600 | [80] | 2.594 |
| 30 | Zn | 2.639 | [87] | 2.660 |
| 36 | Kr | 3.100 | [83] | 2.956 |
| 37 | Rb | 3.131 | [88] | 2.994 |
| 38 | Sr | 3.269 | [80] | 3.031 |
| 39 | Y | 3.385 | [89] | 3.067 |
| 42 | Mo | 3.476 | [90] | 3.180 |
| 47 | Ag | 3.600 | [91] | 3.404 |
| 49 | In | 3.720 | [92] | 3.503 |
| 54 | Xe | 4.000 | [83] | 3.722 |
| 55 | Cs | 4.049 | [93] | 3.759 |
| 56 | Ba | 4.200 | [80] | 3.793 |
| 70 | Yb | 4.280 | [80] | 4.193 |
| 78 | Pt | 4.611 | [89] | 4.479 |
| 79 | Au | 4.660 | [94] | 4.515 |
| 83 | Bi | 4.890 | [80] | 4.645 |

Figure 3.9: Systematic, experimental, and numerical dependences of the quantum defect μ on $Z^{1/3}$. To help orientation within the Periodic Table experimental alkali data are circled.

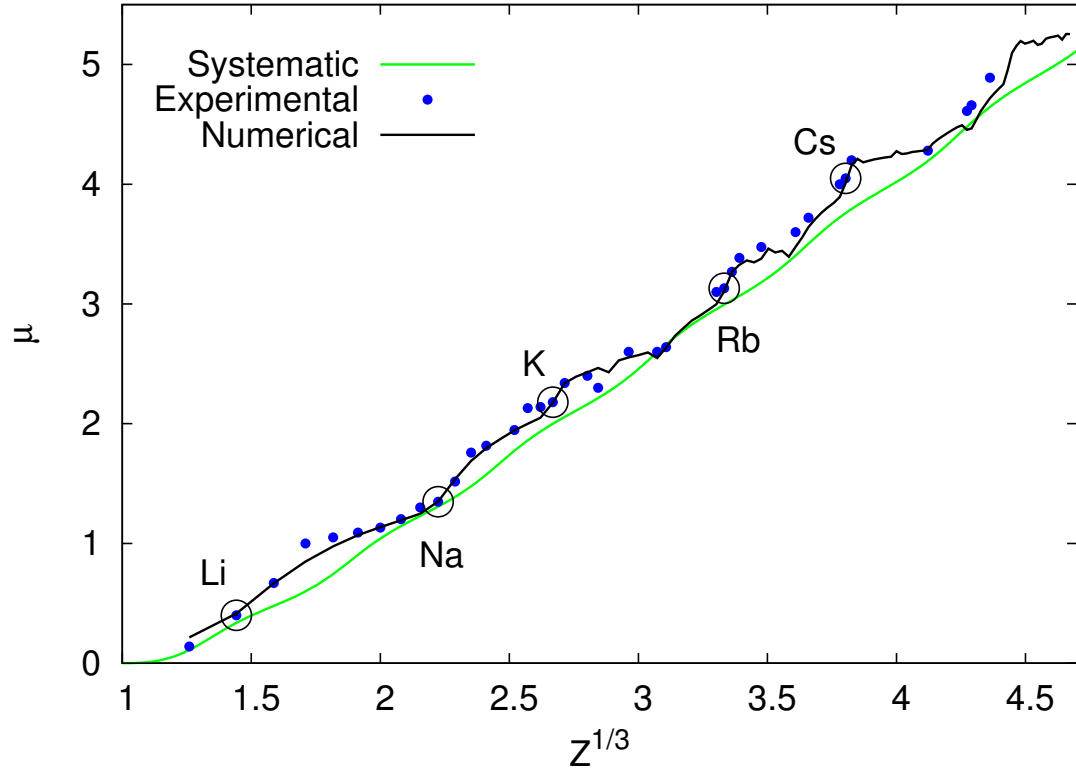
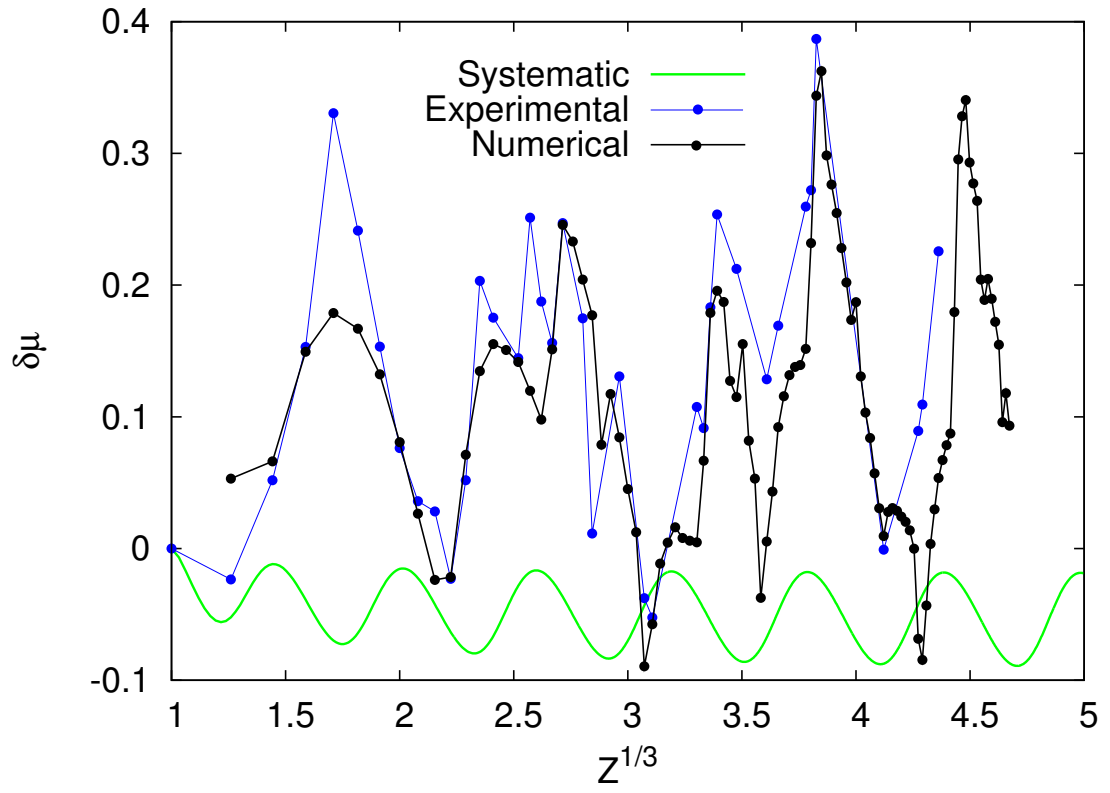


Figure 3.10: Modulation of systematic, experimental and numerical quantum defect $\delta\mu = \mu - \mu_{sc}$ relative to the semiclassical background, Eq.(3.20) as a function of $Z^{1/3}$.



experimental and numerical modulations of the quantum defect as mostly due to the effects of the shell structure.

This viewpoint can be supported by qualitative analysis which rests on the semiclassical result (3.20). First, let us anticipate the outcome of incorporating the shell effects into the calculation. This amounts to replacing the smooth inner potential $U_s(r)$ by one with modulations due to the spatial variation of the electron density reflecting the shell structure. This replacement will result in a value of the size of the ionic core r_0 , Eq.(3.16), generally different from its systematic counterpart.

Let us additionally assume that the inner potential $U_s(r)$ with shell effects included is still sufficiently smooth so that a semiclassical treatment is valid. The corresponding quantum defect (3.20) will deviate away from the systematic result due to different values of the range parameter x_0 , Eq.(3.5), and the number of de Broglie's half-waves, $S_0/\pi\hbar$. Because the latter involves the integral of $(-U_s(r))^{1/2}$ from zero to r_0 (see Eqs.(3.14) and (3.26)) the modulations above and below the systematics present in $U_s(r)$ are expected to largely cancel each other and the deviation from our results can be mostly attributed to the different size of the ionic core.

This argument implies that the quantum defect is strongly sensitive to the value of the size of the ionic core r_0 and weakly sensitive to the details of the inner potential $U_s(r)$. In reality the inner potential may not be smooth enough for the semiclassical treatment to be quantitatively correct. Therefore we do not expect more than a qualitative insight into the trends of the variations of the quantum defect induced by the shell effects.

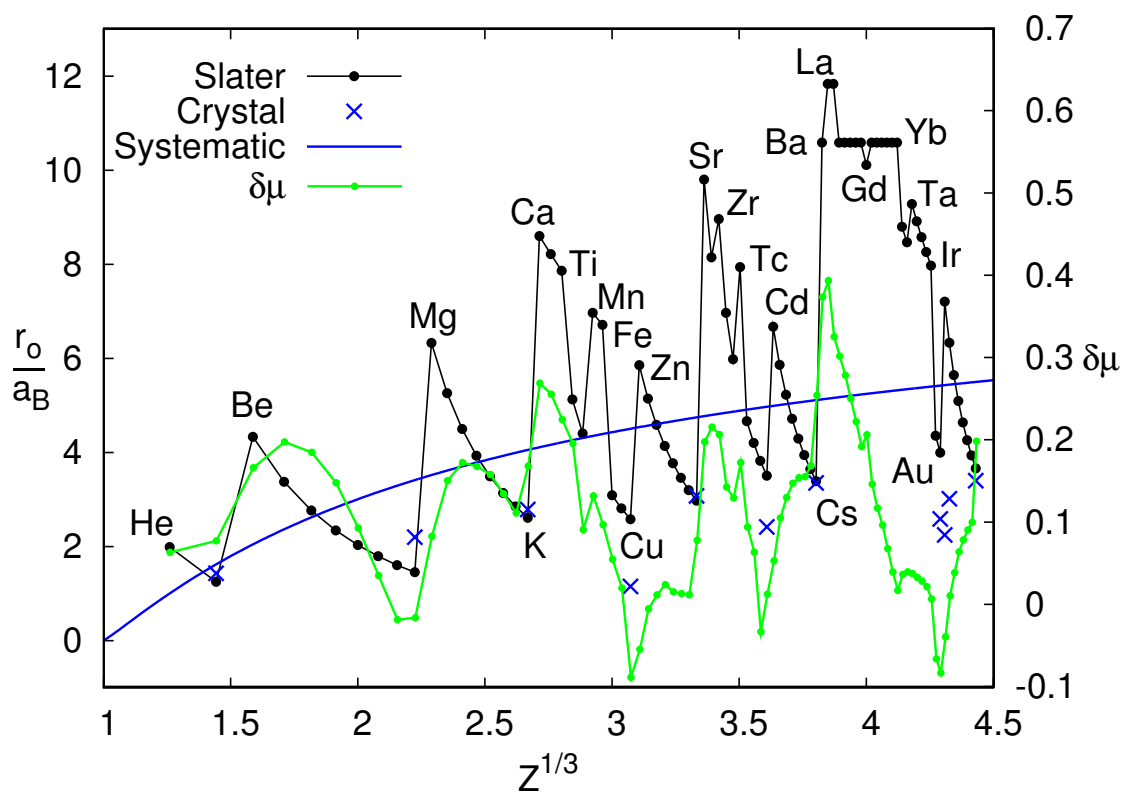
The simple rule that emerges can be most easily deduced from Fig. 3.6 by keeping in mind the relationship between the range parameter x_0 , Eq.(3.5) and the size of the ionic core $r_0 \propto x_0^2$: deviation in r_0 away from systematics leads to the same sign deviation in the quantum defect.

Since the size of the ionic core of the Rydberg atom has a physical meaning close to that of an ionic radius, to verify the correlation we need a set of ionic radii for singly-charged positive ions as a function of position Z along the Periodic Table.

Seventy five years ago J. C. Slater [95] gave a very useful, general, empirical set of rules to approximate analytically atomic wave functions for all the elements in any stage of ionization. The radial part of the single-electron wave function is selected in the form

$$\psi(r) \propto r^{n^*-1} e^{-Z^*r/n^*a_B} \quad (3.27)$$

Figure 3.11: Slater's ionic radii for singly-charged positive ions together with a series of corresponding ionic radii in crystals and systematic sizes of ionic core of the Rydberg atom, all in atomic units, as functions of $Z^{1/3}$. Numerical variation of the quantum defect $\delta\mu = \mu - \mu_{sc}$ is also displayed to show the correlation with Slater's radii.



which can be recognized as the large-distance asymptotics of a Hydrogen-like wave function with an effective quantum number n^* and an effective nuclear charge Z^*e . Based on the underlying electronic structure, Slater's rules assign values of n^* and Z^* to the electrons of each shell of an atom or ion, so that a complete set of single-electron wave functions can be constructed.

For a given shell the maximum of the electron density $4\pi r^2 \psi^2(r)$ is located at

$$r_{max}/a_B = (n^*)^2/Z^* \quad (3.28)$$

which formally coincides with the expression for the radius of the corresponding circular orbit in Bohr's old theory. The radius of the maximum density of the outermost shell is expected to correlate with the size of the atom or ion. Specifically, Slater defines an ionic radius $r_0 > r_{max}$ as a distance at which the electron density becomes 10% of its maximal value.

Using the existing knowledge of electronic configurations [96] we applied Slater's rules to calculate the ionic radii of singly-charged positive ions. The result is shown in Fig. 3.11 where the elements marking the beginning or an end of more dramatic changes in the ionic radius are labeled. For comparison we also displayed a series of ionic crystal radii [97] used for predicting and visualizing crystal structures. Crystal ionic radii are based on experimental crystal structure determinations, empirical relationships, and theoretical calculations. As Fig. 3.11 shows, they are in fair agreement with their Slater's counterparts. We hasten to mention that neither Slater's nor the crystal ionic radii are expected to coincide with what we define as the size of the ionic core of the Rydberg atom, Eq.(3.16). It seems highly plausible, however, that Slater's ionic radii are correlated with the sizes of the ionic cores of the Rydberg atoms.

Inspection of Fig. 3.11 tells us that the average Slater's ionic radius slowly grows with $Z^{1/3}$ in fairly good agreement with our systematic result. A closer look reveals that our systematic radius appears to be consistently smaller than its Slater's counterpart. If the same relationship would hold between the systematic and (unknown) exact sizes of the ionic cores of Rydberg atoms, then the fact that experimental and numerical quantum defects in Figs. 3.9 and 3.10 are generally larger than their systematic counterparts would be explained.

The large variation of the Slater's ionic radius away from the average trend is due to the effects of shell structure. Their role in determining the ionic radius can be most easily visualized based on the expression for the radius of the maximum electron density (3.28) which correlates with the ionic

radius. This result emphasizes the following main principles:

(i) As Z increases, all the n levels move down in energy which amounts to replacing n by its effective counterpart $n^* \leq n$. If the electrons are added to an outer shell, the effective nuclear charge Z^*e seen by each of them gradually increases. This is because the outer shell electrons are relatively inefficient in shielding the nuclear charge. As a result the ion slowly contracts.

(ii) As a new outer shell begins to fill, the effect of going into the higher shell outweighs the effect of lowering of an n level as Z increases to $Z + 1$. This corresponds to an abrupt increase of the effective principal quantum number n^* . Moreover, the effective charge Z^*e seen by the outermost electron drops because now all remaining $Z - 2$ electrons belong to inner shells thus efficiently screening the nuclear charge. These changes in n^* and Z^* cause a sharp increase of the ion size.

Slater's rules [95] add a quantitative aspect to these principles. In the following explanation of the variation of the ionic radius, Fig. 3.11, we are always speaking of the positive singly-charged ions whose electronic configurations are taken from the NIST database [96].

In going from ${}^2\text{He}$ ($1s^1$), to ${}^3\text{Li}$ ($1s^2$) the ion size decreases. As one moves to ${}^4\text{Be}$ ($[\text{He}]2s^1$) the added electron enters the higher $2s$ shell, and the ionic radius sharply increases. Similar increases take place as one goes from every alkali to the following alkali earth ion. A related jump in ionic radius also occurs past every noble element ion, ${}^{29}\text{Cu}$ ($[\text{Ar}]3d^{10}$) \rightarrow ${}^{30}\text{Zn}$ ($[\text{Ar}]3d^{10}4s^1$), ${}^{47}\text{Ag}$ ($[\text{Kr}]4d^{10}$) \rightarrow ${}^{48}\text{Cd}$ ($[\text{Kr}]4d^{10}5s^1$), and ${}^{79}\text{Au}$ ($[\text{Xe}]4f^{14}5d^{10}$) \rightarrow ${}^{80}\text{Hg}$ ($[\text{Xe}]4f^{14}5d^{10}6s^1$) because a higher s -shell starts to be occupied. An analogous argument explains the sharp increase of ionic radius while going from ${}^{24}\text{Cr}$ ($[\text{Ar}]3d^5$) to ${}^{25}\text{Mn}$ ($[\text{Ar}]3d^54s^1$) and from ${}^{42}\text{Mo}$ ($[\text{Kr}]4d^5$) to ${}^{43}\text{Tc}$ ($[\text{Kr}]4d^55s^1$)

As one moves from ${}^4\text{Be}$ ($[\text{He}]2s^1$) to ${}^{11}\text{Na}$ ($[\text{He}]2s^22p^6$) the $2s$ and $2p$ shells are filled by the electrons, and the ion size gradually decreases. A similar effect explains the decrease of the ionic radius along the ${}^{12}\text{Mg}$ ($[\text{Ne}]3s^1$)– ${}^{19}\text{K}$ ($[\text{Ne}]3s^23p^6$), ${}^{30}\text{Zn}$ ($[\text{Ar}]3d^{10}4s^1$)– ${}^{37}\text{Rb}$ ($[\text{Ar}]3d^{10}4s^24p^6$), ${}^{48}\text{Cd}$ ($[\text{Kr}]4d^{10}5s^1$)– ${}^{55}\text{Cs}$ ($[\text{Kr}]4d^{10}5s^25p^6$), and ${}^{80}\text{Hg}$ ($[\text{Xe}]4f^{14}5d^{10}6s^1$)– ${}^{87}\text{Fr}$ ($[\text{Xe}]4f^{14}5d^{10}6s^26p^6$) sequences.

The ionic radius decreases through the ${}^{20}\text{Ca}$ ($[\text{Ar}]4s^1$)– ${}^{21}\text{Sc}$ ($[\text{Ar}]3d^14s^1$)– ${}^{22}\text{Ti}$ ($[\text{Ar}]3d^24s^1$) segment. This happens because the electrons filling the $3d$ shell only partially screen the nuclear charge - as a result the outer $4s$ electron sees a gradual increase of effective Z^* . The same argument explains the decrease of ion size while going from ${}^{25}\text{Mn}$ ($[\text{Ar}]3d^54s^1$) to ${}^{26}\text{Fe}$ ($[\text{Ar}]3d^64s^1$) which is merely a continuation of the Ca-Ti segment. The decrease of ionic radius through the ${}^{73}\text{Ta}$ ($[\text{Xe}]4f^{14}5d^36s^1$)– ${}^{77}\text{Ir}$ ($[\text{Xe}]4f^{14}5d^76s^1$) series can be similarly understood. In fact, the first entry of this series is ${}^{70}\text{Yb}$ ($[\text{Xe}]4f^{14}5d^06s^1$) where we intentionally modified the standard notation to show the absence of the

5d electron.

The size of the ion first abruptly decreases while going from ^{22}Ti ($[\text{Ar}]3d^24s^1$) to ^{23}V ($[\text{Ar}]3d^4$) and then continues decreasing more gradually as one moves to ^{24}Cr ($[\text{Ar}]3d^5$). The sudden change is due to the fact that the outer shell changes from 4s to 3d which can be viewed as a decrease in the effective quantum number n^* . The subsequent slower increase of the ionic radius is due to the increase of the effective nuclear charge Z^*e seen by the larger number of 3d electrons. The same trend is exhibited in the ^{40}Zr ($[\text{Kr}]4d^25s^1$)– ^{41}Nb ($[\text{Kr}]4d^4$)– ^{42}Mo ($[\text{Kr}]4d^5$) sequence. A very similar behavior is found in the ^{26}Fe ($[\text{Ar}]3d^64s^1$)– ^{27}Co ($[\text{Ar}]3d^8$)– ^{28}Ni ($[\text{Ar}]3d^9$)– ^{29}Cu ($[\text{Ar}]3d^{10}$), ^{43}Tc ($[\text{Kr}]4d^55s^1$)– ^{44}Ru ($[\text{Kr}]4d^7$)– ^{45}Rh ($[\text{Kr}]4d^8$)– ^{46}Pd ($[\text{Kr}]4d^9$)– ^{47}Ag ($[\text{Kr}]4d^{10}$), and ^{77}Ir ($[\text{Xe}]4f^{14}5d^76s^1$)– ^{78}Pt ($[\text{Xe}]4f^{14}5d^9$)– ^{79}Au ($[\text{Xe}]4f^{14}5d^{10}$) series.

Superficially, a similar steep decrease of the ion size is followed by more gradual decrease in the ^{70}Yb ($[\text{Xe}]4f^{14}6s^1$)– ^{71}Lu ($[\text{Xe}]4f^{14}6s^2$)– ^{72}Hf ($[\text{Xe}]4f^{14}5d^16s^2$) sequence. This behavior can be explained by noticing that in both steps the effective Z^* felt by a 6s electron increases; the increase during the second step is smaller because inner shell d electrons are more efficient in screening the nuclear charge than s electrons.

While going from ^{38}Sr ($[\text{Kr}]5s^1$) to ^{39}Y ($[\text{Kr}]5s^2$) and to ^{40}Zr ($[\text{Kr}]4d^25s^1$) a decrease of ionic radius follows by an increase. This happens because the effective Z^* felt by an outer 5s electron first increases and then decreases. The increase of the size of the ion is somewhat smaller than the decrease because two 4d electrons in Zr only partially shield two extra units of the nuclear charge.

For the ^{63}Eu ($[\text{Xe}]4f^76s^1$)– ^{64}Gd ($[\text{Xe}]4f^75d^16s^1$)– ^{65}Tb ($[\text{Xe}]4f^96s^1$) sequence the ionic radius first decreases and then increases back to its initial value. This happens because the d electron in Gd is less effective in shielding the nuclear charge than the f electron in Tb (considered perfect in Slater's scheme).

One of the less intuitive increases of ionic radius takes place while going from ^{56}Ba ($[\text{Xe}]6s^1$) to ^{57}La ($[\text{Xe}]5d^2$). On one hand, the effective principal quantum number n^* decreases which according to (3.28) should lower the ionic radius. However as compared to the 6s electron of Ba, the effective Z^* seen by one of La's 5d electrons also decreases. This happens because the inner shell 5sp electrons screen the nuclear charge more effectively if the outer shell electrons are in a d state (La) as compared to an s state (Ba). As a result the decrease in Z^* outweighs the decrease in n^* thus leading to an increase of the ion size. A very similar argument explains the reversed decrease of ionic radius taking place as one goes from ^{58}Ce ($[\text{Xe}]4f^15d^2$) (whose size is identical to that of La) to ^{59}Pr ($[\text{Xe}]4f^36s^1$)

(identical in size to Ba). Here the role of the $4f$ electrons merely reduces to compensating for the increase of the nuclear charge.

The ionic radius does not change as one moves from ^{57}La ($[\text{Xe}]5d^2$) to ^{58}Ce ($[\text{Xe}]4f^15d^2$) because the increase of nuclear charge is exactly compensated by adding a $4f$ electron. The same argument explains the constancy of the ionic radius along most of the lanthanide sequence, ^{59}Pr ($[\text{Xe}]4f^36s^1$)– ^{63}Eu ($[\text{Xe}]4f^76s^1$), ^{65}Tb ($[\text{Xe}]4f^96s^1$)– ^{70}Yb ($[\text{Xe}]4f^{14}6s^1$). The only exception from this trend, ^{64}Gd ($[\text{Xe}]4f^75d^16s^1$), has already been discussed.

Now when the variations of the Slater's ionic radius are understood, we can compare them with experimental and numerical modulations of the quantum defect. Since the numerical data are more extensive than experimental findings, and the agreement between the two is fairly good, in Fig. 3.11 we only show the variation of the numerically evaluated quantum defect $\delta\mu = \mu - \mu_{sc}$. The inspection of Fig. 3.11 leaves no doubt that the variations of the quantum defect with $Z^{1/3}$ are correlated with those of the Slater's ionic radius - even the minute changes of the latter find their way in the corresponding changes of the former.

There are however two places where it appears there is a disagreement with expectation:

(i) Along most of the lanthanide sequence the Slater's ionic radius does not change while the variation of the quantum defect decreases. This can be understood as an artifact of Slater's rules. In reality the f electrons do not perfectly screen the nuclear charge. Therefore the effective charge seen by the outer $6s$ electron increases with $Z^{1/3}$ and correspondingly the ionic radius should decrease. Then the quantum defect variation should decrease as well which is in correspondence with numerical results. We also note that the Gd dip of the ionic radius is reproduced in the quantum defect variation.

(ii) For the elements past Hg, the Slater's ionic radius decreases with $Z^{1/3}$ while the variation of the quantum defect increases. The reason why it happens is unclear. It cannot be ruled out that here the effects of the shell structure might be so strong that our correlation rule derived from semiclassical arguments breaks down qualitatively.

Overall, the analysis of this section makes it certain that the gross features of the quantum defect variation with $Z^{1/3}$ are due to the effects of the shell structure.

3.4.2 Zel'dovich modulation

Qualitative analysis is of little use in trying to see the Zel'dovich effect in experimental and numerical data because the Zel'dovich modulation has an amplitude which is several times smaller than that due to the effects of the shell structure (see Fig. 3.10). A way to proceed quantitatively is suggested by the fashion in which the shell and systematic effects are coupled.

Inspecting the limiting expression for the Zel'dovich modulation, Eq.(3.22), it is straightforward to see that after replacing systematic $U_s(r)$ with the one accounting for the shell structure, the amplitude of the Zel'dovich modulation will become strongly sensitive to the effects of the shell structure because it is determined by the logarithmic derivative of the inner potential $U_s(r)$ and the range parameter x_0 . On the other hand, the period of the oscillation is far less sensitive to the effects of the shell structure since it is determined by the number of de Broglie's half-waves fitting inside the ionic core of the atom.

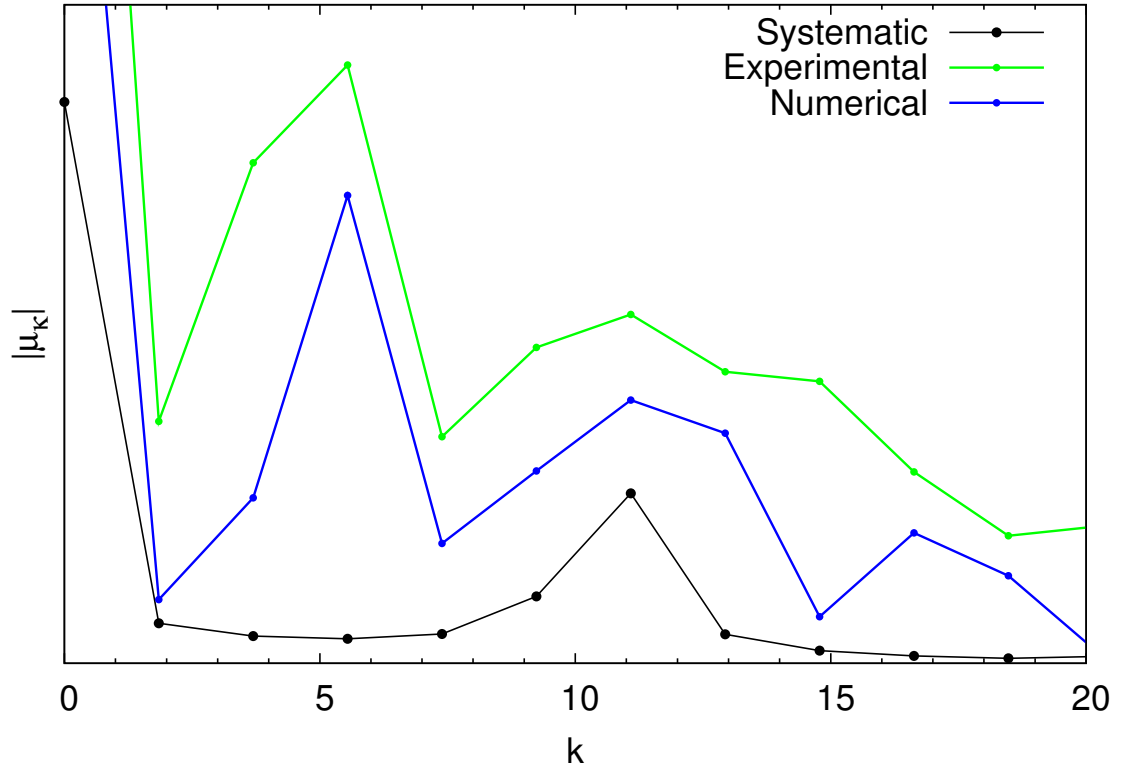
This last observation suggests that it might be possible to see the Zel'dovich effect in the experimental and numerical Fourier spectra of the quantum defect variation $\delta\mu = \mu - \mu_{sc}$ (see Fig. 3.10) as a peak whose location can be brought in correspondence with the systematic theory. To proceed in this direction, in a range of $Z^{1/3}$ of length L we expand the quantum defect variation into a Fourier series

$$\delta\mu(Z^{1/3}) = \sum_{k=2\pi p/L} \mu_k \exp(ikZ^{1/3}) \quad (3.29)$$

where $p = 0, \pm 1, \pm 2, \dots$. In order to numerically evaluate the Fourier coefficients $\mu_k = \mu_{-k}^*$, the experimental and numerical $\delta\mu(Z^{1/3})$ dependences (see Fig. 3.10) were fitted with a cubic spline which was then sampled equidistantly in $Z^{1/3}$ to extract the Fourier spectrum. The result for the magnitude of the Fourier coefficients $|\mu_k|$ as a function of k is displayed in Fig. 3.12 as a series of solid dots which for convenience are connected by straight line segments. The uncertainty of the location of each dot along the k axis, $2\pi/L$, is the distance between the nearest values of k . Since the last available experimental quantum defect corresponds to ^{83}Bi (see Table 3.1), for both experimental and numerical data we restricted ourselves to $L = 83^{1/3}$. The finite values of μ_0 correspond to the presence of nonzero background in experimental and numerical $\delta\mu(Z^{1/3})$ dependences and are of no interest to us.

For comparison in Fig. 3.12 we also show the Fourier spectrum of our systematic calculation which, as expected, has only one peak corresponding to the Zel'dovich effect. The position of the

Figure 3.12: Systematic, experimental and numerical amplitudes of the Fourier coefficients of the quantum defect variation (arbitrary units, same normalization) $|\mu_k|$ as functions of k for $k \geq 0$. The peaks at $k \simeq 11$ correspond to the Zel'dovich effect.



peak along the k axis can be understood from the large Z asymptotics of the Thomas-Fermi action $S_0/\hbar \simeq 5.2Z^{1/3}$ (3.26). Comparing this with the limiting expression for the Zel'dovich modulation (3.22) we would expect a peak at $k \simeq 10.4$. The peak in Fig. 3.12 is located at a slightly different value of $k \simeq 11$ which is due to the fact that the asymptotic behavior $S_0/\hbar \simeq 5.2Z^{1/3}$ becomes numerically accurate only for $Z^{1/3}$ exceeding 10.

Both the experimental and numerical spectra in Fig. 3.12 have peaks at the same value of $k \simeq 11$ which we argue are the signatures of the Zel'dovich effect.

It is curious that both experimental and numerical spectra have another peak in common located at $k \simeq 5.5$. This peak which is about twice as high as that due to the Zel'dovich effect is natural to relate to the effects of the shell structure. The existence of this peak translates into the $(2\pi/5.5)Z^{1/3} = 1.14Z^{1/3}$ periodicity of the quantum defect variation due to the effects of the shell structure. This conclusion resembles the $Z^{1/3}$ periodic oscillation of the ground-state energy of an atom away from the systematic trend [98]. With uncertainty of the peak location in mind, one may speculate that our result is a manifestation of the same effect for highly-excited states. More work is necessary to bring understanding to this issue.

We also repeated the same Fourier analysis by choosing the range of $Z^{1/3}$ to be $L = 102^{1/3}$ which includes all the numerical data. As far as experimental data go in the range of $Z^{1/3}$ between $83^{1/3}$ and $102^{1/3}$ we used extrapolation of our cubic spline fit. As a result the peaks just discussed slightly change their positions and amplitudes but within the $2\pi/L$ uncertainty systematic, experimental and numerical Fourier spectra share a peak in common corresponding to the Zel'dovich effect. Similarly, experimental and numerical spectra continue to share a peak in common due to the effects of the shell structure.

3.5 Conclusions and future directions

In this chapter we analyzed in a model-independent fashion the weakly-bound s spectra of the distorted Coulomb problem for arbitrary relationship between the range of the inner potential and Bohr's radius of the Coulomb field. We demonstrated that the spectra are fairly sensitive to the binding properties of the inner potential which constitutes the essence of the Zel'dovich effect, and established the corresponding details of spectral changes. Armed with these results, we conducted an analysis of experimental and numerical Rydberg spectra of atoms along the Periodic Table which

indeed show an evidence of the Zel'dovich effect. Our analysis can be extended and adopted in several directions:

First, there is an abundance of experimental and numerical data for atomic Rydberg states of finite angular momenta which are likely to contain signatures of the Zel'dovich effect. However, in the limit of a very short-ranged inner potential the way the effect manifests itself is somewhat different from its s state counterpart [60]. This observation makes it pertinent to generalize our analysis to the case of finite angular momentum.

It has been known for some time [99] that the Rydberg formula (2) is superior to the Wannier (Bohr) formula quoted in textbooks [55] in representing excitonic spectra in condensed matter systems. Experimental examples here include clean and doped rare-gas solids and rare-gas impurities in solid hydrogen. Although this is a context in which the Zel'dovich effect has been originally discovered [56], to the best of our knowledge there were no attempts to relate it to excitonic quantum defects. Because of the dielectric screening of the Coulomb interaction, the Zel'dovich effect in these systems is expected to be more pronounced than in atomic Rydberg spectra. Only minor changes to our analysis are needed to understand the excitonic Rydberg spectra.

Other examples of systems where the Zel'dovich effect should have experimental signatures include Rydberg ions and electronic image states [100].

Bibliography

- [1] N. W. Ashcroft and N. D. Mermin, *Solid State Physics* (Saunders College Publishing, 1976).
- [2] J. De Boer, *Physica* **14**, 139 (1948); J. De Boer and B. S. Blaisse, *Physica* **14**, 149(1948); J. de Boer and R. J. Lunbeck, *Physica* **14**, 520 (1948).
- [3] P. W. Anderson and R. G. Palmer, *Nat. Phys. Sci.* **231**, 145 (1971); *Phys. Rev. D* **9**, 3281 (1974); see also P. W. Anderson, *Basic Notions of Condensed Matter Physics* (Addison-Wesley Reading, Massachusetts, 1997), Section IIID.
- [4] J. W. Clark and N. C. Chao, *Nat. Phys. Sci.* **236**, 37 (1972).
- [5] N. D. Mermin and H. Wagner, *Phys. Rev. Lett.* **17**, 1133 (1966), N. D. Mermin, *J. Math. Phys.* **8**, 1061 (1967); P. C. Hohenberg, *Phys. Rev.* **158**, 383 (1967).
- [6] V. N. Popov, *Teor. Mat. Fiz.* **11**, 354 (1972) [*Theor. Math. Phys.* **11**, 65 (1972)]; K.B. Efetov and A. I. Larkin, *Zh. Eksp. Teor. Fiz.* **69**, 764 (1975) *Sov. Phys. JETP* **43**, 390 (1976); F. D. M. Haldane, *Phys. Rev. Lett.* **45**, 1358 (1980); **47**, 1840 (1981); *J. Phys. C* **14**, 2585 (1981); *Phys. Lett.* **81A**, 153 (1981); E. B. Kolomeisky and J.P. Straley, *Rev. Mod. Phys.* **68**, 175 (1996), and references therein.
- [7] L. H. Nosanow, L. J. Parish, and F. J. Pinski, *Phys. Rev. B* **11**, 191 (1975).
- [8] S. Iijima, *Nature (London)*, **354**, 56 (1991).
- [9] P. M. Ajayan and T. W. Ebbesen, *Rep. Prog. Phys.* **60**, 1025 (1997).
- [10] W. Teizer, R. B. Hallock, E. Dujardin, and T. W. Ebbesen, *Phys. Rev. Lett.* **82**, 5305 (1999), and references therein.

- [11] C. Dillon, K. M. Jones, T. A. Bekkedahl, C. H. Kiang, D. S. Bethune, and M. J. Heben, *Nature* (London), **386**, 377 (1997); F. Darkrim and D. Levesque, *J. Chem. Phys.* **109**, 4981 (1998); J. M. Ogden, *Physics Today* **55**, 69 (2002), and references therein.
- [12] F. Schreck, L. Khaykovich, K. L. Corwin, G. Ferrari, T. Bourdel, J. Cubizolles, and C. Salomon, *Phys. Rev. Lett.* **87**, 080403 (2001); A. Görlitz, J. M. Vogels, A. E. Leanhardt, C. Raman, T. L. Gustavson, J. R. Abo-Shaeer, A. P. Chikkatur, S. Gupta, S. Inouye, T. Rosenband, and W. Ketterle, *Phys. Rev. Lett.* **87**, 130402 (2001).
- [13] K. E. Strecker, G. B. Partridge, A. G. Truscott, and R. G. Hulet, *Nature* (London) **417**, 150 (2002); L. Khaikovich, F. Schreck, G. Ferrari, T. Bourdel, J. Cubizolles, L. D. Carr, Y. Castin, C. Salomon, *Science* **296**, 1290 (2002).
- [14] M. A. Kasevich, *C. R. Acad. Sci. IV* **2**, 497 (2001).
- [15] G. Stan, V. H. Crespi, M. W. Cole, and M. Boninsegni, *J. Low Temp. Phys.* **113**, 447 (1998); M. Boninsegni and S. Moroni, *J. Low Temp. Phys.* **118**, 1 (2000).
- [16] M. C. Gordillo, J. Boronat, and J. Casulleras, *Phys. Rev. B* **61**, R878 (2000).
- [17] M. C. Gordillo, J. Boronat, and J. Casulleras, *Phys. Rev. Lett.* **85**, 2348 (2000).
- [18] E. Krotscheck, M. D. Miller, and J. Wojdylo, *Phys. Rev. B* **60**, 13028 (1999), E. Krotscheck, M. D. Miller, *ibid.* **60**, 13038 (1999).
- [19] A. I. Karaevskii and V. V. Lubashenko, *Phys. Rev. B* **60**, 12091 (1999).
- [20] P. M. Morse, *Phys. Rev.* **34**, 57 (1929); L. D. Landau and E. M. Lifshitz, *Quantum Mechanics* (Pergmon, New York, 1977), Problem 4 to Section 23.
- [21] I. F. Silvera and V. V. Goldman, *J. Chem. Phys.* **69**, 4209 (1978), I. F. Silvera, *Rev. Mod. Phys.* **52**, 393 (1980).
- [22] J. B. Kogut, *Rev. Mod. Phys.* **51**, 659 (1979), and references therein.
- [23] E. B. Kolomeisky and J. P. Straley, *Phys. Rev. B* **62**, 301 (2000).
- [24] A. O. Caldeira and A. J. Leggett, *Phys. Rev. Lett.* **46**, 211 (1981)

- [25] The first term of (1.13) written in terms of the Fourier transform $h(\omega)$ is identical to the first term of Eq.(5) in [23].
- [26] R. P. Feynman, *Statistical Mechanics* (Benjamin, Boston, 1972), p. 67.
- [27] Y. Saito, Z. Phys. B **32**, 75 (1978).
- [28] J. D. Weeks, Phys. Rev. B **26**, 3998 (1982); in *Phase Transformations in Solids*, edited by T. Tsakalakos (Elsevier, New York, 1984), p. 597.
- [29] R. Lipowsky, D. M. Kroll, and R. K. P. Zia, Phys. Rev. B **27**, 4499 (1983).
- [30] M. P. A. Fisher and W. Zwerger, Phys. Rev. B **32**, 6190 (1985), and references therein; mathematically equivalent problem is that of a single impurity in an electronic Luttinger liquid as discussed in C. L. Kane and M. P. A. Fisher, Phys. Rev. Lett. **68**, 1220 (1992) and Phys. Rev. B **46** 15233 (1992).
- [31] E. B. Kolomeisky, R. M. Konik, and X. Qi, Phys. Rev. B **66**, 075318 (2002).
- [32] H. Kleinert, *Path Integrals in Quantum Mechanics, Statistics, and Polymer Physics* (World Scientific, Singapore, 1995), Chapter 5 and references therein.
- [33] E. Brézin, B. I. Halperin, and S. Leibler, Phys. Rev. Lett. **50**, 1387 (1983).
- [34] F. Lindemann, Phys. Z. (Leipzig), **11**, 69 (1910).
- [35] M. K. Kostov, M. W. Cole, J. C. Lewis, P. Diep, and J. K. Johnson, Chem Phys. Lett. **332**, 26 (2000); M. K. Kostov, J. C. Lewis, and M. W. Cole, cond-mat/0010015.
- [36] M. Boninsegni, S. -Y. Lee, and V. H. Crespi, Phys. Rev. Lett. **86**, 3360 (2001), and references therein.
- [37] E. Wigner and H. B. Huntington, J. Chem. Phys. **3**, 764 (1935), and references therein.
- [38] M. M. Calbi, M. W. Cole, S. M. Gatica, M. J. Bojan, and G. Stan, Rev. Mod. Phys. **73**, 857 (2001), and references therein.
- [39] W. Kolos and L. Wolniewicz, J. Chem. Phys. **43**, 2429 (1965).
- [40] R. D. Etters, J. V. Dugan, and R. W. Palmer, J. Chem. Phys. **62**, 313 (1975).

- [41] R. Aziz, V. P. S. Nain, J. S. Carley, W. L. Taylor and G. T. McConville, J. Chem. Phys. **70**, 4330 (1979).
- [42] R. E. Grisenti, W. Schöllkopf, J. P. Toennies, G. C. Hegerfeldt, T. Köhler, and M. Stoll, Phys. Rev. Lett. **85**, 2284 (2000), and references therein.
- [43] E. P. Bashkin, Zh. Eksp. Teor. Fiz. **78**, 360 (1980) [Sov. Phys. JETP **51**, 181 (1980)].
- [44] M. W. Cole, V. H. Crespi, G. Stan, C. Ebner, J. M. Hartman, and M. Boninsegni, Phys. Rev. Lett. **84**, 3883 (2000), and references therein.
- [45] R. J. Hemley, H. K. Mao, L. W. Finger, A. P. Jephcoat, R. M. Hazen, and C. S. Zha, Phys. Rev. B **42**, 6458 (1990).
- [46] R. E. Peierls, *Quantum Theory of Solids* (Oxford, 1955), Section 5.3; *More Surprises in Theoretical Physics* (Princeton University Press, 1991), Section 2.3.
- [47] P. Loubeyre, F. Occelli, and R. LeToullec, Nature (London) **416**, 613 (2002), and references therein.
- [48] It has been demonstrated in J. B. Neaton and N. W. Ashcroft, Nature (London) **400**, 141 (1999) that under high pressure similar pairing into Li_2 molecules takes place in ordinary solid lithium.
- [49] P. W. Anderson, *Basic Notions of Condensed Matter Physics* (Addison-Wesley Reading, Massachusetts, 1997), Section IIID.
- [50] For nice reviews see J. G. Dash, Rev. Mod. Phys. **71**, 1737 (1999) and U. Tartaglino, T. Zykova-Timan, F. Ercoleassi, and E. Tosatti, cond-mat/0504680.
- [51] H. A. Fertig, R. Côté, A. H. MacDonald, and S. Das Sarma, Phys. Rev. Lett. **69**, 816 (1992); R. Côté and H. A. Fertig, Phys. Rev. B **48**, 10955 (1993).
- [52] J. N. Crain and D. T. Pierce, Science, **307**, 703 (2005), and references therein.
- [53] E. B. Kolomeisky, X. Qi, and M. Timmins, Phys. Rev. B **67**, 165407 (2003), and references therein.

- [54] L. D. Landau and E. M. Lifshitz, *Quantum Mechanics*, (Pergamon, New York, 1977), Sections 117 and 138.
- [55] N. W. Ashcroft and N. D. Mermin, *Solid State Physics*, (Saunders, Philadelphia, 1976), Chapter 30.
- [56] Ya. B. Zel'dovich, *Fiz. Tverd. Tela* (Leningrad), **1**, 1637 (1959) [*Sov. Phys. Solid State* **1**, 1497 (1959)].
- [57] Sections 21 and 32 of Ref. [54].
- [58] V. S. Popov, *Zh. Eksp. Teor. Fiz.* **60**, 1228 (1971) [*Sov. Phys. JETP* **33**, 665 (1971)].
- [59] A. E. Kudryavtsev, V. E. Markushin, and I. S. Shapiro, *Zh. Eksp. Teor. Fiz.* **74**, 432 (1978) [*Sov. Phys. JETP* **47**, 225 (1978)]; I. S. Shapiro, *Phys. Rep.* **35C**, 131 (1978)]; D. A. Kirzhnits and F. M. Pen'kov, *Zh. Eksp. Teor. Fiz.* **82**, 657 (1982) [*Sov. Phys. JETP* **55**, 393 (1982)].
- [60] A. E. Kudryavtsev and V. S. Popov, *Pis'ma Zh. Eksp. Teor. Fiz.* **29**, 311 (1979) [*Sov. Phys. JETP Lett.* **29**, 280 (1979)], V. S. Popov, A. E. Kudryavtsev and V. D. Mur, *Zh. Eksp. Teor. Fiz.* **77**, 1727 (1979) [*Sov. Phys. JETP* **50**, 865 (1979)], V. S. Popov, A. E. Kudryavtsev, V. I. Lisin, and V. D. Mur, *Zh. Eksp. Teor. Fiz.* **80**, 1271 (1981) [*Sov. Phys. JETP* **53**, 650 (1981)], B. M. Karnakov, A. E. Kudryavtsev, V. D. Mur, and V. S. Popov, *Zh. Eksp. Teor. Fiz.* **94**, 65 (1988) [*Sov. Phys. JETP* **68**, 1333 (1988)].
- [61] B. M. Karnakov, *Pis'ma Zh. Eksp. Teor. Fiz.* **77**, 73 (2003) [*JETP Lett.* **77**, 68 (2003)], V. S. Popov, *ibid.* 79 (2003) [*ibid.* 74 (2003)].
- [62] H. Friedrich, *Theoretical Atomic Physics*, (Springer-Verlag, 1991).
- [63] R. Latter, *Phys. Rev.* **99**, 510 (1955).
- [64] S. T. Manson, *Phys. Rev.* **182**, 97 (1969).
- [65] U. Fano, C. E. Theodosiou and J. L. Dehmer, *Rev. Mod. Phys.* **48**, 49 (1976).
- [66] F. Herman and S. Skillman, *Atomic Structure Calculations* (Prentice-Hall, Englewood Cliffs, N. J., 1963).

- [67] A. B. Migdal, *Qualitative Methods in Quantum Theory* (Benjamin, Reading, MA, 1977), Chapter 3.
- [68] N. N. Lebedev, *Special Functions and Their Applications*, (Prentice-Hall, Inc. Englewood Cliffs, New Jersey, 1965).
- [69] L. D. Landau and Ya. A. Smorodinskii, Zh. Eksp. Teor. Fiz. **14**, 269 (1944); see also Eq. (138.12) of Ref. [54].
- [70] S. Deser, M. L. Goldberger, K. Baumann, and W. Thirring, Phys. Rev. **96**, 774 (1954).
- [71] A more accurate calculation based on Eq.(3.9) gives $\mu = -2a_s/a_B - x_0^4/32$ which is negative for sufficiently weak $U_s(r)$; for $x_0 \ll 1$ this effect however is negligible as can be seen from Fig. 3.3 on page 70.
- [72] Section 132 of Ref. [54].
- [73] Section 133 of Ref. [54].
- [74] A generalization of Levinson's theorem to potentials with Coulomb tails can be found in Z. R. Iwinski, L. Rosenberg, and L. Spruch, Phys. Rev. Lett. **54**, 1602 (1985), and Z. Ma Phys. Rev. D **33**, 1745 (1986).
- [75] M. V. Berry, Sci. Prog., Oxf. **57**, 43 (1969).
- [76] M. V. Berry and K. E. Mount, Rep. Prog. Phys. **35**, 315 (1972).
- [77] Section 70 of Ref. [54].
- [78] Eq.(3.22) predicts that there is an unphysical divergence as $Z \rightarrow 1 + 0$ which is present but hardly noticeable in the inset. The oscillation shown in bold is everywhere finite.
- [79] L. B. Robinson, Phys. Rev. **117**, 1281 (1960).
- [80] A. A. Radzig and B. M. Smirnov, *Reference Data on Atoms, Molecules and Ions*, (Springer-Verlag, 1985), Table 5.2, and references therein.
- [81] C. Jaffé and W. P. Reinhardt, J. Chem. Phys. **66**, 1285 (1977), and references therein.
- [82] TOPbase: on-line interactive database of atomic data, <http://vizier.u-strasbg.fr/topbase/home.html>.

- [83] K. Radler and J. Berkowitz, *J. Chem. Phys.* **70**, 216 (1979).
- [84] S. F. Dyubko, V. A. Efremov, V. G. Gerasimov and K. B. MacAdam, *J. Phys. B: At. Mol. Opt. Phys.* **37**, 1967 (2004).
- [85] B. Ruscic and J. Berkowitz, *Phys. Rev. A* **40**, 6716 (1989).
- [86] R. H. Page and C. S. Gudeman, *J. Opt. Soc. Am. B* **7**, 1761 (1990).
- [87] M. Kompitsas, C. Baharis, and Z. Pan, *J. Opt. Soc. Am. B* **11**, 697 (1994).
- [88] W. Li, I. Mourachko, M. W. Noel and T. F. Gallagher, *Phys. Rev. A* **67**, 052502 (2003).
- [89] Z. J. Jakubek and B. Simard, *J. Phys. B: At. Mol. Phys.* **33**, 1827 (2000).
- [90] D. M. Rayner, S. A. Mitchell, O. L. Bourne and P. A. Hackett, *J. Opt. Soc. Am. B* **4**, 900 (1987).
- [91] F. Federmann, K. Hoffmann, N. Quaas, and J.D.Close, *Phys. Rev. Lett.* **83**, 2548 (1999).
- [92] J. H. M. Neijzen and A. Dönszelmann, *J. Phys. B: At. Mol. Phys.* **15**, 1981 (1982).
- [93] P. Goy, J. M. Raimond, G. Vitrant and S. Haroche, *Phys Rev A* **26**, 2733 (1982).
- [94] G. J. Ding, R. C. Shang, L. F. Chang, K. L. Wen, Q. Hui, and D. Y. Chen, *J. Phys. B: At. Mol. Opt. Phys.* **22**, 1555 (1989).
- [95] J. C. Slater, *Phys. Rev.* **36**, 57 (1930).
- [96] *Atomic Reference Data for Electronic Structure Calculations*,
<http://physics.nist.gov/PhysRefData/DFTdata/>.
- [97] *CRC Handbook of Chemistry and Physics*, D. R. Lide, Editor-in-Chief, 84th Edition 2004-2005 (Boca Raton, CRC Press, LLC), 12-14; <http://www.hbcpnetbase.com/>. The crystal ionic radius of the same ion varies with its coordination number; the data shown in Fig. 3.11 on page 91 are averages (if more than one coordination number is possible).
- [98] B.-G. Englert, *Semiclassical Theory of Atoms*, Lecture Notes in Physics, 300 (Springer-Verlag, Berlin, 1988), Chapter 5, and references therein.

- [99] L. Resca and R. Resta, Phys. Rev. B **19**, 1683 (1979), and references therein; V. Saile, R. Reininger, P. Laporte, I. T. Steinberg, and G. L. Findley, Phys. Rev. B **37**, 10901 (1988), and references therein.
- [100] S. G. Davison and M. Stes'licka, *Basic Theory of Surface States*, (Clarendon Press, Oxford, 1992), Chapter 7, and references therein.